

國立交通大學

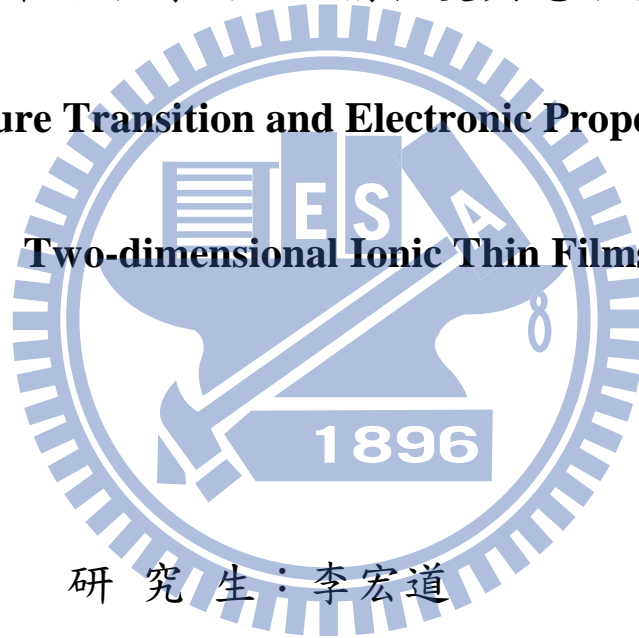
物理研究所

博士論文

二維離子薄膜之結構相變與電子特性

Structure Transition and Electronic Properties of

Two-dimensional Ionic Thin Films



研究生：李宏道

指導教授：江進福 教授

林登松 教授

中華民國一〇〇年六月

二維離子薄膜之結構相變與電子特性

Structure Transition and Electronic Properties of

Two-dimensional Ionic Thin Films

研究生：李宏道

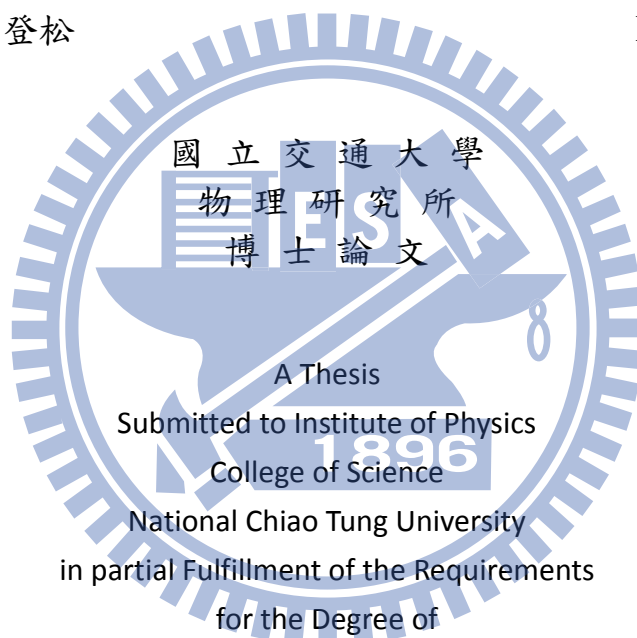
指導教授：江進福

林登松

Student : Hong-Dao Li

Advisor : Tsin-Fu Jiang

Deng-Sung Lin



A Thesis
Submitted to Institute of Physics
College of Science
National Chiao Tung University
in partial Fulfillment of the Requirements
for the Degree of

Doctor

in

Physics

June 2011

Hsinchu, Taiwan

中華民國一〇〇年六月

二維離子薄膜之結構相變與電子特性

學生：李宏道

指導教授：江進福 博士

林登松 博士

國立交通大學物理研究所博士論文

摘要

近年來異質磊晶成為製造超大型積體電路的一個重要技術,我們也經常藉由異質磊晶來研究不同材料之間的介面特性,希望藉由深入了解磊晶成長機制,進而能自由的操控薄膜特性。氯化鈉和矽有相近的晶格常數,但在原子間的鍵結本質上有很大的差異,氯和矽的電負度差是 1.2,而和鈉的電負度差是 2.1,這樣的離子共價介面存在許多有趣的問題:氯化鈉和矽的介面將傾向形成離子鍵或共價鍵?在介面又會存在甚麼樣的物理特性?我們可否人工製造出單原子層的離子薄膜?在本論文中,我們結合了原子層沉積法與自我限制反應的概念,設計了一個兩階段的磊晶方法來研究這些問題。

首先,我們利用表面矽原子懸鍵的活性製造出一個有序的氯/矽(100)面,然後蒸鍍不同數量的鈉原子在這個表面上,如此便可直接的觀察三種原子之間的交互作用,我們同時利用掃描隧道顯微鏡 (STM), X 射線光電子能譜 (XPS) 和第一原理計算 (DFT) 來研究薄膜成長過程中的表面形貌,電子狀態和界面性質的演變。STM 結果顯示,當少量的鈉吸附時表面同時存在三種結構有 $p(2 \times 2)$ 、單一暗點、和一大塊的暗斑。當鈉覆蓋率達到 0.5 ML,表面會形成唯一的 $p(2 \times 2)$ 有序結構,當覆蓋超過 1 ML 時,表面會戲劇性的轉變為大規模且均勻的 $p(1 \times 1)$ 結構。經由高度及距離量測,我們推斷其應為二維 NaCl(100) 薄膜。XPS 結果則顯示,隨著鈉覆蓋增加, Cl 2p 和 Na 2p 的束縛能同步增加約 1.1 eV。它反映出磊晶過程中產生不同的鍵結形態。當鈉覆蓋率超過 1 ML, Si 2p 光譜顯示表面矽原子的電子

恢復成懸鍵狀態，此時氯化鈉薄膜與基底只存在微弱的凡德瓦作用力。

第一原理計算結果顯示，單一鈉原子喜歡吸附在氯原子之間的洞位，且鈉原子可以很容易地沿二聚體擴散組裝成氯化鈉(111)叢集結構。此結構對應於STM圖中的單一暗點，當叢集密度增加後表面將從氯化鈉(111)轉化為氯化鈉(111)-(100)共面結構，此結構對應於STM圖中的 $p(2 \times 2)$ 有序結構，當鈉原子覆蓋率超過1 ML，氯、鈉原子將自組裝成氯化鈉(100)薄膜，對應於STM圖中的 $p(1 \times 1)$ 有序結構。整個磊晶成長過程遵循 Franck-van der Merve 成長模式。最後我們計算了該系統一系列的電子特性，包括電子態密度、空間分布，STM 影像模擬以及 XPS 光譜模擬，模擬結果與我們的實驗相當吻合，它不僅成功解釋了實驗數據，更幫助我們了解深層的物理意義。



Structure Transition and Electronic Properties of

Two-dimensional Ionic Thin Films

Student : Hong-Dao Li

Advisor : Dr. Tsin-Fu Jiang

Dr. Deng-Sung Lin

Institute of Physics, National Chiao Tung University

Abstract

Heteroepitaxy has now become an important technique for fabricating very-large scale integrated circuits (VLSI). It also serves as an ideal sample preparation tool for understanding the nature in heterogeneous interface. Furthermore, one hopes to gain sufficient insight to manipulate the thin film structures with desired properties. Silicon and sodium chloride have similar lattice constant but much difference in crystal structure (fcc & diamond). The electronegativity difference between chlorine and silicon is 1.2 and that between chlorine and sodium is 2.1. Many interesting questions can be raised regarding the ionic crystal-covalent crystal interface: What correlations can be drawn about the difference in electronegativity between bonded atoms and their tendency to form ionic or covalent bonds? What kind of physical properties exist in interface? Can we produce a NaCl thin film of only single layer in thickness? In this thesis, we designed a two-step epitaxy to research these issues through a combination of atomic layer deposition (ALD) and self-limited concept. First, we prepared a oriented Cl/Si(100)-(2x1) surface, and then deposit various amount of sodium atoms on the surface. On the sample surface, we can directly observe the interaction between three species of atoms. The evolution of the surface

morphology, the electronic state, and the interfacial properties during the film growth are investigated by scanning tunneling microscopy (STM), X-ray photoelectron spectroscopy (XPS) and first principle calculations (DFT).

The STM result shows, in low sodium coverage ($\theta_{Na} = 0.1$), the surface consists three kind of adsorption structures, the single dim spot, the p(2x2) domain and a domain of dim spots. At intermediate coverage ($\theta_{Na} = 0.5$), the surface would transform into unique p(2x2) ordered structure. When the coverage over 1 ML, the surface dramatically transformed into large scale and uniform p(1x1) structure. By a steric measurement, we concluded the structure is a two dimensional NaCl(100) film. The XPS spectra indicate, with increasing of sodium coverage, the Cl2p and Na2p peaks synchronously increase by about 1.1 eV. It suggests significant transition in their bonded electronic state during the Na adsorption process. The Si 2p spectra indicate, when sodium coverage is over 1 ML, the electron state in surface silicon retrieved dangling bond state; namely, the Van der Waals force dominated the interaction between the NaCl thin film and silicon substrate.

From first principle calculation, we showed that the single sodium prefer to adsorb on hollow sites between chlorine atoms and that the sodium atom can easily diffuse along the dimer row assembling into NaCl(111) cluster. The structure should correspond to single dim spot that we observed in STM. With the increasing of cluster density, the structure would transform into NaCl(111)-(100) concomitant phase; It just corresponding to p(2x2) ordered structure that we observed in STM. When the sodium coverage over 1 ML, the cluster would entirely self-assemble into NaCl(100) monolayer. We demonstrated that the epitaxy process follows Franck-van der Merve growth mode. Finally, we also simulated a series of electronic properties including density of state (DOS), spatial charge distribution, STM image and XPS spectra

simulation. The simulation result showed good agreement with our experiment data; it not only successfully explains the experimental data but also clarifies the underlying physics.



致謝

本論文得以順利的完成,首先要感謝我的指導老師 林登松教授,對我的知遇之恩,與老師在學術上的討論思辨,以及生活上的關懷鼓勵,使我獲益良多,老師認真勤奮且嚴謹的工作態度,是我終身學習的典範。感謝 鄭弘泰教授對於我模擬工作的指導,每周的討論明確地指引我研究的方向,是實質且有用的幫助。感謝中正大學 梁贊全教授引領我進入理論模擬的領域,在中正的學習期間,耐心地教導我一步一步建立起理論基礎,提供我許多方便的小程式,使我的分析工作進行的更順利。此外,要感謝我的口試委員江進福、林炯源、鄭舜仁教授的指正與建議,使得我的論文更加的完善。也要感謝國家高速電腦中心、交大理學院、國家同步輻射中心提供的軟硬體資源。

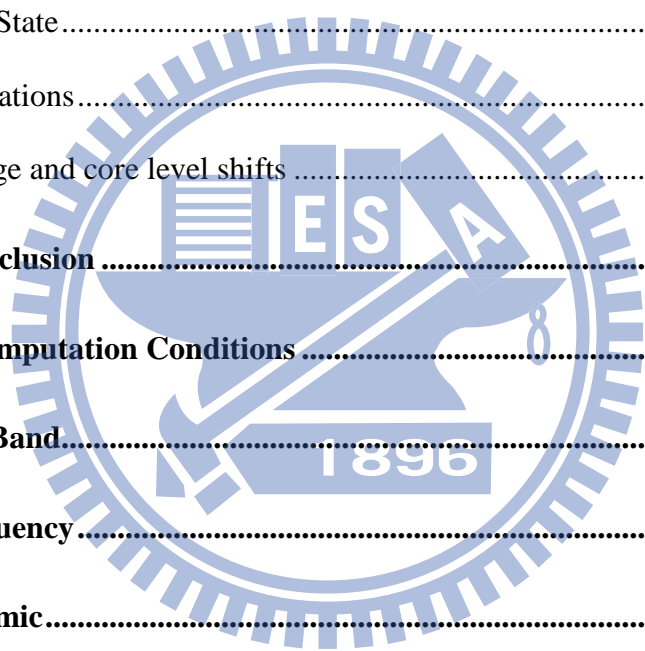
感謝模擬間的好夥伴 candy 經常交流討論,每天播放好聽的詩歌,使我時常感覺天使在身邊圍繞。感謝仁陽、展源、中廷一起走過在同步熬夜做實驗的日子,還記得第一次同步結束,看見清晨微露的曙光,內心的感動無以言喻。特別要感謝展源即使在離開實驗室後,仍然熱衷的與我討論 STM 影像意義,對於真理的執著與追求,啟發了我許多的靈感。懷念與靖勛一起製作”搞笑泡泡機”的日子,從這東西得到不少樂子,希望你在異鄉的日子能平安順利。感謝國威時常與我嘴砲,閒聊實驗室發生的趣事,讓我最後寫論文這段時間每天都很歡樂,模擬組的重擔就交給你了,把模擬的技術發揚光大吧!!感謝學弟妹榮君、卓穎、鈺佑、琬珩的互相扶持,一同出遊的美好回憶,使我博士班生涯增色不少,希望妳們的研究工作都能順利進行,天下無不散的宴席,期待未來我們還能有相聚的一天。

感謝我父母親的支持與鼓勵,無怨無悔的付出,讓我得以完成我的夢想。最後,我要感謝我老婆思帆以及我的岳母對我的體諒,照顧我可愛的女兒羽橙,讓我沒有後顧之憂,這段日子您真的辛苦了,未來的日子讓我們一起共同努力吧!!

Contents

Chapter1 Introduction.....	1
1.1 Motivation.....	1
1.2 Si(100) surface reconstruction	5
1.3 Madelung constant	8
1.4 Literature Review.....	11
1.4.1 NaCl /Cu(111).....	11
1.4.2 NaCl/Ge (100).....	13
1.4.3 NaCl/Si (100).....	16
Chapter2 Theory.....	20
2.1 Born-Oppenheimer approximation	20
2.2 Hartree-Fock approximation	21
2.3 Density Functional Theory.....	23
2.4 Exchange-Correlation Functional	27
2.5 Bloch's Theory.....	29
Chapter3 Algorithm.....	34
3.1 Pseudopotential	34
3.2 Projector Augmented Wave (PAW).....	37
3.3 Residual Minimization Scheme(RMS)	40
3.4 Ab-initio molecular dynamics (AIMD)	41
Chapter4 Experimental results.....	45
4.1 Principle of STM.....	46
4.2 STM results	48

4.3 Principle of XPS	52
4.4 XPS results.....	55
Chapter 5 Computational results(I) : morphology and dynamics	59
5.1 Static structure relaxations	59
5.2 Diffusion process	61
5.3 Finite temperature simulations.....	64
Chapter 6 Computational results (II) : Electronic properties	77
6.1 Density of State.....	77
6.2 STM simulations.....	84
6.3 Bader charge and core level shifts	89
Chapter 7 Conclusion	95
APPENDIX: Computation Conditions	98
Nudged Elastic Band.....	100
Vibrational frequency.....	100
Molecular Dynamic.....	101
Reference.....	102



List of Figures

Figure 1.1.1 (a) Nearest distance and (b) Normalized pair bond energy of various kinds of ionic solid from one (molecule) to three dimensions.....	4
Figure 1.1.2 Schematic diagram of self-limited reaction.....	4
Figure 1.2.1 (a) Tetrahedral bond arrangement of diamond structure. (b) The Bird's eye view of diamond structure, the fractions denoted the height of the atoms in units of a cubic edge.	6
Figure 1.2.2 (a) The oblique view of the primary Si(100)-p(1x1) surface. Spheres are Si atoms and conoid sticks are dangling bonds. Each silicon atom has two valence bonds and two dangling bonds, and (b) after reconstructive Si(100)-p(2x1) surface....	6
Figure 1.2.3 (a) Top view of four kinds of silicon reconstructions .Smaller spheres represents deeper atoms. (b) A schematic illustration of the order of magnitude of energy differences between different reconstructions of Si (100).	7
Figure 1.2.4 Step structures on the Si(100)-p(2x1) surface. (a) STM image of Si(100)-p(2x1) surface. The size is 15 nmx10 nm and $V_s = 2$ V. (b) Oblique, (c) top and (d) side views of step structures..	7
Figure 1.3.1 Madelung constant Function $\alpha(\theta)$ in 1D non-collinear and 2D non-coplanar anion-cation pairing system.	10
Figure 1.4.2 From top to bottom, (a) the experimental STM images acquired with pentacene on Cu (111) (without NaCl interlayer) and (b) STM images of pentacene on NaCl/Cu(111) surface with a metal and a pentacene tip, the images at bias voltages exceeding the HOMO (left) or LUMO (right) exhibit very pronounced features.(c) The results of theoretical calculations.....	12

Figure 1.4.4 (a) Large-area STM scan ($1130 \times 1130 \text{ \AA}^2$) of NaCl on Ge(100). Nearly all NaCl islands have a height of one double layer ($V_s = -2.7 \text{ V}$, $I_t = 0.7 \text{ nA}$). (b) STM image ($98 \times 81 \text{ \AA}^2$) with atomic resolution of a NaCl layer of one double layer. 15

Figure 1.4.5 (a) Layer adsorption energies per 1×1 supercell for NaCl adsorbed on a Ge (100) surface ($\Delta E_{\text{ads}}(n) \equiv [E_{\text{NaCl/Ge}}(n-1) + E_{\text{Na}} + E_{\text{Cl}} - E_{\text{NaCl/Ge}}(n)]$), (b) The electronic band structure and PDOS for 10 ML NaCl/Ge(100) surface. 16

Figure 1.4.6 (a) NaCl dimers on a Si(100)-c(4×2) reconstruction. The silicon surface reconstruction disappeared and the pattern of NaCl dimers mimics the original silicon surface reconstruction. (b) $(\text{NaCl})_4$ cube adsorbed in a hole of the silicon model tip. The green (dark gray large sphere) and purple (dark gray small sphere) spheres denote Cl and Na atoms respectively. 17

Figure 1.4.7 (a) Si $2p$ core-level photoemission spectra (dots) of Si(100) surface with various amounts of NaCl deposition, as specified. The solid curves fit to the spectra. The curves labeled B, S, I, and Si^+ are the results, respectively, of the decomposition of the Si $2p$ spectra into contributions from the bulk, the clean surface, the interface layer, and the Si-Cl species. The energy zero refers to the bulk position. (b) Cl $2p$ (left), and Na $2p$ core-level photoemission spectra (dots) corresponding to Si $2p$ 18

Figure 1.4.8 (a) Filled-state STM images showing morphology evolution with various NaCl coverages on Si(100), as labeled. All images are obtained at room temperature with $I_t = 0.23 \text{ nA}$ and $V_s =$ (a) -2.05 , (b) -2.3 , (c), and (d) -2.8 V . The images cover an area of about (a) $80 \text{ nm} \times 40 \text{ nm}$, and (b)–(d) $300 \times 150 \text{ nm}$. The apparent topographic height profiles along the line segments and schematics of grown NaCl nanofilms were shown in right side. 19

Figure 2.3.1 Flowchart of self-consistent loop	26
Figure 2.5.1 Sketch diagram of DOS smearing, the short solid line in left represents discrete eigenstates and the red curve represents its dispersion broadening. The spectrum on right side represents integral results through the different smearing method.	33
Figure 3.1.1 Sketch diagram of the all-electron (AE) wavefunction and electronic potential (solid lines) plotted against distance, r , from the atomic nucleus.....	37
Figure 3.4.1 Diagrammatic sketch of an MD trajectory upon BO surface	44
Figure 3.4.2 Flow chart of iterative procedure of <i>ab initio</i> molecular dynamics simulations (AIMD).....	45
Figure 4.1.1 Schematic diagram of the essential elements of STM.....	47
Figure 4.1.2 Schematic diagram of quantum tunneling phenomenon	48
Figure 4.1.3 Schematic diagrams of tunneling current under varying bias voltage in fill state (a) the current tunneling from sample to tip; in empty state (b) the current tunneling from tip to sample.....	48
Figure 4.2.1 A series of STM images which scanned by the following parameters: ..	52
Figure 4.3.1 Ultra high vacuum system (UHV) for core-level-photoemission spectroscopy.....	54
Figure 4.4.1 Si $2p$ core level photoemission spectra (red circles) for the ALD growth process.....	57
Figure 4.4.2 Cl $2p$ (left) and Na $2p$ (right) core level photoemission spectra (red and black dots) in different sodium coverage.....	58
Figure 5.1.1 (a) Bird's eye view of chlorine terminated Si(100) surface with six high	

symmetry adsorption sites,(b) mean adsorption energy table, (c) configuration of H1H2 case ,and (d) configuration of H1H2H2H2 case.	61
Figure 5.2.1 Sketch of the Nudged Elastic Band (NEB) method.....	63
Figure 5.2.2 Energy variation along the diffusion path A→B→C→D, each the path contains eight intermediate states (black circle).	64
Figure 5.3.1 (a)-(f) Molecular dynamic process: $\theta_{Na}=6/36$ (random), and (g) temperature history. Each snapshot includes three kinds direction of view, the bird's eye view(left),side view(upper right),and oblique view(lower right).....	71
Figure 5.3.2 (a)-(f) Molecular dynamic process: $\theta_{Na}=5/36$ and (g) temperature history.....	72
Figure 5.3.3 (a)-(f) Molecular dynamic process: $\theta_{Na}=9/36$ and (g) temperature history.....	73
Figure 5.3.5 (I)-(V) structures were calculated by static relaxation after “annealing”, (VI)-(XII) structures were calculated by static relaxation, and (XII) was calculated by static relaxation from predetermined coplanar NaCl(100) layer after “annealing”.....	75
Figure 5.3.6 Mean adsorption energy diagram of various structures.....	76
Figure 6.1.1 Density of state (DOS) of chlorine pre-covered case (left) and single sodium adsorption case (type I). Which atom we used for computing project density of state (PDOS) was marked with darker color.	79
Figure 6.1.2 Density of state (DOS) of (a) type II (3/36 ML) and (b) type III case (5/36 ML).....	80
Figure 6.1.3 Density of state (DOS) of (a) type IV (9/36 ML) and (b) type V case	

(13/36 ML).....	81
Figure 6.1.4 Density of state (DOS) of (a)type VIII (12/36 ML) and (b)type XI case (36/36 ML).....	82
Figure 6.1.5 Density of state (DOS) of (a) type XII case (36/36 ML).....	83
Figure 6.2.1 A series results of STM simulation for fill state ($V_s=-2$ V) and empty state ($V_s=+2$ V). The projection plane is placed on about 2 \AA above topmost chlorine.	87
Figure 6.2.2 A series results of fill state ($V_s=-2$ V) and empty state ($V_s=+2$ V) simulated STM images. The projection plane is placed on about 2 \AA above topmost chlorine.	88
Figure 6.3.1 (a) Contour map of NaCl overlaid with trajectories of $\nabla\rho$, and (b) Bader partition volume of our system.....	92
Figure 6.3.2 (a) Initial and (b) final states of the photoemission process. The effect of screening is shown by the increased occupation of the local valence band DOS in (b) compared to (a).	92
Figure 6.3.3 Net Bader charge ($q_{\text{bader}}-q_{\text{neutral}}$) and RCLS (relative to Si $2p$ bulk) for specified atoms. The final state results of Si $2p$ states are labeled by red word.....	93
Figure 6.3.4 (a) Detailed net Bader charge and (b)-(d) RCLS (relative to Si $2p$ bulk) in all of the surface atoms. Each the case includes thirty-six data points.....	94

Chapter 1 Introduction

1.1 Motivation

The implementation of top-down technologies with the aim of making miniaturized structures is about to reach certain limits. With reduced dimension, producing defect free device structures becomes increasingly difficult and expensive. The formation of nanostructures by atomic layer deposition (ALD) as a bottom-up approach is therefore a promising alternative for the fabrication of nanoscale devices.

Electrons confined in two-dimensional systems, such as interfaces and ultrathin films, are essential to low-dimensional physics. Without a doubt, the discovery of 2010 Nobel Prize-winner, graphene is the most famous two-dimensional material in recent years. Such a 2D quantum film exhibits many amazed material characteristic that had never been observed before. The physical properties of three dimension crystalline solid are well documented, dimensionality two is conspicuously absent among experimentally known crystals. It has long been tempting to try splitting 3D crystal into individual atomic layers; but it remained unclear whether free-standing atomic layers could exist in principle (thermodynamically unstable).

Alkali halides are the family of ionic compounds with simple chemical formula X^+Y^- . In standard room conditions dry alkali halides tend to form in Halite structure (space group: $Fm\bar{3}m$). Whether two dimensional alkali halides is a stable state has been widely discussed before. For example, on metal surface, alkali halides are known to grow in the form of large domains (approximately micrometers) of bilayers, but growth beyond the bilayer contents many small islands^{1,2}. Why the alkali halides thin films always follows double-layer growth mode still remains much unknown.

Hebenstreit *et al.*³ produced for the first time unusual adsorbate-free NaCl(111) thin film by subsequent adsorption of Na and Cl₂ on Al(111). It used to be widely believed that the surface energy of polar surfaces such as bulk-terminated (111) surfaces of NaCl-type ionic crystals is formally infinite, and such surfaces are unstable and do not exist in nature. Whether the NaCl(111) thin film surface can be “produce” is still in controversy.

The Si(100) has been widely used in the semiconductor industry. The reconstructive Si(100) surface rich in half-occupied dangling bonds that has very high chemical activity and electron mobility. Halogen molecules can be dissociated by dangling bonds without any extra energy, the reaction is spontaneous. The halogen saturated p(2x1) surface would become very stable and well ordered⁴. It would be a very good platform for observing growth behavior of ionic thin film. By utilizing the concept of self-limited reaction, we prepare a halogen-terminated ordered p(2x1) surface by using molecule halogen. Then, we deposit controlled amounts of alkali metal on the surface. The method has two expected advantages; first, halogen-saturated surface provides a good positioning for increasing lateral growth ratio. Second, by controlling the amount of alkali metal, step by step, we can directly observe surface transition with varying sodium coverage. The self-limit reaction process is schematically shown in Fig. 1.1.2.

In general, the lattice mismatch of less than 3% can effectively reduce interface stress that would be good for growing high-quality thin films. Therefore, we attempted to calculate bond length and energy in among of twelve kinds of different alkali halides as shown in Fig. 1.1.1; it tells us that most of alkali-halides in nature tend to form in three-dimension. However, for some case, 2D and 3D alkali-halides have only very small difference in paired bond energy. In those cases, the 2D alkali-halide

crystal might be a metastable even a stable state. Therefore, in consideration of their lattice matching, sodium chloride seems to be the best choice; Because, theoretically, the lattice mismatch of NaCl(3D)/Si(100) and NaCl(2D)/Si(100) is only +2.35% and -3.11% respectively. For the reasons, this thesis, we chose the Si(100) as a substrate, chlorine molecule as a precursors and sodium metal as a reagent. Unlike in the past, we employed the ALD method by using the sequential Cl and Na deposition. Entire experiment was carried out in an ultra high vacuum (UHV) under room temperature condition. The evolution of epitaxy process was examined by STM, XPS, and First principle simulation. By combination of experiment and theoretical computation, we are able to answer following issues.

1. Can we produce a NaCl film with only single layer in thickness?
2. Can the ALD method effectively increase lateral growth ratio?
3. If the answer for (2) is yes, what's the growth mechanism?
4. What correlations can be drawn about the bonding between Si, Cl, and Na in atomic level?
5. What kind of physical properties exist in surface and interface?

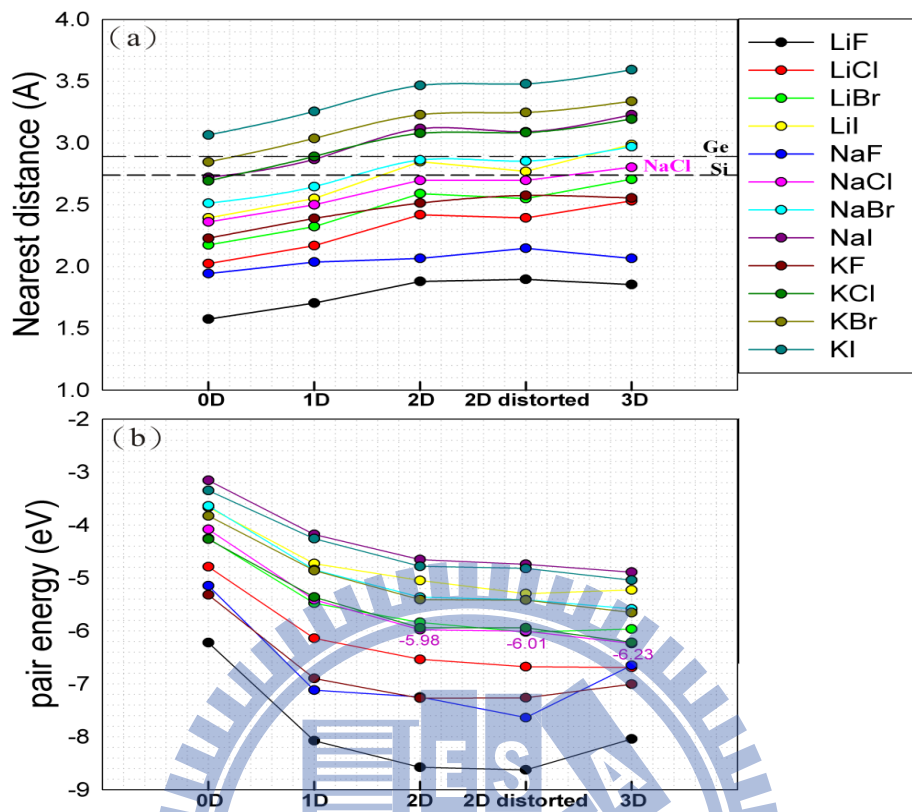
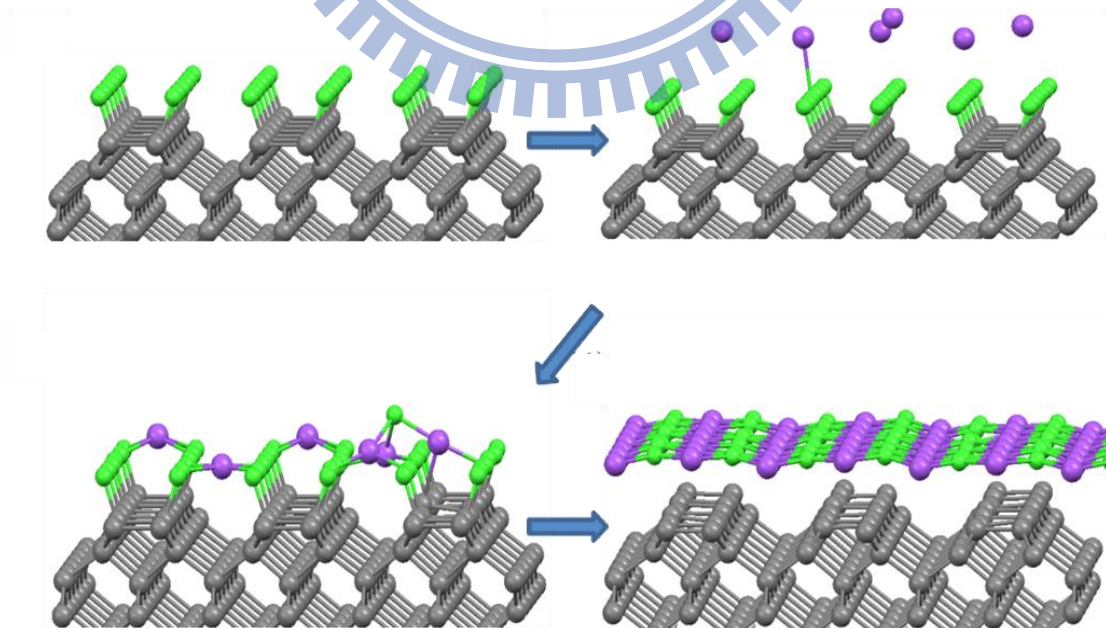


Figure 1.1.1 (a) Nearest distance and (b) normalized pair bond energy of various kinds of ionic solid from one (molecule) to three dimensions. The pair energy is calculated from the formula⁵: $E_{\text{pair}} \equiv (E_{\text{total}} - NE_{\text{iso-X}} - NE_{\text{iso-Y}}) / N_{\text{XY}}$



1.2 Si(100) surface reconstruction

Si(100) surface is the most widely used material in the semiconductor industry. Silicon in bulk is bounded by covalent bonding with the sp^3 orbital hybridization, and composed of two fcc sublattices with $1/4$ lattice dislocation (See Fig. 1.2.1). If one cleaves the silicon crystal along the (100) direction, two valence bonds of each Si atom at the exposed surface will be broken and transform into dangling bonds. As shown in Fig. 1.2.2 (a), every silicon atom in the surface has two dangling bonds and two valence bonds. In this 1×1 structure, the surface energy is too high to be stable. To reduce the numbers of the dangling bonds, the first layer atoms in the surface will be reconstructed. Upon reconstruction, two neighboring atoms form a strong sigma (σ) bond by combined one of the two dangling bonds. The top-layer atoms of the Si(100) surface dimerize to reduce the number of dangling bonds. These bonded pairs of Si atoms are called dimers. The amount of dangling bonds is reduced by 50 %. This establishes two characteristic directions on the surface, along the dimer row and perpendicular to the dimer. The parallel rows of the dimer bonds also reduce the overall surface energy. These remaining dangling bonds can further form a weak π bond, then the 1×1 structure of the surface have transformed into 2×1 structure, as shown in Fig. 1.2.3(b). Many studies reported that the perfect $p2 \times 1$ structure is not the ground state. The reconstructure of Si(100) is dependent on the temperature conditions⁶⁻⁹. As shown in Fig. 1.2.3, The DFT-LDA simulated result¹⁰ indicates that the equilibrium structure of the Si(100) surfaces cannot be adequately explained by a single static structure, namely its surface configuration is switching rapidly at room temperature. Thermal disordering renders the dimers uncorrelated, therefore, the ground state $c(4 \times 2)$ orderly structures can be observed only if the temperature lower

than 150K^{11, 12}.

As shown in Fig. 1.2.4, when preparing the Si(100) surface, the step structure formed by the cleavage along the (100) direction. The step height is about 1.36 Å (1/4 lattice constant). The dimer rows on the neighboring terraces are perpendicular, so steps of the terraces divide into two types. S_A is the steps where the dimer rows direction on the upper terrace parallel the step edge. S_B is the steps where the dimer rows direction on the upper terrace perpendicular the step edge.

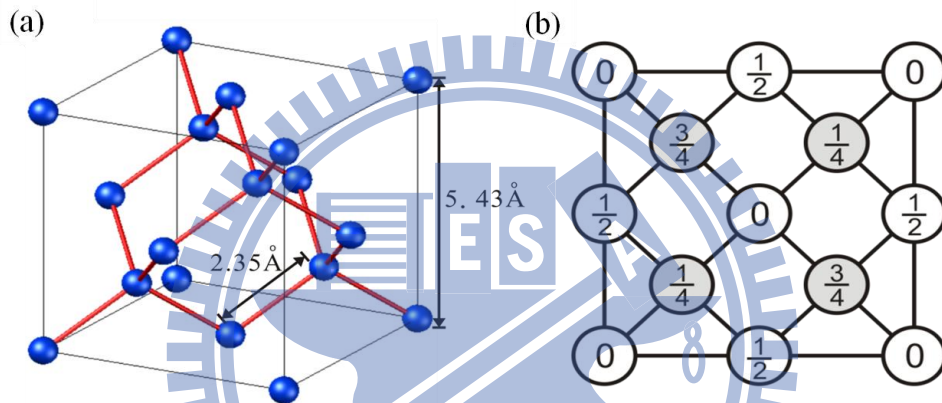


Figure 1.2.1 (a) Tetrahedral bond arrangement of diamond structure. (b) The down view of diamond structure, the fractions denoted the height of the atoms in units of a cubic edge.

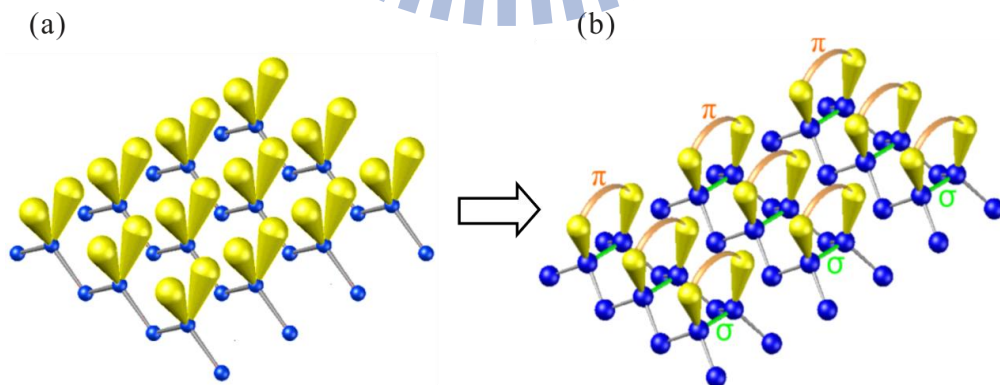


Figure 1.2.2 (a) The oblique view of the primary Si(100)-p(1x1) surface. Spheres are Si atoms and conoid sticks are dangling bonds. Each silicon atom has two valence bonds and two dangling bonds, and (b) after reconstructive Si(100)-p(2x1) surface.

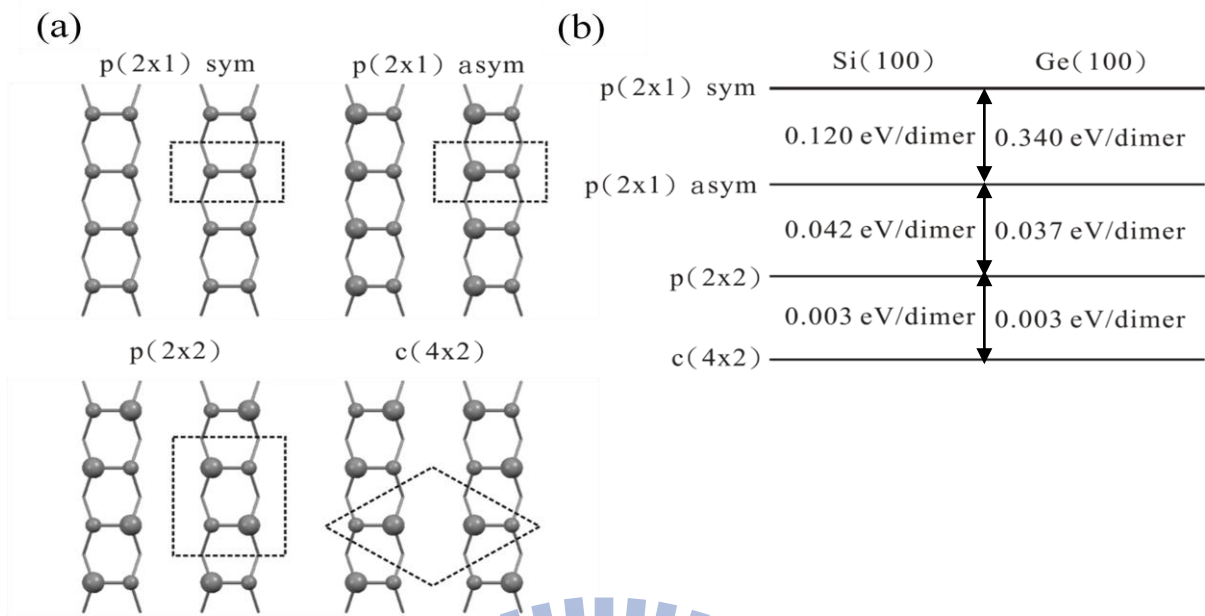


Figure 1.2.3 (a) Top view of four kinds of silicon reconstructions. Smaller spheres represent deeper atoms. (b) A schematic illustration of the order of magnitude of energy differences between different reconstructions of Si(100).

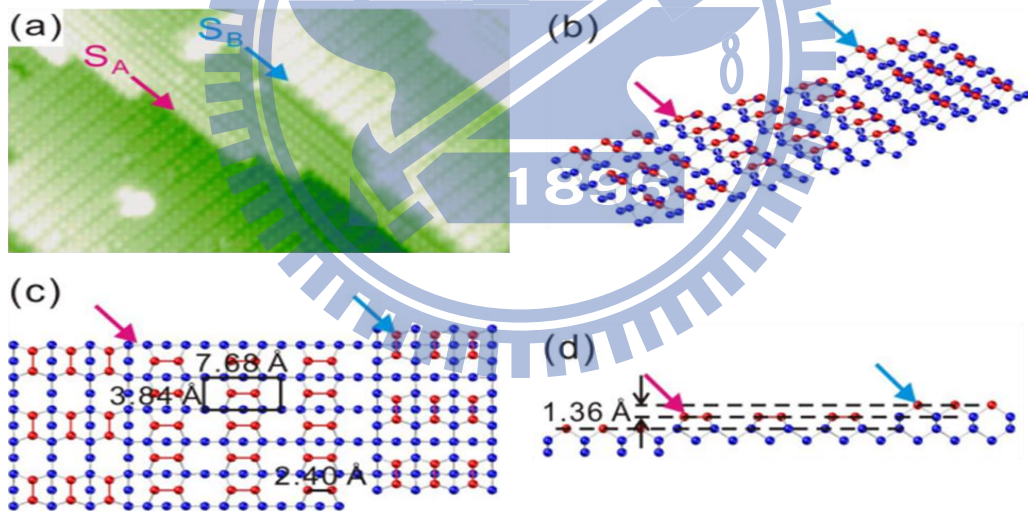


Figure 1.2.4 Step structures on the Si(100)-p(2x1) surface. (a) STM image of Si(100)-p(2x1) surface. The size is 15 nm×10 nm and $V_s = 2$ V. (b) Oblique, (c) top and (d) side views of step structures. S_A is the steps where the dimer rows direction on the upper terrace parallel the step edge. S_B is the steps where the dimer rows direction on the upper terrace perpendicular the step edge.

1.3 Madelung constant

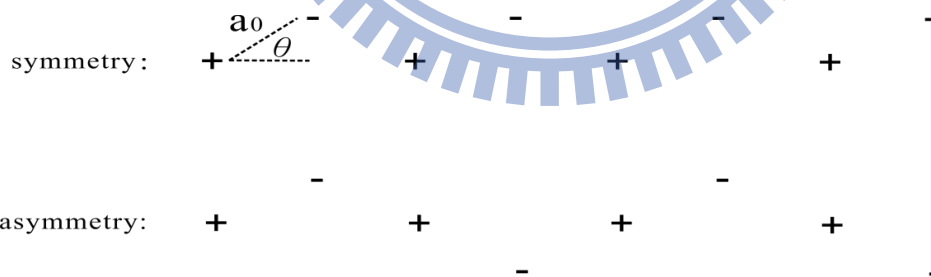
Madelung constant^{13, 14} is the most important factor for estimating the electrostatic potential of a single ion in a crystal by approximating the ions point charges. Because the anions and cations in an ionic solid are attracting each other by virtue of their opposing charges, separating the ions requires a large amount of energy. This energy must be given to the system in order to break the anion-cation bonds. The total energy:

$$E_{tot} = \frac{1}{4\pi\epsilon_0} \sum_{i \neq j} \frac{q_i q_j}{|\mathbf{r}_i - \mathbf{r}_j|} = -\alpha \frac{q^2}{4\pi\epsilon_0 a_0} \text{ where } a_0 \text{ is the nearest distance between anion and cation, } \alpha \text{ being the Madelung constant. For 1-D infinite collinear ionic solid:}$$

For 1-D infinite collinear ionic solid:

$$E_{col} = \frac{q^2}{4\pi\epsilon_0 a_0} (-2) \left(1 - \frac{1}{2} + \frac{1}{3} - \frac{1}{4} + \dots \right) = \frac{-q^2}{4\pi\epsilon_0 a_0} (2 \ln 2) \Rightarrow \alpha_{1D} = 1.3863 \quad (1.3.1)$$

If the anions and cations arrange in straight line but with a small angle as shown in the following schematic:



The total energy of two case can be calculated by principle of superposition.

$$E_{sym} = \frac{2q^2}{4\pi\epsilon_0 a_0} \left(\frac{1}{2 \cos \theta} + \frac{1}{4 \cos \theta} + \dots \right) \text{ (anions - anions)}$$

$$+ \frac{-2q^2}{4\pi\epsilon_0 a_0} \left(1 + \frac{1}{\sqrt{(3 \cos \theta)^2 + (\sin \theta)^2}} + \frac{1}{\sqrt{(5 \cos \theta)^2 + (\sin \theta)^2}} + \dots \right) \text{ (anions - cations)}$$

$$E_{\text{asym}} = \frac{2q^2}{4\pi\epsilon_0 a_0} \left(-1 + \frac{1}{2} - \frac{1}{\sqrt{(3\cos\theta)^2 + \sin^2\theta}} + \frac{1}{4} \dots \right) \quad (1.3.2)$$

By using the numerical method with distance-fixed constraint, we can obtain a “Madelung constant function” which depends on only the bending angle. As shown in Fig. 1.3.1. The result tells us that the anions-cations arranged in asymmetric non-collinear chain is relatively stable than another. In the other words, this arrangement mode is able to survive in higher distortion angle. For 2D case; we can calculate it by same method:

$$E_{\text{cop}} = \frac{q^2}{4\pi\epsilon_0 a_0} \left(\frac{-4}{1} + \frac{4}{\sqrt{2}} - \frac{8}{\sqrt{5}} + \frac{4}{2} + \frac{4}{\sqrt{8}} + \dots \right) \Rightarrow \alpha_{2D} = 1.6227$$

$$E_{\text{sym}} = \left(\frac{4}{2} + \frac{4\sqrt{2}}{4} + \frac{4}{4} + \dots \right) \text{ (anions - anions)}$$

$$+ \frac{-q^2}{4\pi\epsilon_0 a_0} \left(4 + \frac{4\sqrt{2}}{\sqrt{(3\cos\theta)^2 + (\sin\theta)^2}} + \frac{4}{\sqrt{(3\cos\theta)^2 + (\sin\theta)^2}} + \dots \right) \text{ (anions - cations)} \quad (1.3.3)$$

The result indicates that the Madelung constant in 2D system is more strongly depending on bending angle. In summary, the result tells us that the anion and cation they prefer to arrange in perfect collinear (1D) and coplanar (2D) configurations; but the “Madelung constant function” in asymmetric arrangement mode have just slightly decreasing with bending angle. From an electrostatics point of view, asymmetry arrangement can effectively reduce the electric dipole which makes the system relatively stable. For 3-D case, from the textbook : $\alpha_{3D} = 1.7475$.After a comparing, The Madelung constant is increasing with system dimension $\alpha_{1D}(1.386) \ll \alpha_{2D}(1.612) < \alpha_{3D}(1.748)$;which indicates larger degree of freedom of system result in more stable structure. However the argument is limited in complete electronic closed-shell model and constant distance constrain. In real systems,

electron transfer between anion-cation may not be integer. Bond length in lower dimension system also can be shrinking or expanding. Does the 2D ion film can be stable; the simple electrostatic model may no longer applicable for the question. Nevertheless, this calculation gives us some significant hint; completely free-standing 1D and 2D ionic system cannot exist in nature. But if a 1D or 2D ionic crystal be inhabited growing on a surface. In order to reduce surface, the anion-cation pair should prefer to arrange in anti-symmetry form instead of symmetry form.

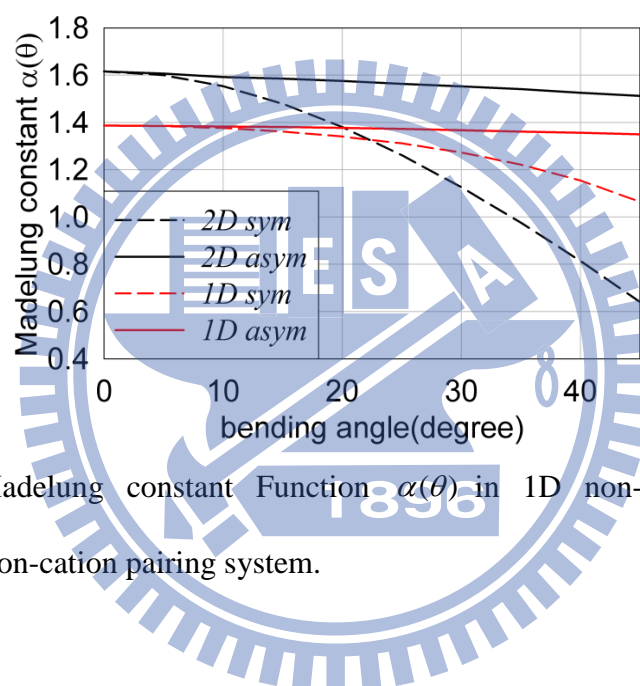


Figure 1.3.1 Madelung constant Function $\alpha(\theta)$ in 1D non-collinear and 2D non-coplanar anion-cation pairing system.

1.4 Literature Review

1.4.1 NaCl /Cu(111)

Typical alkali halide growth based on molecular beam epitaxy (MBE) using beams of ionically balanced molecular units for deposition has been reported to yield a double-layer growth mode^{15, 16}. NaCl /Cu(111) is the most remarkable system because it has much strange behavior and high application value, but only bilayer NaCl structure had been observed on Cu(111)^{17, 18}. Uniform and very large scale (micrometer) Sodium chloride would assemble itself on the surface (Fig. 1.4.1(a)), which provides a very nice platform for doing STM measurements. By the method, DOS of molecules could be decoupled from the substrate through an interlayer, namely the STM images would resemble closely the shape of the HOMO/LUMO of the free molecule. The Pentacene on NaCl/Cu(111) system is the most famous case¹⁹. As shown in Fig. 1.4.2, the insulator NaCl thin film would benefit to greatly enhance the sample resolution. Another unusual behavior, Fig. 1.4.3 shows a strong interface state density and it will possibly propagate to clean Cu(111) region. With varying sample bias, the surface reveals different DOS distribution. The observed metal induced gap state (MIGS) formation due to Moiré patterns is similar to the superlattice concept^{17, 20, 21} based on the idea of creating artificial, tunable 1D band gaps by growing a vertical lattice of alternating semiconductors. Whereas in semiconductor superlattices the band gaps can be tuned by the layer thicknesses during growth, Moiré'- pattern-induced band gaps can be tuned by the choice of lattice constant mismatch. This phenomenon shows a new way to tailor the properties of interface states for future applications. These possibilities can be further extended by controlled sequential growth of different dielectric materials. In contrast to surface

states, interface states are inherently protected by the dielectric adlayer and can even be studied under ambient conditions.

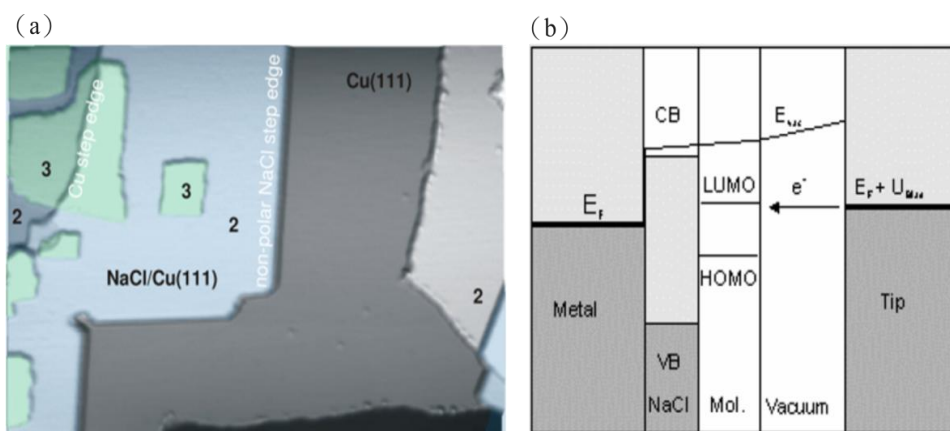


Figure 1.4.1(a) STM image of NaCl/Cu(111) taken at 320 K with the sample bias $V_s = -1.26$ V and the tunneling current of 230 pA. The scan size is 230 nm \times 160 nm. (b) Diagrammatic sketch of double barrier tunneling junction. (Cited from Gerhard Meyer, Jascha Repp, Peter Liljeroth IBM Zurich Research Laboratory).

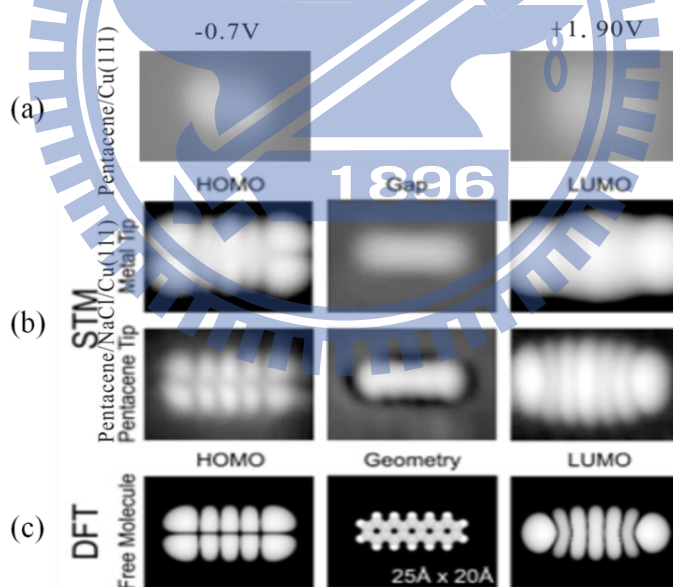


Figure 1.4.2. From top to bottom, (a) the experimental STM images acquired with pentacene on Cu (111) (without NaCl interlayer) and (b) STM images of pentacene on NaCl/Cu(111) surface with a metal and a pentacene tip, the images at bias voltages exceeding the HOMO (left) or LUMO (right) exhibit very pronounced features. (c) The results of theoretical calculations. (Cited from ¹⁹).

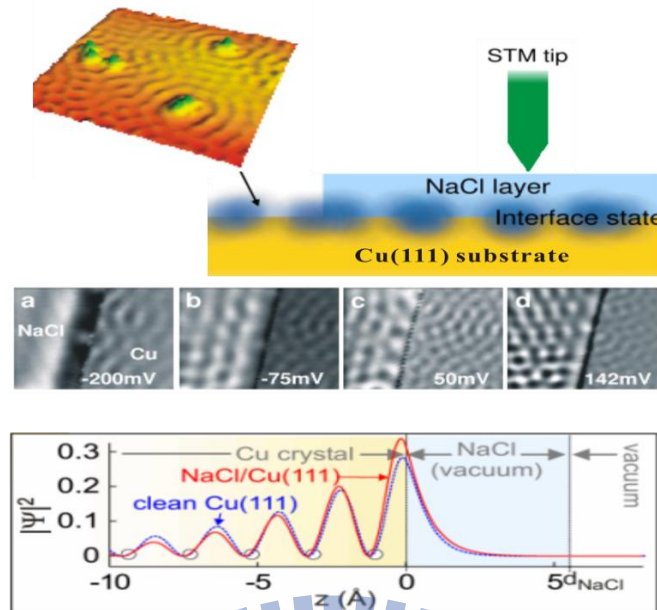


Figure 1.4.3 From top to bottom, a schema of MIGS between Cu(111) and NaCl thin film. Under various sample bias (a)-(d), which reveals different sort of Fermi wave. Bottom figure draws vertical charge density distribution. (Cited from Gerhard Meyer, Jascha Repp, Peter Liljeroth IBM Zurich Research Laboratory).

1.4.2 NaCl/Ge (100)

Thin NaCl films can be grown epitaxially on Si-Ge(100) with high quality under appropriate conditions. Gloeckler *et al.*¹⁵ demonstrated that NaCl grows on Ge(100) surface by using the MBE also results in bilayer NaCl. Fig. 1.4.4(b) displays a typical large-area STM image with various NaCl island sizes, between 30 and 320 Å in diameter, which are mostly one DL high. The island edges run predominantly along the [100] and the [110] directions of the Ge substrate, yielding 90° and 135° island corners. Lateral atomic resolution (see Fig. 1.4.4(b)) was obtained for NaCl islands of one DL height for slightly enhanced tunneling currents ($I_t=1.8$ nA), which force the tip closer to the surface. A well-resolved square lattice with a lattice constant of 4.0 Å is observed. From this lattice constant they conclude that only one type of ions (Na^+ or Cl^-) is imaged as white protrusions. They indicated that the tunneling current is

predominantly due to emission from Ge states through the NaCl layer. This is certainly due to the fact that the tunneling barrier is not only determined by the vacuum between tip and NaCl layer, but also by the NaCl layer itself, which does not provide the density of states between the Fermi energies of the tip and Ge substrate. They also executed a deep profile measurement as shown in Fig. 1.3.4(c), from which nominal heights of 3.8 ± 0.3 and 2.0 ± 0.3 Å are derived for the first (double) and the second (single) NaCl layers respectively. In summary, They have roughly described growth mode of NaCl/Ge(100) system.

Professor Shioh-Fon Tsay *et al*²², also reported a series of DFT calculation results for the system. By way of layer adsorption energies calculations (see Fig. 1.3.5(a)), they demonstrated that why NaCl grow on Ge(100) is also followed double layer growth mode. They indicated that only very weak coupling has existed between the interfacial Cl⁻ ions and the dimer up-Ge atom. Fig. 1.3.5(b) shows their electronic calculation result that reveals small quantities of Ge-Cl bonded states locate around -1 eV and large quantities Cl 3p state locate between -2 to -4 eV. The calculation results are totally consistent with the previous results of STM experiments. The white protrusions in STM image should be explained as an electron that emitted from silicon substrate.

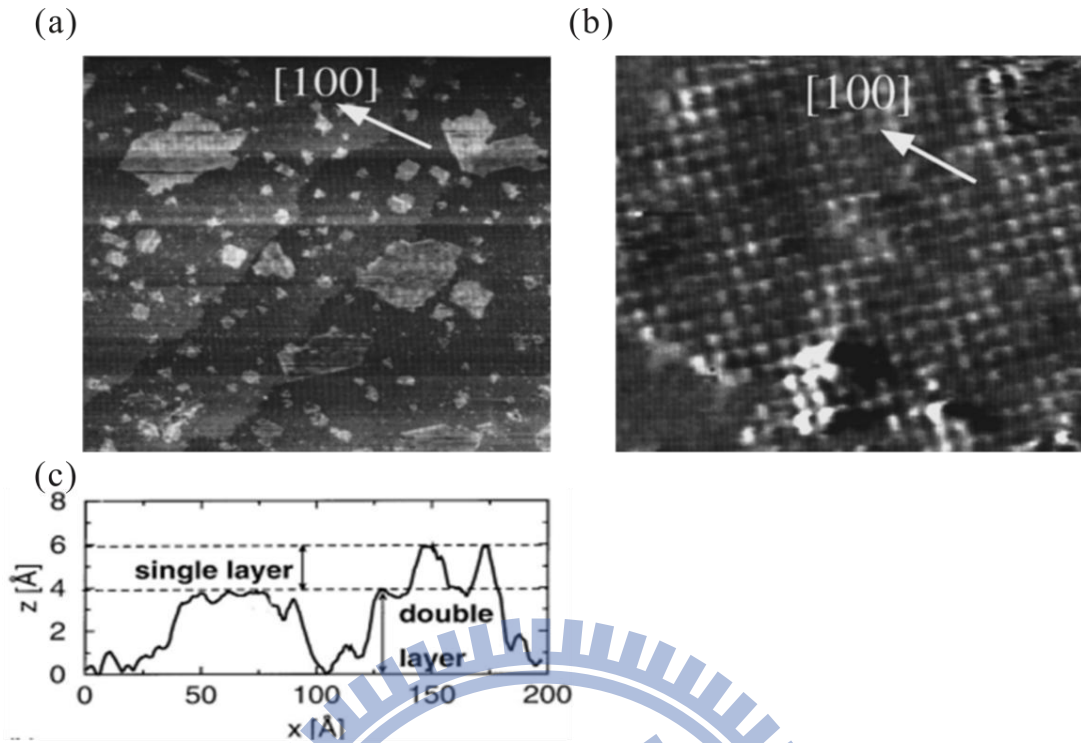


Figure 1.4.4 (a) Large-area STM scan ($1130 \times 1130 \text{ \AA}^2$) of NaCl on Ge(100). Nearly all NaCl islands have a height of one double layer ($V_s = -2.7 \text{ V}$, $I_t = 0.7 \text{ nA}$). (b) STM image ($98 \times 81 \text{ \AA}^2$) with atomic resolution of a NaCl layer of one double layer. The square lattice has a lattice constant of 4.0 \AA , and is oriented along the [110] and [-110] directions of the underlying Ge (100) surface ($V_s = -2.7 \text{ V}$, $I_t = 1.8 \text{ nA}$). (cited from ¹⁵)

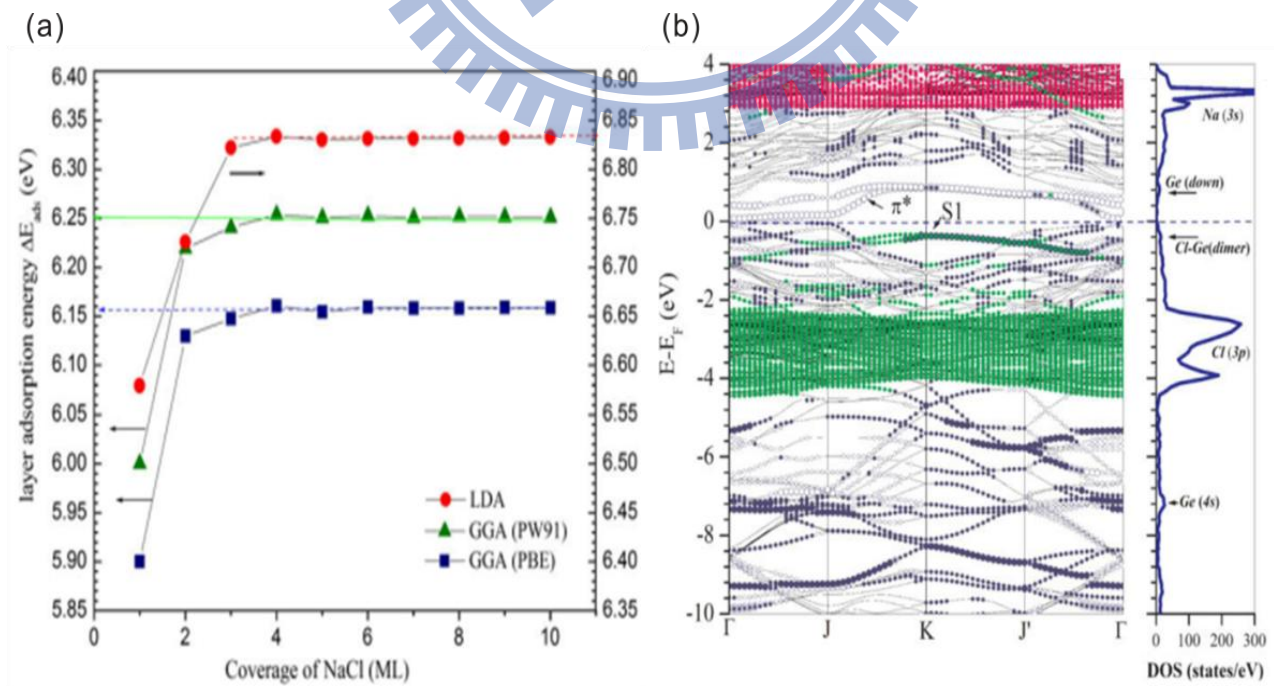


Figure 1.4.5 (a) Layer adsorption energies per 1×1 supercell for NaCl adsorbed on a Ge (100) surface ($\Delta E_{\text{ads}}(n) \equiv [E_{\text{NaCl/Ge}}(n-1) + E_{\text{Na}} + E_{\text{Cl}} - E_{\text{NaCl/Ge}}(n)]$).

(b) The electronic band structure and PDOS for 10 ML NaCl/Ge(100) surface. The states corresponding to the Na and Cl are indicated by pink and green solid circles, respectively, and that of the dimer up-Ge and down-Ge are represented by the full and empty blue circles, respectively.(cited from ²²)

1.4.3 NaCl/Si (100)

Maximilian Amsler *et al*²³ had calculated a series of simulation for researching the structural stability of NaCl/Si(100) system. As shown in Fig. 1.4.6, two sort of adsorbed configurations had been considered. They indicated the most favored adsorption type was found to be four NaCl dimers on top of lower Si atoms. This is in agreement with the positive balance of energy when the dissociation of the (NaCl)₄ cube into dimers and the formation of Cl–Si bonds is taken into account. However, this trend changes if larger NaCl clusters were adsorbed. The increasing dimerization energy with respect to the cluster size and the formation of stable cuboid geometries of isolated NaCl clusters suggest that the adsorption without dissociation is preferred over the dimer adsorption for larger clusters. Because in the limit of bulk NaCl, the dissociation into dimers requires 3.25 eV per molecule, which is considerably larger than the 2.31 eV released during a single dimer adsorption on the silicon surface. In the other words, they suggested two kind of adsorption behavior may synchronize on the Si(100) surface, which kind would happen that depends on the NaCl particle size. Besides, our group also did a series of experiment by using the MBE epitaxy for this system²⁴. The results as shown in Fig. 1.3.7 and Fig. 1.3.8. As $\theta < 0.4$ ML, the XPS and STM results both indicated that more than half of the adsorbed NaCl dissociates

to form Si-Cl and adsorbed Na. A wetting adlayer is formed after the deposition of 0.65 ML NaCl. This adlayer consists of Si-Cl, adsorbed Na, NaCl networks, and isolated dangling bonds. Many isolated dangling bonds are grouped into small patches, which exhibit the (2×4) or (2×2) ordered structure. Further deposition above 0.65 ML results in the appearance of double-layer NaCl islands which grow in size on top of the first adlayer (see Fig. 1.3.8). Up to $\theta = 1.8$ ML, the isolated dangling bonds remain at the interface between the NaCl film and the silicon substrate. On the whole, our experimental data is totally in a good agreement with previous theoretical paper.

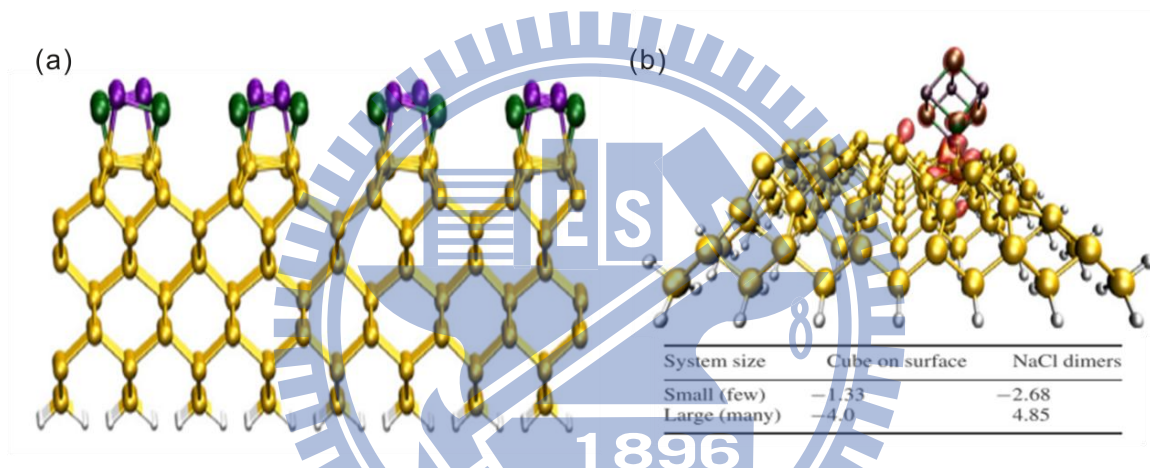


Figure 1.4.6 (a) NaCl dimers on a Si(100)-c(4 \times 2) reconstruction. The silicon surface reconstruction disappeared and the pattern of NaCl dimers mimics the original silicon surface reconstruction. (b) (NaCl)₄ cube adsorbed in a hole of the silicon model tip. The green (dark gray large sphere) and purple (dark gray small sphere) spheres denote Cl and Na atoms respectively. Adsorption energy of them also listed at lower right corner.(cited from ²³)

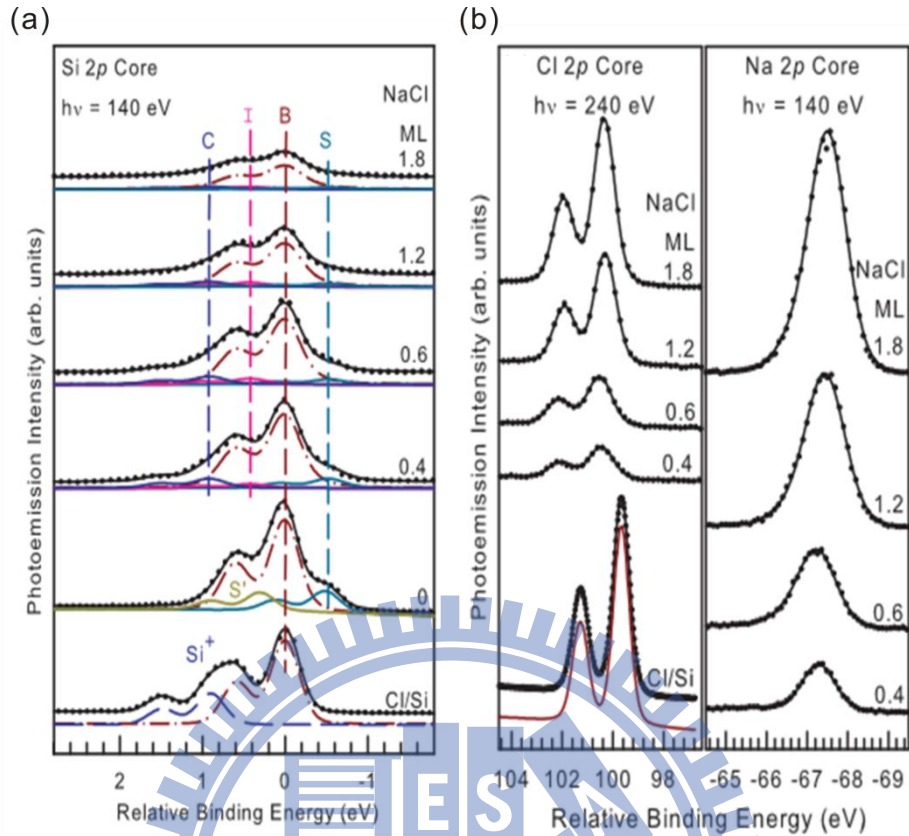


Figure 1.4.7 (a) Si 2*p* core-level photoemission spectra (dots) of Si(100) surface with various amounts of NaCl deposition, as specified. The solid curves fit to the spectra. The curves labeled B, S, I, and Si⁺ are the results, respectively, of the decomposition of the Si 2*p* spectra into contributions from the bulk, the clean surface, the interface layer, and the Si-Cl species. The energy zero refers to the bulk position. (b) Cl 2*p* (left), and Na 2*p* core-level photoemission spectra (dots) corresponding to Si 2*p*. All the energy scales were relative to Si 2*p* bulk for eliminate the band-bending effect.(cited from ²⁴)

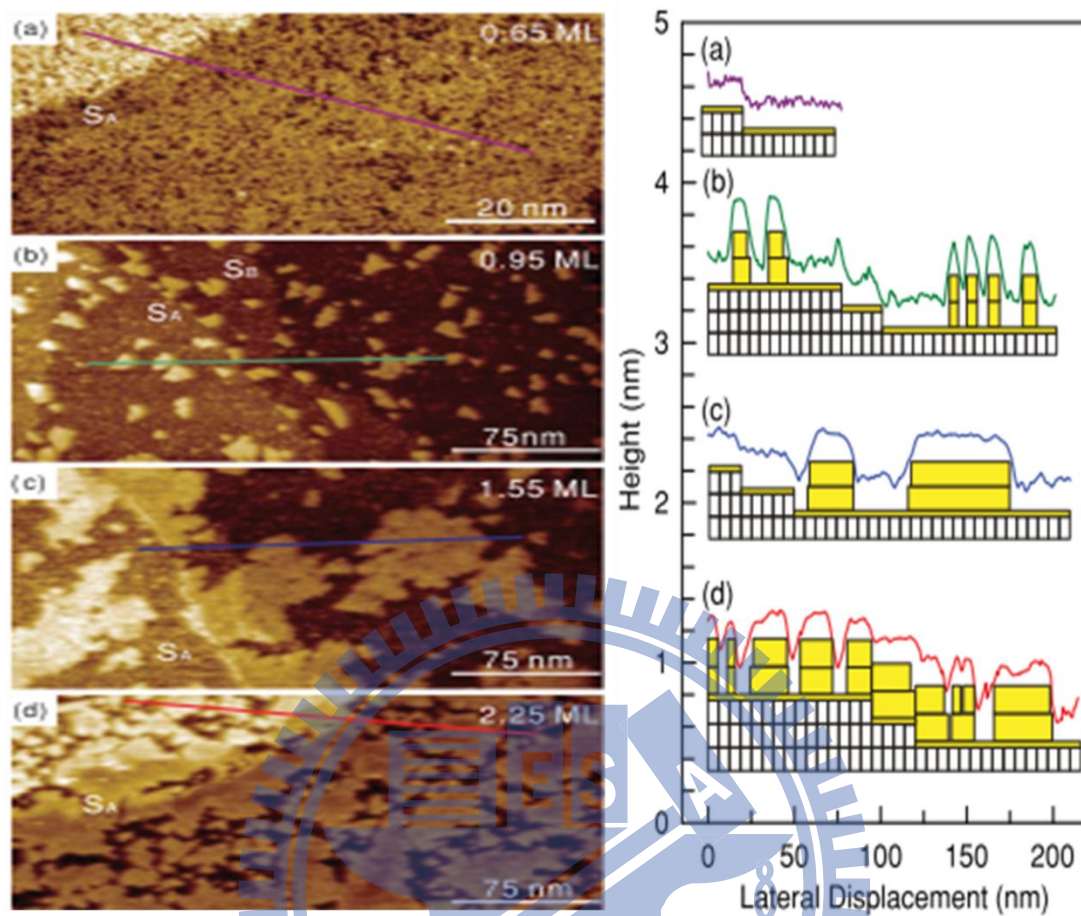


Figure 1.4.8 (a) Filled-state STM images showing morphology evolution with various NaCl coverages on Si(100), as labeled. All images are obtained at room temperature with $I_t = 0.23$ nA and $V_s =$ (a) -2.05 , (b) -2.3 , (c), and (d) -2.8 V. The images cover an area of about (a) $80 \text{ nm} \times 40 \text{ nm}$, and (b)–(d) $300 \times 150 \text{ nm}$. The apparent topographic height profiles along the line segments and schematics of grown NaCl nanofilms were shown in right side. The thin yellow (light gray) layer above the substrate depicts the first adlayer. A thick yellow (light gray) rectangle indicates an NaCl monolayer. (cited from ²⁴)

Chapter 2 Theory

In this chapter, we introduce several theoretical background and approximate method that used in our first principle calculations. At the first, we introduce the Born-Oppenheimer approximation, and how does it work for separating equations of motion of nuclei and electron. After that, we introduce Hartree-fork theory and show how it simplifies the multi-electronic complicated system to single electron model. Furthermore, we will introduce the Density Functional Theorem (DFT), and illustrate how to estimate exchange correlation energy. The last section, we review the Bloch's theory and illustrates that how to estimate density of states through the different smearing methods.

2.1 Born-Oppenheimer approximation

The N-electron Schrödinger equation is usually extremely complicated because of too many coupling items:

$$\hat{H} = \hat{K}_N + \hat{K}_e + \hat{V}_{NN} + \hat{V}_{Ne} + \hat{V}_{ee} \quad (2.1.1)$$

Considering both the atomic nucleus and the electronic movement will cause the question to be extremely complicated. In general, we always simplify the N-electron problem by using the famous Bohn-Oppenheimer (BO) approximation^{25, 26}, which assumes that electron is fast-moving particle with frozen nucleus because their enormous mass ratio $m_e/m_m=1/1836$. Therefore we are able to separately solve the Schrödinger equation of electron:

$$\hat{H}_e = \hat{K}_e + \hat{V}_{Ne} \quad \hat{H}_e \psi_e = E_e \psi_e \quad (1_e K \quad N \bar{N} \bar{e}) ,$$

$$U(\mathbf{r}) = E_e(\mathbf{r}) + V_{NN}(\mathbf{r}) \quad (2.1.2)$$

Where $U(\mathbf{r})$ is called potential energy function or potential energy surface (PES). In the general molecular orbital theory (MO), the molecule structure will correspond with minimum point on PES²⁷.

2.2 Hartree–Fock approximation

The Hartree–Fock algorithm^{28, 29} is frequently used for solving the multi-electron atom or molecule time-independent Schrödinger equation. The N-electron Hamilton of a system can be written as:

$$H = \sum_{i=1}^N \frac{p_i^2}{2m} + \sum_{i=1}^N V_{ext}(\mathbf{r}_i) + \frac{1}{2} \sum_{i=1}^N \sum_{j=1}^N \frac{e^2}{|\mathbf{r}_i - \mathbf{r}_j|} \quad (2.2.1)$$

Assuming the total wavefunction can be simplified as a production of individual wavefunction. $\psi(\mathbf{r}_1, \mathbf{r}_2, \dots, \mathbf{r}_N) = \phi_1(\mathbf{r}_1)\phi_2(\mathbf{r}_2)\dots\phi_N(\mathbf{r}_N)$ (2.2.2)

And then, we have to consider exchange symmetry of fermions' electron thus total wave function should be written as Slater determinant:

$$\psi = \frac{1}{\sqrt{N!}} \begin{vmatrix} \phi_1(q_1) & \phi_2(q_1) & \dots & \phi_N(q_1) \\ \phi_1(q_2) & \phi_2(q_2) & \dots & \phi_N(q_2) \\ \vdots & \vdots & \ddots & \vdots \\ \phi_1(q_N) & \phi_2(q_N) & \dots & \phi_N(q_N) \end{vmatrix} \quad (2.2.3)$$

thus the total energy of the system should write as :

$$E = \langle \psi | \hat{H} | \psi \rangle = \sum_i \int dq_1 \phi_i^*(q_1) H_i(q_1) \phi_i(q_1) + \frac{1}{2} \sum_{i \neq j} \int dq_1 dq_2 \frac{|\phi_i(q_1)|^2 |\phi_j(q_2)|^2}{|\vec{r}_i - \vec{r}_j|} - \frac{1}{2} \sum_{i \neq j} \int dq_1 dq_2 \frac{\phi_i^*(q_1) \phi_i(q_2) \phi_j^*(q_2) \phi_j(q_1)}{|\vec{r}_1 - \vec{r}_2|} \quad (2.3.4)$$

Through the variational principle, for the ground state, we have $\delta \frac{\langle \psi | H | \psi \rangle}{\langle \psi | \psi \rangle} = 0$.

In order to ensure each single electron wavefunctions that satisfies normalization condition. We introduce the Lagrange multiplier λ_{ij} , and let

$$\delta \left[E - \sum_{i,j} \lambda_{ij} (\langle \phi_i | \phi_j \rangle - \delta_{ij}) \right] = 0 \quad (2.2.5)$$

Thus we have

$$\sum_j \hat{h}_{ij}(q_1, \{\phi_k\}) \phi_j(q_1) = \sum_j \lambda_{ij} \phi_j(q_1), \quad \sum_j \hat{h}_{ij}^*(q_1, \{\phi_k\}) \phi_j^*(q_1) = \sum_j \lambda_{ji} \phi_j^*(q_1) \quad (2.2.6)$$

Where $\hat{h}_{ij}(q_1, \{\phi_k\}) = \left[-\frac{\hbar^2}{2m} \nabla_1^2 + V_{ion}(\mathbf{r}_1) \right] \delta_{ij} + \sum_k \int dq_2 \frac{|\phi_k(q_2)|^2}{|\vec{r}_1 - \vec{r}_2|} \delta_{ij} - \int dq_2 \frac{\phi_j^*(q_2) \phi_i(q_2)}{|\vec{r}_1 - \vec{r}_2|}$

Because \hat{h} is a Hermitian operator $\hat{h}_{ij} = \hat{h}_{ji}^\dagger$, thus we have $\sum_j (\lambda_{ji}^* - \lambda_{ij}) \phi_j = 0$, where

λ_{ij} is a Hermitian matrix. It can be diagonalized through a unitary operator:

$$(u\lambda u^\dagger)_{ij} = E_i \delta_{ij} \Rightarrow \phi_i = \sum_j u_{ij} \phi_j \quad (2.2.8)$$

The new single electron ground state wavefunction should satisfy the equation:

$$\sum_j h_{ij}(q_1, \{\phi_k\}) \phi_j(q_1) = E_i \phi_i(q_1) \quad (2.2.9)$$

$$h_{ij}(\mathbf{r}, \{\phi_k\}) = \left[-\frac{\hbar^2}{2m} \nabla^2 + V_{ion}(\mathbf{r}) \right] \delta_{ij} + \sum_k \int d\mathbf{r}' \frac{|\phi_k(\mathbf{r}')|^2}{|\mathbf{r} - \mathbf{r}'|} \delta_{ij} - \int d\mathbf{r}' \frac{\phi_j^*(\mathbf{r}') \phi_i(\mathbf{r}')}{|\mathbf{r} - \mathbf{r}'|} \delta_{j/i} \quad (2.2.10)$$

(Hartree) (exchange)

This is known as Hartree-Fock equation, the third term generally so-called “screening potential” or Hartree potential, which represents effective local potential contributed between electrons in a mean-field theory description. It could be solve by standard self-consistent procedure. The last term is the exchange potential which is a very complicated nonlocal term; in general, people didn’t directly calculate this term, but replace by some approximation. However, Hohenberg and Kohn suggested that the

problem really is the many-electron wavefunction that is too complicated to deal with Hartree-Fock theory in a variational approach. The primary reason is that we cannot describe the real system with 10^{23} variables. They suggested chose an alternative electron density as their fundamental variable. The K-S theory based on BO approximation and H-F self-consistent field theory and associate with exchange and correlation functional not only make the calculation of large electron system feasible but also greatly improve accuracy of simulation.

2.3 Density Functional Theory

The first practical density functional theory (DFT) published by Kohn and Sham^{30,31} since 1965, it is widely applied for physical and chemical researching. It is an extremely successful approach for the description of ground state properties of metals, semiconductors, and insulators. The success of density functional theory (DFT) not only encompasses standard bulk materials but also complex materials such as organic Polymer, carbon nanotube, and graphene³². Numerous material properties such as bonding types, magnetic moments, band structure, dynamic, and optical character has been precisely described by DFT in the past several decades. The main concept of DFT is to describe an interacting system of fermions through its charge density distribution.

The most important concept of DFT is the ground properties of a many electron system are uniquely determined by its electron density $n(\mathbf{r})$. All ground physical quantity of the system can be derived by functional calculation $E[n(\mathbf{r})]$, $T[n(\mathbf{r})]$..etc
The general proof as following demonstration:

Hamilton of a system can be write as :

$$H = \sum_{i=1}^N \frac{p_i^2}{2m} + \sum_{i=1}^N V_{ext}(\mathbf{r}_i) + \frac{1}{2} \sum_{i=1}^N \sum_{j=1}^N \frac{e^2}{|\mathbf{r}_i - \mathbf{r}_j|} \quad (2.3.1)$$

Suppose there are two potential V_1 and V_2 have the same electron density $n(\mathbf{r})$, but $V_1 \neq V_2 + \text{constant}$ and $\psi_1 \neq \psi_2$. Suppose the ground state is nondegenerate, then

$$\langle \psi_1 | H_1 | \psi_1 \rangle < \langle \psi_2 | H_2 | \psi_2 \rangle; H_1 = H_2 + V_1 - V_2$$

$$E_1 < \langle \psi_2 | \hat{H}_2 | \psi_2 \rangle + \langle \psi_2 | V_1 - V_2 | \psi_2 \rangle = E_2 + \int d\mathbf{r} (V_2 - V_1) n(\mathbf{r})$$

$$\int d\mathbf{r}_1, \dots, \int d\mathbf{r}_N^3 (V_1(\mathbf{r}_1) - V_2(\mathbf{r}_1)) |\psi(\mathbf{r}_1, s_1, \mathbf{r}_2, s_2, \dots, \mathbf{r}_N, s_N)|^2 = \int d\mathbf{r}_1 (V_1(\mathbf{r}_1) - V_2(\mathbf{r}_1)) n(\mathbf{r}_1)$$

$$\Rightarrow E_2 < \langle \psi_1 | \hat{H}_1 | \psi_1 \rangle + \langle \psi_1 | V_1 - V_2 | \psi_1 \rangle = E_1 + \int d\mathbf{r} (V_2 - V_1) n(\mathbf{r})$$

$$E_2 - E_1 < \int d\mathbf{r} (V_1 - V_2) n(\mathbf{r}) < E_2 - E_1 \quad \leftarrow \text{contravention}$$

(2.3.2)

$$\therefore n_1(\mathbf{r}) = n_2(\mathbf{r}) \Rightarrow V_1 = V_2 + \text{constant}$$

The great idea largely reduced complexity of unknown systems, and successfully convert the problem from 3N dimension wavefunction expansion to only three dimension density $n(\mathbf{r})$ expansion. As in the Schrödinger equation, the density-functional approximation can be summarized as a sequence: $n(\mathbf{r}) \Rightarrow \psi(\mathbf{r}_1, \mathbf{r}_2, \dots, \mathbf{r}_N) \Rightarrow V(\mathbf{r})$

Although this sequence describes the conceptual picture of DFT, but it does not really represent what is done in actual applications of it, which typically implement along rather different line, and do not make explicit use of many-body wave functions. It's only a conceptual representation. The real DFT base on Hartree-Fock approximation as an effective single-body theory which described by Kohn-Sham equation. The ground state total energy of a system can write as:

$$E_G[n] = T[n] + \int d\bar{\mathbf{r}} n(\bar{\mathbf{r}}) V(\bar{\mathbf{r}}) + \frac{1}{2} \iint \frac{n(\bar{\mathbf{r}}) n(\bar{\mathbf{r}}')}{|\bar{\mathbf{r}} - \bar{\mathbf{r}}'|} d\bar{\mathbf{r}} d\bar{\mathbf{r}}' + E_{xc}[n] \quad (2.3.3)$$

which $T_s[n]$, $E_{xc}[n]$, $V_s(\mathbf{r})$ and $n(\mathbf{r})$ still unknown term, Kohn and Sham they suggested a practicable scheme to determine them. According to the Hohenberg-Kohn theory, given a known $V_s(\mathbf{r})$ corresponds to unique $n(\mathbf{r})$, as the Hartree-Fock algorithm we introduce a Lagrange multiplier λ to ensure norm conserve condition.

$$\delta \left(E_G(n, V) - \lambda \left(\int d\mathbf{r}' n(\mathbf{r}') - N \right) \right) = 0 \quad (2.3.4)$$

The total charge density can be calculated by linear combination of inner product of N non-interaction wavefunctions: $n(\mathbf{r}) = \sum_{i=1}^N |\phi_i|^2$, $\int d\mathbf{r} \phi_i^*(\mathbf{r}) \phi_j(\mathbf{r}) = \delta_{ij}$

By using the variation method, we have:

$$\delta \left(E_G(n, V) - \sum_{i,j} \lambda_{ij} \left(\int d\mathbf{r} \phi_i^*(\mathbf{r}) \phi_j(\mathbf{r}) - \delta_{ij} \right) \right) = 0 \quad (2.3.6)$$

$$\int d\mathbf{r} \sum_{i=1}^N \delta \phi_i^*(\mathbf{r}) \left\{ \frac{\delta n(\mathbf{r})}{\delta \phi_i^*(\mathbf{r})} \frac{\delta E_G[n, V]}{\delta n(\mathbf{r})} - \sum_{j=1}^N \lambda_{ij} \phi_j(\mathbf{r}) \right\} = 0 \Rightarrow \frac{\delta n(\mathbf{r})}{\delta \phi_i^*(\mathbf{r})} \frac{\delta E_G[n, V]}{\delta n(\mathbf{r})} - \sum_{j=1}^N \lambda_{ij} \phi_j(\mathbf{r}) = 0$$

$$\int d\mathbf{r} \sum_{i=1}^N \delta \phi_i(\mathbf{r}) \left\{ \frac{\delta n(\mathbf{r})}{\delta \phi_i(\mathbf{r})} \frac{\delta E_G[n, V]}{\delta n(\mathbf{r})} - \sum_{j=1}^N \lambda_{ji} \phi_j^*(\mathbf{r}) \right\} = 0 \Rightarrow \frac{\delta n(\mathbf{r})}{\delta \phi_i(\mathbf{r})} \frac{\delta E_G[n, V]}{\delta n(\mathbf{r})} - \sum_{j=1}^N \lambda_{ji} \phi_j^*(\mathbf{r}) = 0 \quad (2.3.7)$$

From the eq (2.3.3) we have:

$$\frac{\delta E_G}{\delta n(\mathbf{r})} = \frac{\delta T[n]}{\delta n(\mathbf{r})} + \int d\mathbf{r}' \frac{n(\mathbf{r}')}{|\mathbf{r} - \mathbf{r}'|} + \frac{\delta E_{xc}}{\delta n(\mathbf{r})} + V(\mathbf{r}) \quad (2.3.8)$$

Rewriting the $T[n] = T_s[n] + (T[n] - T_s[n])$, where $T_s[n] = \sum_{i=1}^N \int d\bar{r} \phi_i^* (-\nabla^2) \phi_i$

.The unknown $(T[n] - T_s[n])$ term can be classified into new exchange correlation term

$E_{xc}[n]$.

$$\frac{\delta T_s}{\delta \phi_i^*(\mathbf{r})} = \sum_{i=1}^N (-\nabla^2) \phi_i(\bar{r}) \quad \text{and} \quad \frac{\delta T_s}{\delta \phi_i(\bar{r})} = \sum_{i=1}^N (-\nabla^2) \phi_i^*(\bar{r}) \quad (2.3.9)$$

Similarly, through the unitary operation, let $\varphi_i = \sum_j u_{ij} \phi_j$, the many-electron wavefunction of the system may be constructed as a Slater determinant of the Kohn-Sham orbital. Finally we can obtain the standard Kohn-Sham equation:

$$\left[-\nabla^2 + V_{ion}(\mathbf{r}) + V_H[n(\mathbf{r})] + V_{xc}[n(\mathbf{r})] \right] \varphi_i(\mathbf{r}) = E_i \varphi_i(\mathbf{r}) \quad (2.3.10)$$

$$\text{Where } V_H[n(\mathbf{r})] = \int d\mathbf{r}' \frac{n(\mathbf{r}')}{|\mathbf{r} - \mathbf{r}'|} \quad (\text{Hartree}) \quad (2.3.11)$$

$$V_{xc}^{GGA}[n(\mathbf{r})] = \int n(\mathbf{r}) \bar{\epsilon}_{xc}[n(\mathbf{r})] F_{xc}[n(\mathbf{r}), \nabla n(\mathbf{r})] d\mathbf{r} \quad (\text{exchange-correlation}) \quad (2.3.12)$$

In finite temperature, the occupation numbers of electron comply with Fermi-Dirac distribution, thus the electron density can be augmented³³:

$$n(\mathbf{r}) = \sum_{i=1}^N \frac{1}{\exp[(E_i - \mu) / k_B T] + 1} |\varphi_i|^2 \quad (2.3.13)$$

If the exchange correlation potential is known, we can calculate the ground state wavefunction φ and electron density $n(\mathbf{r})$ through the self-consistent iteration loop³⁰ (see Fig. 2.3.1):

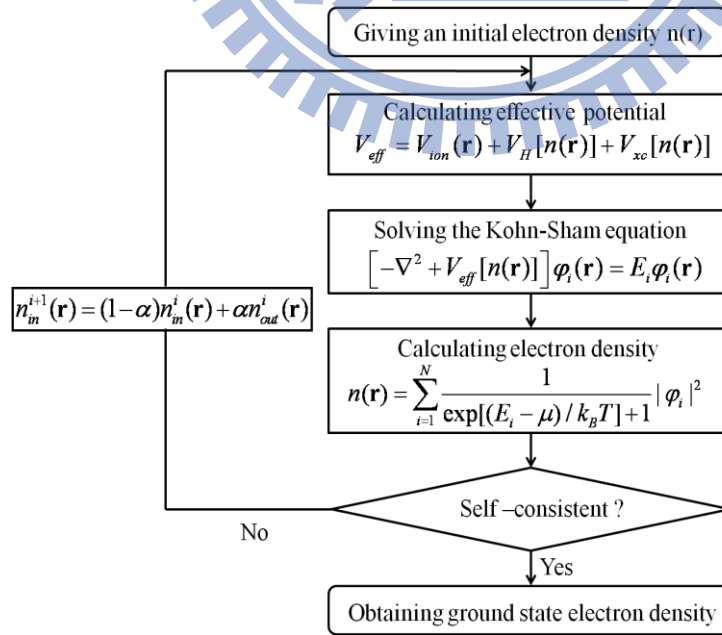


Figure 2.3.1 Flowchart of self-consistent loop

2.4 Exchange-Correlation Functional

The Kohn-Sham equations are thus far exact; no approximations have yet been made. We have simply mapped the fully interacting system onto an auxiliary non-interacting system that yields the same ground state density. As mentioned before, several unknown many-body interaction energy totally attributed into exchange correlation energy:

$$E_{xc}[n(\mathbf{r})] = T[n(\mathbf{r})] - Ts[n(\mathbf{r})] + E_{ee}[n(\mathbf{r})] - E_H[n(\mathbf{r})] \quad (2.4.1)$$

where $E_{ee}[n(\mathbf{r})]$ and $T[n(\mathbf{r})]$ are the real electron-electron interaction energies and exact kinetic respectively. Physically, this term can be interpreted as containing the contributions of detailed exchange and correlation to the system energy. The definition above is such that it ensures that the Kohn-Sham formulation is exact. But directly calculate this term is very difficult work, thus we must introduce an approximate functional to substitute that.

We can divide the density of the N-1 electron system into the total density $n(\mathbf{r})$, and to add an exchange-correlation hole let $\bar{n}(\mathbf{r}_0, \mathbf{r}) = n(\mathbf{r}) + h(\mathbf{r}_0, \mathbf{r})$. where $h(\mathbf{r}_0, \mathbf{r})$ should satisfy locality condition: $\lim_{|\mathbf{r}-\mathbf{r}_0| \rightarrow \infty} h(\mathbf{r}_0, \mathbf{r}) = 0$, obeys Pauli Exclusion Principle

$$\lim_{|\mathbf{r}-\mathbf{r}_0| \rightarrow 0} h(\mathbf{r}_0, \mathbf{r}) = -n(\mathbf{r}) \quad , \text{ and the hole contains negative one electron } \int h(\mathbf{r}_0, \mathbf{r}) d\mathbf{r} = -1$$

The exchange hole affects electrons with the same spin and accounts for the Pauli principle. In contrast, the correlation-hole accounts for the Coulomb repulsion of electrons with the opposite spin. It is short range and leads to a small redistribution of charge. The correlation hole contains empty charge: $\int h_c(\mathbf{r}_0, \mathbf{r}) d\mathbf{r} = -1$. There are two

common approximations in used : the local density approximation (LDA)³⁴, and the generalized gradient approximation (GGA)^{35, 36}. The simplest approximation is the LDA, It assumes that the exchange-correlation energy at a point in space is simply equal to the exchange-correlation energy of a uniform electron gas that has the same density at the point. Thus we can write:

$$E_{xc} = [n(\mathbf{r})] = \int \varepsilon_{xc}(\mathbf{r})n(\mathbf{r})d\mathbf{r} \quad , \quad V_{xc}(\mathbf{r}) = \frac{\delta E_{xc}[n(\mathbf{r})]}{\delta n(\mathbf{r})} = \frac{\partial [n(\mathbf{r})\varepsilon_{xc}(r)]}{\partial n(\mathbf{r})} \quad (2.4.2)$$

where $\varepsilon_{xc}(r) = \bar{\varepsilon}_{xc}[n(\mathbf{r})]$. Assuming that the exchange-correlation energy is purely local. The most common parametrisation in use for $\bar{\varepsilon}_{xc}[n(\mathbf{r})]$ is that of Perdew and Zunger³⁷ form, which is based upon the quantum Monte Carlo calculations of Ceperley and Alder³⁸ on homogeneous electron gases at various densities; the parameterizations provide interpolation formula linking these results. The LDA ignores corrections to exchange-correlation energy due to inhomogeneities in the electron density about \mathbf{r} . It may seem surprising that this is as successful as it is given the severe nature of the approximation in use; to large extent, it appears that this is due to the fact that the LDA respects the sum rule, that is, that exactly one electron is excluded from the immediate vicinity of a given electron at point \mathbf{r} . The LDA is known as overbind, particularly in molecules. In order to the reason that in this studies we have neglected it in favor of the GGA. The GGA attempts to incorporate the effects of inhomogeneities³¹ by including the gradient of the electron density; as such it is a semi-local method. The GGA exchange-correlation functional can be written as:

$$E_{xc}^{GGA}[n(\mathbf{r})] = \int n(\mathbf{r})\bar{\varepsilon}_{xc}[n(\mathbf{r})]F_{xc}[n(\mathbf{r}), \nabla n(\mathbf{r})]d\mathbf{r} \quad (2.24)$$

where $F_{xc}[n(\mathbf{r}), \nabla n(\mathbf{r})]$ is known as the enhancement factor. Unlike the LDA, there has not unique form for the GGA, and indeed many possible variations are possible

³⁹⁻⁴¹, each corresponding to a different enhancement factor. The GGA succeeds in reducing the effects of LDA over binding, and is significantly more successful when applied to molecules, and also generally employed for semiconductor systems. For metallic systems GGA is also overall better than LDA for cohesive properties (lattice parameters, cohesive energies, elastic constants)^{42, 43}. Therefore, in this thesis, we employed the GGA-PBE exchange correlation functional⁴⁴ for entire calculation. But one may notice that neither LDA nor GGA are not perfect, they don't work for strongly correlated systems^{42, 45, 46} and also false to describe Van der Waals interactions, excited states, band gaps⁴⁷⁻⁴⁹.

2.5 Bloch's Theory

In solid state systems, the periodic potential appears because the ions are arranged with a periodicity of their Bravais lattice, given by lattice vectors \mathbf{R} . $V(\mathbf{r} + \mathbf{R}) = V(\mathbf{r})$ and $\psi(\mathbf{r} + \mathbf{R}) = \exp(i\mathbf{k} \cdot \mathbf{R})\psi(\mathbf{r})$. The physical meaning of \mathbf{k} is an indication for describes the wavefunction variation with space transition. If the \mathbf{k} is discrete (molecule) then the energy is also discrete energy level. If the \mathbf{k} is continuing (solid state) then it corresponds with energy band. For a system with translational symmetry $[H, T] = 0$, thus $\hat{H}\psi_{n,\mathbf{k}} = E_{n,\mathbf{k}}\psi_{n,\mathbf{k}}$, $T(\mathbf{R})\psi_{n,\mathbf{k}} = e^{i\mathbf{k} \cdot \mathbf{R}}\psi_{n,\mathbf{k}} \Rightarrow \psi_{n,\mathbf{k}} = e^{i\mathbf{k} \cdot \mathbf{r}}u_{n,\mathbf{k}}(\mathbf{r})$.

The momentum of electron can be calculated as the operation:

$$\mathbf{P}\psi_{nk} = \frac{\hbar}{i}\nabla\psi_{nk} = \frac{\hbar}{i}\nabla[e^{i\mathbf{k}\mathbf{r}}u_{nk}(\mathbf{r})] = \hbar\mathbf{k}\psi_{nk} + \frac{\hbar}{i}e^{i\mathbf{k}\mathbf{r}}\nabla u_{nk}(\mathbf{r}) \quad (2.5.1)$$

For bloch electrons, $\psi_{n,\mathbf{k}}$ is no longer a momentum eigenstate $\hat{\mathbf{P}}\psi_{n,\mathbf{k}} \neq \hbar\mathbf{k}\psi_{n,\mathbf{k}}$.

however, and $\hbar\mathbf{k}$ is called the crystal momentum and \mathbf{k} can always be confined in the first Brillouin zone (1st B.Z) with restricted vector $\{\mathbf{k}\} = \hbar\mathbf{a}^* + \mathbf{k}\mathbf{b}^* + \mathbf{l}\mathbf{c}^* \equiv \mathbf{G}$, Where

h, k, l are integers and the vectors $\mathbf{a}^*, \mathbf{b}^*, \mathbf{c}^*$ are the reciprocal lattice vectors. In terms of the lattice vectors the reciprocal lattice vectors $\mathbf{a}^*, \mathbf{b}^*, \mathbf{c}^*$ are given by:

$$\mathbf{a}^* = 2\pi \frac{\mathbf{b} \times \mathbf{c}}{\mathbf{a} \cdot (\mathbf{b} \times \mathbf{c})}, \quad \mathbf{b}^* = 2\pi \frac{\mathbf{c} \times \mathbf{a}}{\mathbf{a} \cdot (\mathbf{b} \times \mathbf{c})}, \quad \mathbf{c}^* = 2\pi \frac{\mathbf{a} \times \mathbf{b}}{\mathbf{a} \cdot (\mathbf{b} \times \mathbf{c})} \quad (2.5.2)$$

It can be reduced to be a hermitian eigenvalue problem which restricted to a single primitive cell of the crystal. The Hamilton of a periodic crystal system can rewrite:

$$\hat{H}_k = -\frac{\hbar^2}{2m} (\mathbf{i}\mathbf{k} + \nabla)^2 + V(\mathbf{r}) \quad \text{with} \quad \text{B.C} \psi_{n, \mathbf{k} + \mathbf{G}}(\mathbf{r}) = \psi_{n, \mathbf{k}}(\mathbf{r}), \quad \psi_{n\mathbf{k}} = \exp(\mathbf{i}\mathbf{k} \cdot \mathbf{r}) u_{n\mathbf{k}}(\mathbf{r})$$

However the partial differential equation is too complicated. But we can reduce the boundary value problem to a simple matrix diagonalization problem by using the variational principle. We can choose a set of orthonormal basis $\{\chi_n\}$ that also satisfy the same periodic boundary conditions.

$\chi_n(\mathbf{r} + \mathbf{R}) = \chi_n(\mathbf{r})$, and the wavefunction can expand as linear combination of $\{\chi_n\}$,

$u_k(\mathbf{r}) = \sum_n C_n \chi_n(\mathbf{r})$ Minimizing the expectation value $\langle u_k | \hat{H} | u_k \rangle$ with normalizes

constraint $\langle u_k | u_k \rangle$ for the ground state solution we have:

$$\frac{\partial}{\partial C_l^*} \left\langle \sum_n C_n \chi_n \left| H_k \right| \sum_m C_m \chi_m \right\rangle - \lambda \frac{\partial}{\partial C_l^*} \left\langle \sum_n C_n \chi_n \left| \sum_m C_m \chi_m \right\rangle = 0$$

$$\sum_m H_{lm}(\mathbf{k}) C_m - \lambda \sum_m S_{lm} C_m = 0 \quad (2.5.5)$$

According to orthogonal conditions the equation remains only the terms which satisfies $C_n = C_m$, thus:

$$\sum_m H_{lm}(\mathbf{k})C_m - \lambda \sum_m S_{lm}C_m = 0, \text{ where } H_{lm}(\mathbf{k}) = \langle \chi_l | H_k | \chi_m \rangle, S_{lm} = \langle \chi_l | \chi_m \rangle \quad (2.5.6)$$

Thus we can transform complicated boundary value problem to a diagonalization eigenvalue problem. By Apply the boundary condition of macroscopic periodicity for generalize volume commensurate with underlying Bravais lattice we have:

$\psi(\mathbf{r} + N_i \mathbf{a}_i) = \psi(\mathbf{r})$, $i = 1, 2, 3$, where \mathbf{a}_i are the primitive vectors and N_i are integers of order where $N = N_1, N_2, N_3$ is the total number of primitive cells in the crystal. The quantum number \mathbf{k} can be composed from the reciprocal lattice vectors

$\mathbf{k} = x_1 \mathbf{b}_1 + x_2 \mathbf{b}_2 + x_3 \mathbf{b}_3$, since $\mathbf{a}_i \cdot \mathbf{b}_j = 2\pi \delta_{ij}$ the Bloch theorem then gives $e^{i2\pi x_i N_i} = 1$.

Thus, $x_i = \frac{m_i}{N_i}$ and the allowed Bloch wave vectors are given by: $\mathbf{k} = \sum_{i=1}^3 \frac{m_i}{N_i} \mathbf{b}_i$ with

m_i integers. For a simple cubic Bravais lattice, the allowed wave vector components

reduce to the earlier $k_x = \frac{2\pi m_x}{L_x}, k_y = \frac{2\pi m_y}{L_y}, k_z = \frac{2\pi m_z}{L_z}$, since $N_i = \frac{L}{a}$ and

$\mathbf{b}_i = \frac{2\pi}{a} \hat{i}$ etc. As for a free electron case, the volume Δk per allowed k is given by

$\Delta \mathbf{k} = \frac{8\pi^3}{V}$. The group velocity of a Bloch electron given by n and \mathbf{k} is $\mathbf{v}_n(\mathbf{k}) = \frac{1}{\hbar} \frac{\partial \varepsilon_n}{\partial \mathbf{k}}$.

An external force acting on an electron in the crystal gives rise to change of \mathbf{k} , and the variation energy can be written as:

$$\frac{d\mathbf{k}}{dt} = \frac{\mathbf{F}}{\hbar}, \quad \delta \varepsilon = \mathbf{F} \cdot \mathbf{v}_g \delta t = \mathbf{F} \cdot \left(\frac{1}{\hbar} \frac{\partial \varepsilon}{\partial \mathbf{k}} \right) \delta t \quad (2.5.7)$$

The ground state of a system of Bloch electrons can be constructed by filling up energy levels just as in the free electron case. To count each level only once, \mathbf{k} needs to be limited to a single primitive cell of the reciprocal lattice, typically the first

Brillouin zone. The allowed \mathbf{k} values are still spaced discretely, even though $\varepsilon_n(\mathbf{k})$ are continuous functions of \mathbf{k} . Since the volume of the Brillouin zone is

$$D(\varepsilon) = \frac{V}{4\pi^3} \int \frac{dS_\varepsilon}{\bar{V}_k \varepsilon_{nk}}, \quad D(\varepsilon)d\varepsilon = \int_{\substack{\text{shell in k space} \\ \varepsilon < \varepsilon_{nk} < \varepsilon + \Delta\varepsilon}} \frac{d\mathbf{k}}{2\pi^3/V} = \frac{V}{8\pi^3} \int_{\varepsilon < \varepsilon_{nk} < \varepsilon + \Delta\varepsilon} \delta\mathbf{k} dS_\varepsilon \quad (2.5.8)$$

which gives $2N$ electron states per band. Depending on the number of valence electrons per cell V_c and the band structure $\varepsilon_n(\mathbf{k})$, one may obtain completely filled or partially filled bands. The Fermi surface is obtained from the condition that $\varepsilon_F = \varepsilon_n(\mathbf{k})$. If some bands are completely filled and all others remain empty, the gap between the highest occupied level and the lowest unoccupied level is known as band gap. Theoretically, the accurate band-structure energy of a system can be calculated

by integral over the filled parts of the bands:
$$\sum_n \frac{1}{\Omega_{BZ}} \int_{\Omega_{BZ}} \varepsilon_{nk} \delta(\varepsilon_{nk} - \mu) d\mathbf{k} \quad (2.5.9)$$

But due to finite computer resources this integral has to be evaluated using a discrete set of \mathbf{k} -points^{50, 51}: $\frac{1}{\Omega_{BZ}} \int_{\Omega_{BZ}} \rightarrow \sum_k \omega_k$, where ω_k is the weighting of the \mathbf{k} points.

Keeps the step function we get a sum of density of state: $\sum_n \sum_k \omega_k \varepsilon_{nk} \delta(\varepsilon_{nk} - \mu)$ But it converges exceedingly slow with the number of \mathbf{k} -points included. This slow convergence speed arises only from the fact that the occupancies jump from 1 to 0 at the Fermi-level. If a band is completely filled the integral can be calculated accurately using a low number of \mathbf{k} -points (semiconductors and insulators). Thus we can replace the step function $\delta(\varepsilon_{nk} - \mu)$ by a (smooth) function $f(\{\varepsilon_{nk}\})$ resulting in a much faster convergence speed without destroying the accuracy. The VASP program supports several selectable smearing methods⁵². In general, for semiconductors or

insulators we select always the tetrahedron method with Blöchl corrections⁵³, if the cell is too large (too few k-points) we select Gaussian smearing with appropriate smearing width (σ).The following sketch diagram shows how to integral DOS through the discrete k-points by different smearing method.

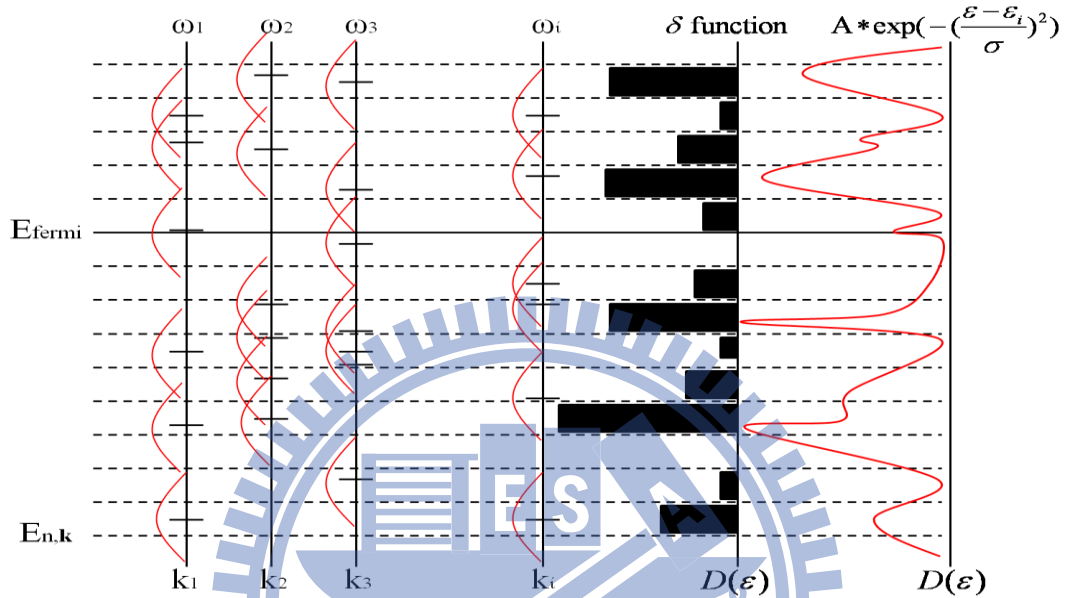


Figure 2.5.1 Sketch diagram of DOS smearing, the short solid line in left represents discrete eigenstates and the red curve represents its dispersion broadening. The spectrum on right side represents integral results through the different smearing method.

Chapter 3 Algorithm

3.1 Pseudopotential

Most of physical and chemical properties of materials depend only on the behaviors of valence electrons. The core electrons usually do not participate in the chemical bond. They are strongly localized around the nucleus; therefore, the distribution of core electrons basically does not change even if the atoms are placed in a different chemical environment. It is thus justified to assume the core electrons to be “frozen” and to keep the core electron distribution of the isolated atom in the crystal environment. The first advantage of the frozen-core approximation is that now fewer electrons have to be treated and less eigenstates of the Kohn–Sham equations have to be calculated. The second advantage is that the total energy scale is largely reduced. If the core electrons were removed from the workload which makes the calculations of energy differences between atomic configurations numerically much more stable. In principle one might just take the distribution of the core electrons and combine their Hartree potential with the Coulomb potential of the nucleus to an ionic core potential. However, this is not very useful since the valence wave functions still have to maintain their nodal structure in order to be orthogonal to the core states. Much more practical is to replace immediately the ionic core potential by a pseudo potential which leads to nodeless valence wave functions⁵⁴. Current pseudo potentials are constructed from ab initio calculations for isolated atoms. Assume we have solved

the Kohn–Sham equations for a single atom of the chemical species for which we would like to generate a pseudo potential. This can be done easily since due to the spherical symmetry of atoms the wave functions can be written as a product of a radial function and a spherical harmonic. The Schrödinger equation then reduces to one–dimensional differential equations for the radial functions which can be integrated numerically. A typical result for a radial function from such an “all–electron” atom calculation together with the corresponding external Coulomb potential as shown in Fig. 3.1.1. In general, the pseudopotential is also constructed such that the scattering properties of the pseudo wavefunctions are identical to the scattering properties of the ion and core electrons. This will be different for each angular momentum component of the valence wavefunction, therefore the pseudopotential will be angular momentum dependent. Pseudopotentials with angular momentum dependence were called non-local pseudopotentials. The usual methods of pseudopotential generation firstly determine the all electron eigenvalues of an atom using the Schrödinger equation

$$\left(-\frac{\hbar^2}{2m} \nabla^2 + V \right) \psi_{AE(l)} = c_{(l)} \psi_{AE(l)} \quad (3.1.1)$$

where $\psi_{AE(l)}$ is the wavefunction for the all electron (AE) atomic system with angular momentum component l . The resulting valence eigenvalues are substituted back into the Schrödinger equation but with a parameterized pseudo wavefunction function of the form⁵⁵: $\psi_{ps(l)} = \sum_{i=1}^n \alpha_i j_i$, where j_i are spherical Bessel functions. The coefficients, α_i , are the parameters fitted to the conditions listed below. In general the pseudo wavefunction is expanded in three or four spherical Bessel functions. The pseudopotential is then constructed by directly inverting the Kohn-Sham equation

with the pseudo wavefunction $\psi_{ps(i)}$. The pseudopotential is not unique, but they have to obey following criteria. First, Pseudo-electron eigenvalues must be the same as the valence eigenvalues obtained from the atomic wavefunctions. Second, Pseudo wavefunctions must be continuous at the core radius as well as its first and second derivative and also be non-oscillatory. Third, on inversion of the all electron Schrödinger equation for the atom, excited states may also be included in the calculation (if appropriate for a given condensed matter problem), for example, generating a d component for a non-local pseudopotential when the ground state of an atom does not contain these angular momentum components. 4. The core charge produced by the pseudo wavefunctions must be the same as that produced by the atomic wavefunctions. This ensures the pseudo atom produces the same scattering properties as the ionic core. To make the exchange-correlation energy accurately it is necessary that outside the core region⁵⁶ the real and pseudo wavefunctions be identical so that both wavefunctions generate identical charge densities (see conditions listed above). Generation of a pseudopotential that satisfies

$$\int_0^{R_c} \psi_{AE}^*(\mathbf{r})\psi_{AE}(\mathbf{r})d\mathbf{r} = \int_0^{R_c} \psi_{ps}^*(\mathbf{r})\psi_{ps}(\mathbf{r})d\mathbf{r} \quad (3.1.2)$$

The condition guarantees the equality of the all electron and pseudo wavefunctions outside the core region. In general this is achieved using a non-local pseudopotential which uses a different potential for each angular momentum component of the pseudopotential. This also best describes for the scattering properties from the ion core. This type is known as non-local norm-conserving pseudopotentials⁵⁷ and is the most transferable since they are capable of describing the scattering properties of an ion in a variety of atomic environments. There are several ways in which these

conditions can be satisfied leading to the non-uniqueness of pseudopotential. This can be traced back to the expansion of the wavefunction in terms of a plane wave basis set. The setting of plane waves, $\exp((\mathbf{k} + \mathbf{G}) \cdot \mathbf{r})$ forms a complete basis set and the additional core states to which they are orthogonal results in a linearly dependent spanning set, that is an over complete basis set. This linear dependence leads to non-unique pseudopotentials.

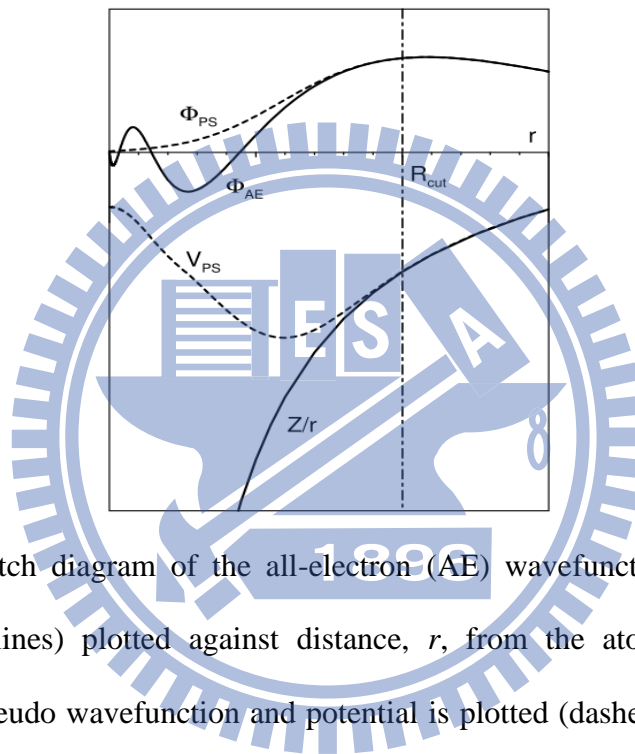


Figure 3.1.1 Sketch diagram of the all-electron (AE) wavefunction and electronic potential (solid lines) plotted against distance, r , from the atomic nucleus. The corresponding pseudo wavefunction and potential is plotted (dashed lines). Outside a given radius, R_{cut} , the all electron and pseudo electron values are identical.

3.2 Projector Augmented Wave (PAW)

The projector augmented wave (PAW) method⁵⁸ is an extension of augmented wave methods and the pseudopotential approach, which combines their traditions into a unified electronic structure method. At the root of the PAW method lays a transformation, which maps the true wave functions with their complete nodal structure onto auxiliary wave functions that are numerically convenient. We aim

for smooth auxiliary wave functions, which have a rapidly convergent plane wave expansion. With such a transformation we can expand the auxiliary wave functions into a convenient basis set, and evaluate all physical properties after reconstructing the related physical (true) wave functions. We denote the physical one-electron exact wave functions as $|\phi_n\rangle$ and the auxiliary wave functions as $|\tilde{\phi}_n\rangle$, where n is the label for a one-particle state and contains a band index, a k -point and a spin index.

They can transfer to each other through a transformation operator $|\phi_n\rangle = \hat{T}|\tilde{\phi}_n\rangle$.

The electronic ground state can be determined by minimizing a total energy functional $E[\phi_n]$ of the density functional theory. The one-particle wave functions have to be orthogonal. This constraint is implemented with the method of Lagrange multipliers.

$$F([\psi_n], \Lambda_{n,m}) = E[\phi_n] - \sum_{n,m} [\langle \phi_n | \phi_m \rangle - \delta_{n,m}] \Lambda_{n,m} \quad (3.2.1)$$

The extremum condition for the wave functions has the form: $H|\phi_n\rangle f_n = \sum_m |\phi_m\rangle \Lambda_{n,m}$

where the $\Lambda_{n,m}$ is the Lagrange multiplier and f_n are occupation numbers. To express the functional, F , in terms of our auxiliary wave functions, we have:

$$F([T\tilde{\phi}_n], \Lambda_{n,m}) = E[T\tilde{\phi}_n] - \sum_{n,m} [\langle \tilde{\phi}_n | T^\dagger T | \tilde{\phi}_m \rangle - \delta_{n,m}] \Lambda_{n,m} \quad (3.2.2)$$

The variational principle with respect to the auxiliary wave functions yields

$$T^\dagger H T |\tilde{\phi}_n\rangle = T^\dagger T |\tilde{\phi}_n\rangle \varepsilon_n \quad (3.2.3)$$

Again, we obtain a Schrödinger-like equation, but now the Hamilton operator has a different form, $T^\dagger H T$ an overlap operator $T^\dagger T$ occurs and the resulting auxiliary wave functions are smooth. If we want to evaluate physical quantities, we need to evaluate expectation values of an operator \hat{O} , which can be expressed in terms of either the true or the auxiliary wave functions:

$$\langle O \rangle = \sum_n f_n \langle \phi_n | \hat{O} | \phi_n \rangle = \sum_n f_n \langle \tilde{\phi}_n | T^\dagger \hat{O} T | \tilde{\phi}_n \rangle \quad (3.2.4)$$

In the representation of auxiliary wave functions we need to use transformed operators, $\hat{O} = T^\dagger \hat{O} T$. As it is, this equation only holds for the valence electrons. The transformation takes us conceptionally from the pseudopotentials to that of augmented wave methods, which deal with the full wave functions. The operator, T , has to modify the smooth auxiliary wave function in each atomic region, so that the resulting wave function has the correct nodal structure. Therefore, it makes sense to write the transformation as identity plus a sum of atomic contributions, $T = 1 + \sum_R S_R$. For each atom, S_R adds the difference between the true and the auxiliary wave function. The index R is a label for an atomic site. The local terms, S_R , are defined in terms of solutions $|\phi_c\rangle$ of the Schrödinger equation for the isolated atoms. This set of partial waves will serve as a basis set so that, near the nucleus, all relevant valence wave functions can be expressed as superposition of the partial waves with unknown coefficients:

$$\phi(\mathbf{r}) = \sum_{i \in R} c_i \phi_c(\mathbf{r}) \text{ for } |\mathbf{r} - \mathbf{R}_R| < |\mathbf{R}_{cut}| \quad (3.2.5)$$

The index i refers to a site index \mathbf{R} , the angular momentum indices (l, m) and an additional index that differentiates partial waves with same angular momentum quantum numbers on the same site. Since the core wave functions do not spread out into the neighbouring atoms. Currently we use the frozen-core approximation so that density and energy of the core electrons are identical to those of the corresponding isolated atoms. The transformation T shall produce only wave functions orthogonal to the core electrons, while the core electrons are treated separately. Therefore, the set of atomic partial waves $|\phi_c\rangle$ includes only valence states that are

orthogonal to the core wave functions of the atom. For each of the partial waves we choose an auxiliary partial wave $|\tilde{\phi}_c\rangle$ and let:

$$|\phi_c\rangle = (1 + S_R)|\tilde{\phi}_c\rangle, \quad S_R|\tilde{\phi}_c\rangle = |\phi_c\rangle - |\tilde{\phi}_c\rangle \quad (3.2.6)$$

In order to apply the transformation operator to an arbitrary auxiliary wave function, we have to expand the auxiliary wave function locally into the auxiliary partial waves:

$$\tilde{\phi}(\mathbf{r}) = \sum_{i \in R} \tilde{\phi}_c(\mathbf{r}) \langle \tilde{p}_i | \tilde{\phi} \rangle \quad \text{for } |\mathbf{r} - \mathbf{R}_R| < |\mathbf{R}_{cut}| \quad (3.2.7)$$

The projector functions probe the local character of the auxiliary wave function in the atomic region and satisfy orthogonality conditions

$$\sum_i |\phi_{c(i)}\rangle \langle \tilde{p}_i| = 1 \quad \text{and} \quad \langle \tilde{p}_i | \phi_{c(j)} \rangle = \delta_{i,j} \quad \text{for } i, j \in R. \quad (3.2.8)$$

Finally, the exact wave function can be expressed as:

$$|\phi\rangle = |\tilde{\phi}\rangle + \sum_{i \in R} (|\phi_c\rangle - |\tilde{\phi}_c\rangle) \langle \tilde{p}_i | \tilde{\phi} \rangle = |\tilde{\phi}\rangle + |\phi^1\rangle - |\tilde{\phi}^1\rangle \quad (3.2.9)$$

The following figure demonstrated how does PAW method worked in VASP.

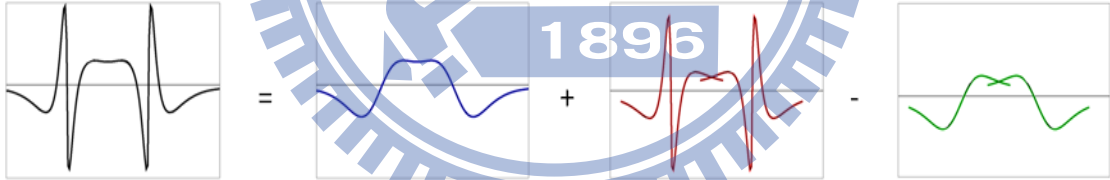


Figure 3.2.1 superposition sketch of PAW method

3.3 Residual Minimization Scheme

According to the Kohn-Sham equation, the charge density and energies of a system can be written as sum of ground state one electron wavefunction:

$$\rho^{tot}(\mathbf{r}) = 2 \sum_{n=1}^{N_e/2} |\phi_n(\mathbf{r})|^2 + \rho^{ion}(\mathbf{r}) \quad (3.3.1)$$

$$E^{tot} = \frac{\hbar^2}{2m} 2 \sum_{n=1}^{N_e/2} \int \phi_n^*(\mathbf{r}) \nabla^2 \phi_n(\mathbf{r}) d\mathbf{r} + \frac{1}{2} \frac{\rho^{tot}(\mathbf{r}) \rho^{tot}(\mathbf{r}')}{|\mathbf{r} - \mathbf{r}'|} d\mathbf{r} d\mathbf{r}' + E_{xc}[\rho(\mathbf{r})] \quad (3.3.2)$$

The VASP provides several algorithms to improve wavefunction for searching Kohn- Sham ground state. The most stable and efficiency method is the residual minimization scheme (RMS)^{59, 60}. One usually starts with a set of trial wavefunctions representing the filled states and a few empty one electron states, and then the wavefunctions are improved by adding to each certain amount of the residual vector:

$|R_n\rangle = (\hat{H} - \varepsilon_n \hat{S})|\phi_n\rangle$ and a wavefunction $|\phi'_n\rangle = |\phi_n\rangle + \lambda \hat{P}|R_n\rangle$, where \hat{P} is a preconditioner. For the short wavelength parts of the residuals, $\hat{H} - \varepsilon_n \hat{S}$ will be dominated by the kinetic energy operator, so we have approximately $\hat{P} \approx -\hat{T}^{-1}$

Then we can get step length λ by minimizing the norm of new residual vector

$$\langle R_n | R_n \rangle = \langle \phi_n | (\hat{H} - \varepsilon_n \hat{S})^\dagger (\hat{H} - \varepsilon_n \hat{S}) |\phi_n\rangle \quad (3.3.3)$$

, and possesses a quadratic unrestricted minimum at the each eigenfunction $\phi_n(\mathbf{r})$. If a good starting guess for the eigenfunction it is possible to use the algorithm without the knowledge of other wavefunctions, and therefore without explicit orthogonalization of the preconditioned residual vector.

3.4 Ab-initio molecular dynamics (AIMD)

A natural consequence of the Car-Parrinello formalism^{61, 62} is that electronic and ionic relaxation can take place simultaneously, the time-dependence of the electronic structure is a consequence of nuclear motion. For this to be performed, the total forces on the ions must be found to update the ionic positions. In order to process this part, Born-Oppenheimer Molecular Dynamics was employed in VASP program⁶³. The force on an ion, I , at position R_I can be obtained from the full derivative of the total

energy: $\mathbf{F}_I = -\frac{dE}{d\mathbf{R}_I}$ As the electronic wavefunctions change, force on the ions will be altered; therefore the full derivative has to be expressed in terms of changes in the wavefunction:

$$\mathbf{F}_I = -\frac{dE}{d\mathbf{R}_I} = \sum_i \frac{\partial E}{\partial \varphi_i} \frac{\partial \varphi_i}{\partial \mathbf{R}_I} - \sum_i \frac{\partial E}{\partial \varphi_i^*} \frac{\partial \varphi_i^*}{\partial \mathbf{R}_I}, \text{ where } E = \langle \varphi | H | \varphi \rangle \quad (3.4.1)$$

It follows that $\frac{\partial E}{\partial \varphi_i}$ is just $H \varphi_i$. But φ_i are electronic eigenstates with eigenvalues ε_i .

Therefore after some algebraic manipulation the last two terms can be written as:

$\sum_i \varepsilon_i \frac{\partial}{\partial \mathbf{R}_I} \langle \varphi_i | \varphi_i \rangle$. This shows that when each electronic orbital is an eigenstate of the Hamiltonian, then the partial derivative of the total energy with respect to the ionic positions is the force felt by the ions. According to the Hellmann-Feynman theorem⁶⁴, it can be generalized to any order of derivative of the total energy. In practice, the wavefunctions are only calculated to a given tolerance therefore they are not exact eigenstates of the Kohn-Sham Hamiltonian. As a result the forces calculated using the Hellmann-Feynman theorem incurs error. This can be seen when the expression for the force is written formally as:

$$\mathbf{F}_i = -\frac{\partial E_{ext}}{\partial \mathbf{R}_i} - \int n(\mathbf{r}) \frac{\partial V_I}{\partial \mathbf{R}_i} d\mathbf{r} - \int \frac{\partial E}{\partial n(\mathbf{r})} \frac{\partial n(\mathbf{r})}{\partial \mathbf{R}_i} d\mathbf{r} \quad (3.4.2)$$

where E_{ext} are all external energies such as the Ewald energy. The final term, called the variational force, vanishes when the wavefunctions are completely converged so that the conditions of the Hellmann-Feynman theorem are satisfied. It is in this term that the errors occurring from unconverged wavefunctions or incomplete basis sets are incurred. The error on the force is first order with respect to error in the wavefunction.

It follows that the Hellmann-Feynman theorem can only be implemented when the wave functions are very close to self consistency. Only then can the ionic equations of motion be integrated and the ionic positions updated. This leads to the use of the Born-Oppenheimer approximation. This is based on the fact that typical electronic velocities are much greater than that of the ions. It can therefore be assumed that the ions move so slowly relative to the electrons that at any point in time, the electrons will be in their ground state for that instantaneous ionic configuration (see Fig. 3.4.1). The ground state wavefunction is first calculated self-consistently for a fixed set of ionic coordinates. In this method an initial wavefunction has to be assumed this is given by initializing the expansion coefficients of the wavefunction by random numbers. Although this initial state is far from the Kohn-Sham eigenstates it does not assume any initial symmetry which, if incorrect, could lead to prohibitively long calculation to find the correct wavefunctions. The total energy is reduced by the residual minimization scheme (RMS) until the wavefunctions are sufficiently converged to give correct forces. New ionic positions are then calculated under the influence of these forces either by integration of the equations of motion or by direct minimization techniques. After each change in the position of the ions, the wavefunctions will no longer be eigenstates of the new ionic positions. In order to find the wavefunctions for this better set of ionic positions it is not necessary to randomize the wavefunctions. The motion of the ions will be sufficiently small that the old wavefunctions will be a good place to initialize the iterative procedure again. After electronic self-consistent iteration, a molecular dynamic iterative procedure as shown in Fig. 3.4.2. The verlet algorithm is employed for time iteration in VASP program which running as follow step. Consider expansion of coordinate forward and backward in time scale we have:

$$\begin{aligned} \mathbf{r}(t + \delta t) &= \mathbf{r}(t) + \frac{1}{m} \mathbf{p}(t) \delta t + \frac{1}{2m} \mathbf{F}(t) \delta t^2 + \frac{1}{3!} \frac{d^3 \mathbf{r}}{dt^3} \delta t^3 + \dots \\ \mathbf{r}(t - \delta t) &= \mathbf{r}(t) - \frac{1}{m} \mathbf{p}(t) \delta t + \frac{1}{2m} \mathbf{F}(t) \delta t^2 - \frac{1}{3!} \frac{d^3 \mathbf{r}}{dt^3} \delta t^3 + \dots \end{aligned} \quad (3.4.5)$$

Adding above two formulas:

$$\mathbf{r}(t + \delta t) = 2\mathbf{r}(t) - \mathbf{r}(t - \delta t) + \frac{1}{m} \mathbf{F}(t) \delta t^2 + \dots \quad (3.4.6)$$

As the equation shows, we only need to know current acceleration from the potential

gradient of current position: $\mathbf{a}(t) = \frac{\mathbf{F}(t)}{m} = \frac{-\nabla U[\mathbf{r}(t)]}{m}$. Finally we can obtain velocity

information from the finite difference method: $\mathbf{v}(t) = \frac{\mathbf{r}(t + \delta t) - \mathbf{r}(t - \delta t)}{2\delta t}$. A

schematic view of iterative procedure as shown in Fig. 3.4.2.

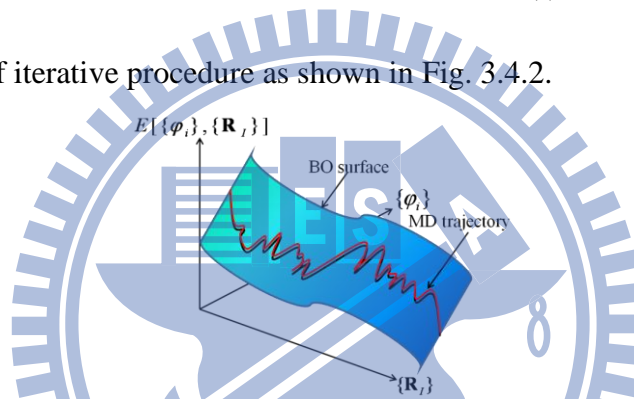
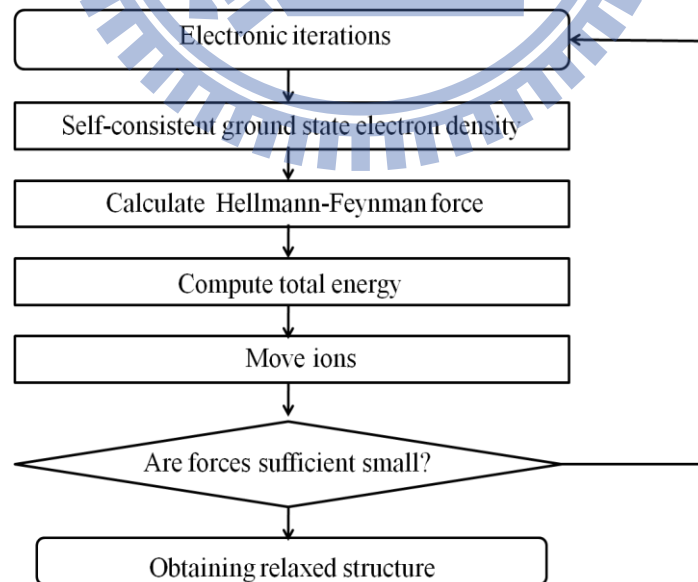


Figure 3.4.1 Schematic diagram of an MD trajectory on BO surface



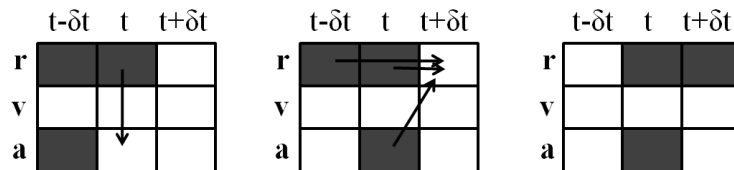


Figure 3.4.2 Flow chart of iterative procedure of *ab initio* molecular dynamics simulations (AIMD).

Chapter 4 Experimental results

In chapter we will first introduce the principle of scanning tunnel microscope (STM) and X-ray photoelectron spectroscopic (XPS); and then, discuss experimental results. Two measurement experiments have same sample preparation procedure as shown in following. The sample was placed in a grounded μ -metal chamber with ultrahigh-vacuum (UHV) environment ($1\sim 3\times 10^{-10}$ torr) at room temperature (~ 300 K). The Si(100) samples used in our experiment were sliced into pieces of size 1 mm \times 8 mm .After loading the samples to the chamber; the samples were then being degassed for over 12 hours at ~ 900 K. After degassing, the sample was flashed at ~ 1450 K for a few seconds (~ 9 s) to remove the surface oxide layer. After these processes the surface would form a Si(100)- 2×1 dimerized surface. More detailed sample cleaning procedure please refer this article⁶⁵. And then, chlorine gas was induced and controlled through a leak valve. The amount of dosage of chlorine gas was about $2\times 10^{-8}\times 2$ minutes (2.4 Langmuir) .After reaction; the surface would form a Cl-terminated Si (100)- 2×1 structure. After that, we employed the DC current controlled “alkali metal disperser” to deposit Sodium atom under varying exposure time. The deposition rate was calibrated by thickness monitor; and to converter the unit into “ML” by referring atom density of surface silicon. About one minute afterwards, the surface would reach thermal equilibrium. After that time, we just start

to take data.

4.1 Principle of STM

The STM technique has been widely used in various fields, like condensed-matter physics, chemical, biology physics etc. Especially, after resolving the structure of the Si(111)-7×7 in real space using STM⁶⁶⁻⁶⁸, this instrument has proven to be an extremely powerful tool. Fig. 4.1.1 exhibits its essential component. A probe tip, usually made of tungsten (W) or Pt-Ir alloy^{69, 70}, is attached to a piezoelectric scanner. Using the positioner, the tip and sample are brought to be within a few angstroms. A bias voltage, applied between the tip and the sample, causes an electrical current to flow. A quantum-mechanical phenomenon, tunneling, is the principle theory of the scanning tunneling microscopy. For achieving higher atomic resolution, vibration isolation is essential. A commonly used vibration isolation system consists of a set of suspension springs and a damping mechanism. Based on quantum tunneling theory, an electron can penetrate into or across a potential barrier even if its energy E is smaller than the potential Φ within the barrier (see Fig. 4.1.2). For a rectangular barrier we have:

$$\psi(d) = \psi(0)e^{-\kappa d}, \text{ where } \kappa = \frac{\sqrt{2m(\Phi - E)}}{\hbar} \quad (4.1.1)$$

The probability of finding an electron behind the barrier of the width d is

$$W(d) = |\psi(d)|^2 = |\psi(0)|^2 e^{-2\kappa d} \quad (4.1.2)$$

In a STM system a small bias voltage V is applied so that the tunneling of electrons results in a tunneling current I . The barrier height can be roughly estimated by the

$$\text{average workfunction of sample and tip } \Phi = \frac{(\Phi_{\text{sample}} + \Phi_{\text{tip}})}{2}$$

If the applied voltage is much smaller than the workfunction ($eV \ll \Phi$), the κ can be

simplified as a constant: $\kappa \approx \frac{\sqrt{2m\Phi}}{\hbar}$, and the current is proportional to the probability

$$\text{of tunneling electrons penetrate the barrier: } I \propto \sum_{E=E_f-eV}^{E_f} |\psi(0)|^2 e^{-2\kappa d}. \quad (4.1.3)$$

The tunneling current depends on an integration of electron density of states around the Fermi level. Therefore, STM image is a mapping of surface electron state instead of the atomic topography. Sometimes, we have to combine with theoretical computation to verify what the real structure is. Fig. 4.1.3 shows the direction of tunneling current under varying bias voltage. In general the fill state image is rather reliable than empty state images. But sometimes, we have to switch bias for clarifying real atomic image.

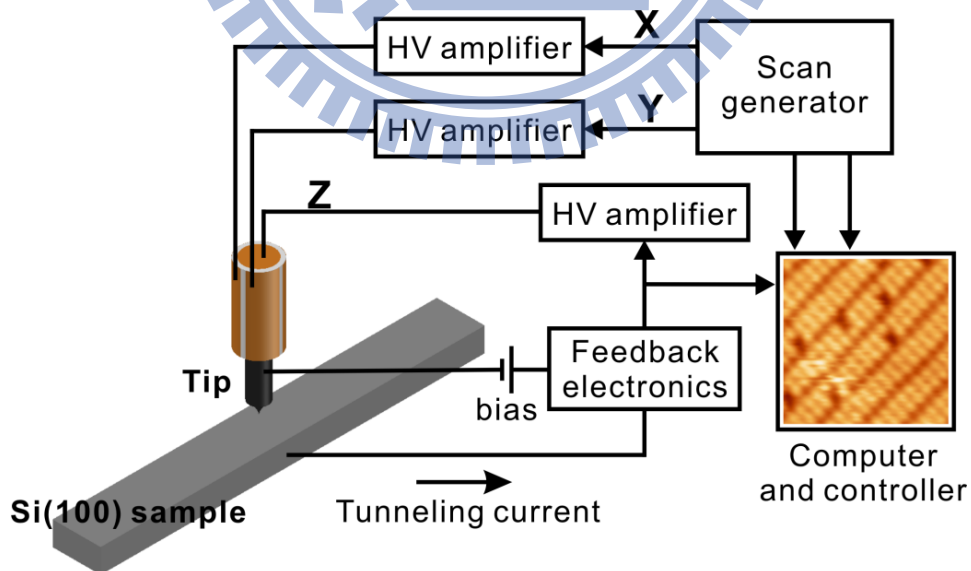


Figure 4.1.1 Schematic diagram of the essential elements of STM.

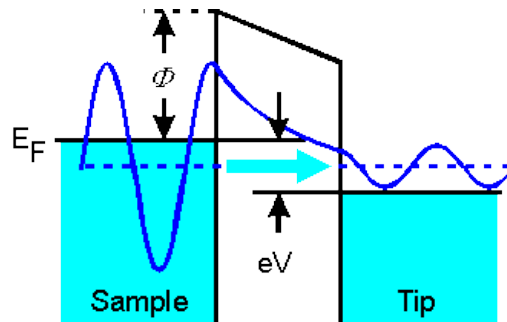


Figure 4.1.2 Schematic diagram of quantum tunneling phenomenon

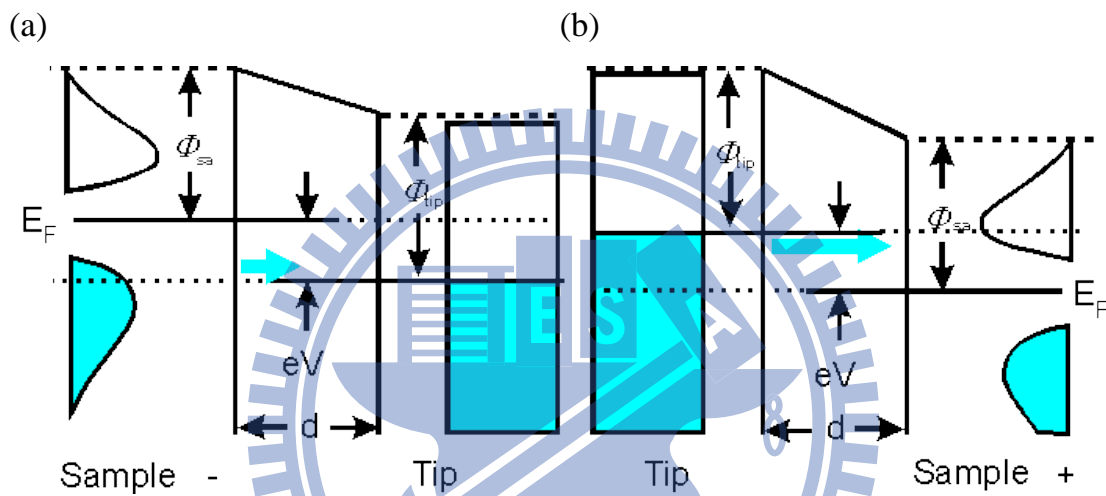


Figure 4.1.3 Schematic diagrams of tunneling current under varying bias voltage in filled state (a) the current tunneling from sample to tip; in empty state (b) the current tunneling from tip to sample.

4.2 STM results

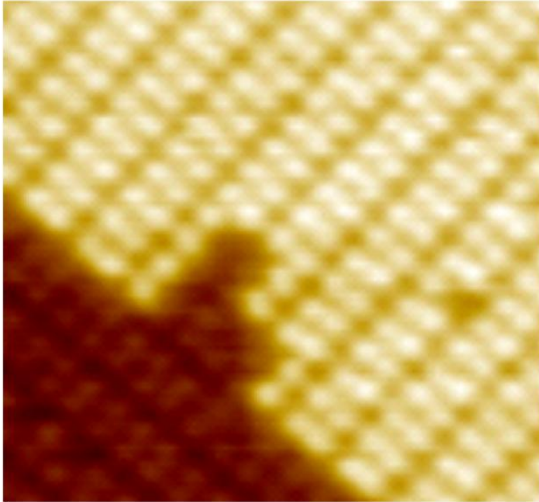
As shown in Fig. 4.2.1 (a), the chlorine-terminated $p(2 \times 1)$ surface had prepared before sodium deposition. A visible step edge located at lower left corner which separate the surface into two planes with different height ($\sim 1.36 \text{ \AA}$). Fig. 4.2.1 (b) shows the surface after 0.2 ML sodium deposition; the surface formed into three kinds of different pattern- a single dark dim (ii), a $p(2 \times 2)$ zigzag array (iii), and a chunk of dark dim (iv). Besides the type (iv) structure, every dark dot is located alternative one

side of dimer. Intuitively, we might consider that the sodium atom is directly standing on the top site of chlorine atom. However, if this is the case, it may induce strong surface electric dipole along z-direction, as we mentioned in sec. 1.1.3, that would cause the system unstable. On the other hand, the model cannot explain why the sodium should be arranged in zigzag pattern. If we assume that the pattern is due to somehow “stress force”; but how to explain the type (iv) structure? Up to now, depends only on the STM experiment cannot give a reasonable explanation; Fuller discussion will be presented in the next chapter. As shown in the Fig. 4.2.1(c), with the increasing of sodium coverage, the surface generated more and more dark dots; and they seem tending to form in more ordered p(2x2) structure. The residual uncovered dimer can serve as an indicator for identifying the surface orientation; which indicates the p(2x2) pattern prefer to extend along the dimer row. The average height difference along O-B in Fig. 4.2.1(c) is about one angstrom, and width of each peak is about $22/3 \sim 7.3 \text{ \AA}$.

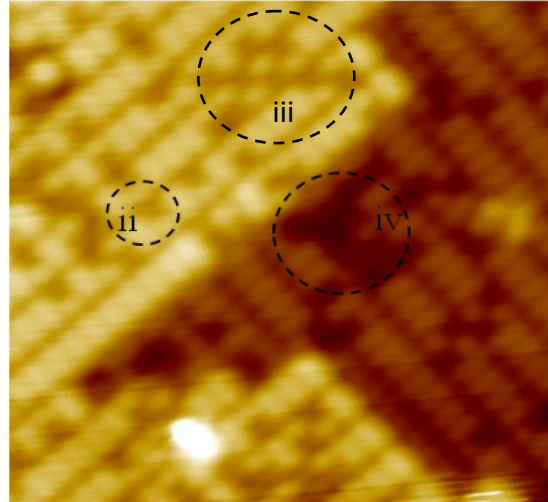
When the sodium coverage reached 0.75 ML, the image has rather different. As shown in the Fig. 4.2.1(d), most zigzag dark spot has disappeared and several darker cluster growing. But the average apparent height difference between O to point A still held one angstrom. Finally, the surface structure has significant structure transition when the sodium dosage reached one monolayer. The Fig. 4.2.1(e) reveals a clearly structural phase transition, incredibly, a large scale and uniform p(1x1) structure has been formed. The Fig. 4.2.1(f) shows an obvious height difference across the point O to point C approximately about 1.4 \AA that exactly correspond to the step gap of Silicon (1.36 \AA). But unlike the general step edge, that the structure is extended to very broad region ($\sim 30 \text{ \AA}$). The curve O-C indicates that the distance between two

wave peak is about $\frac{120}{28} \approx 4.3 \text{ \AA}$; is very closed to the simulated result (4.33 \AA). By comparing, in the case, either chlorine or sodium atom should correspond to the bright spot. Oppositely, darker spot should correspond to space that without any atom. That structure is exactly consisted with NaCl(100) structure; but the nearest distance in the thin film (4.33 \AA) is somewhat larger than that in typical NaCl crystal (4.00 \AA). Namely, the lattice is stretched about 8% in 2D thin film. More noteworthy is that the p(1x1) structure looks like a large carpet with many random corrugations; this feature is rather similar to the graphene. It tells us the 2D NaCl thin film may not be perfect plane. Corrugations would effectually reduce the surface stress which makes 2D structure can be stable. In summary, STM image strongly tells us that the surface morphology strongly depends on sodium coverage. It implies the growth mechanism of the case may involve somewhat structure phase transition. Besides, these images from STM measurement verify that 2D ionic NaCl layer indeed can be stable even at room temperature condition. It also confirmed that the self-limit concept can effectively enhance the lateral growth ratio. As far as we know, perfect 2D ionic NaCl is first time to be produced and observed in room temperature.

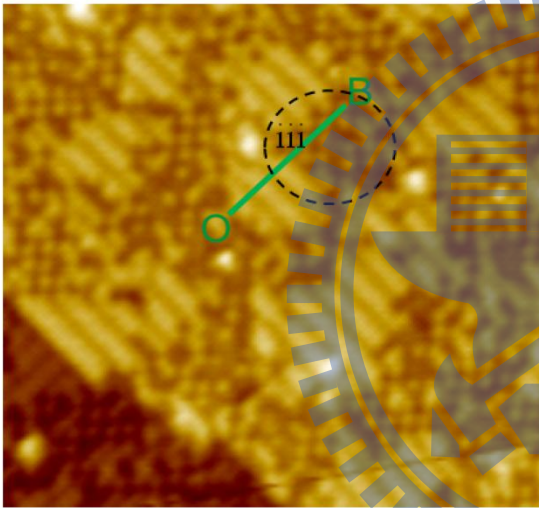
(a)



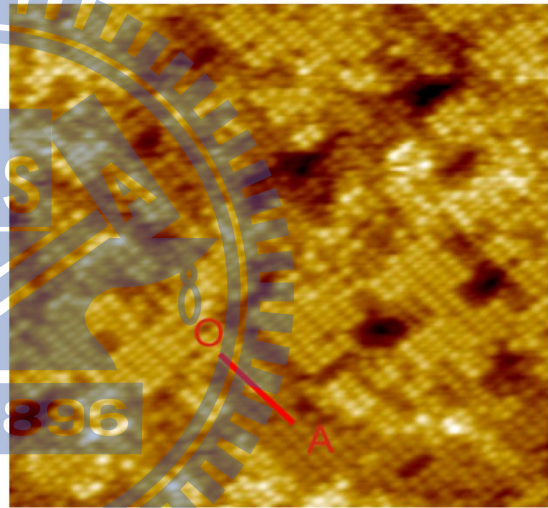
(b)



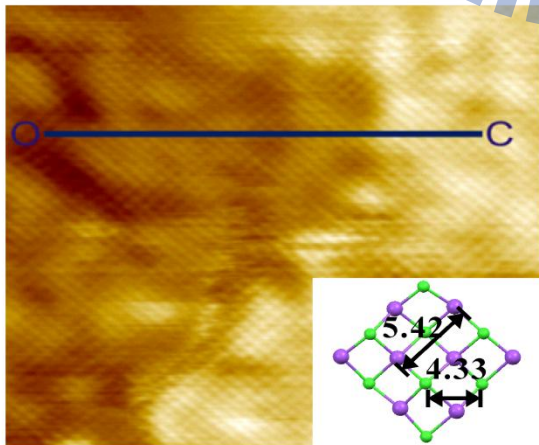
(c)



(d)



(e)



(f)

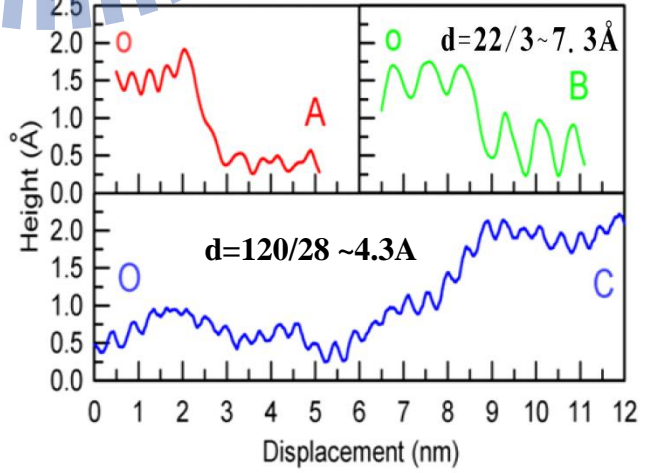


Figure 4.2.1 A series of STM images which scanned by the following parameters:

- (a) Chlorine-terminated p(2x1) Silicon surface scanned by sample bias $V_s=+2V$ (empty state) with $25A \times 25A$ scan size.
- (b) 0.2 ML sodium covered surface scanned by sample bias $V_s=-2 V$ (fill state) with $40A \times 40A$ scan size.
- (c) 0.5 ML sodium covered surface scanned by sample bias $V_s=-2 V$ (fill state) with $150 \times 150A$ scan size.
- (d) 0.7 ML sodium covered surface scanned by sample bias $V_s=+2 V$ (empty state) with $200A \times 200A$ scan size.
- (e) 1 ML sodium covered surface scanned by sample bias $V_s=-2V$ (fill state) with $150A \times 150A$ scan size; and a sketch of NaCl(100) thin film (calculated by VASP).
- (f) Measured apparent height topography along specific path in (c), (d) and (e).

4.3 Principle of XPS

X-ray photoelectron spectroscopy (XPS) is also an important one of surface analysis tools which take different approaches from core state of electron. The core level photoemission experiment is to collect the photoelectrons excited from core level near nucleus. Photoelectrons were collected and analyzed by a large hemispherical analyzer as shown in Fig. 4.3.1. Relative core level shift (RCLS) of an atom reflects its local bonding state and surrounding chemical environment. According to Einstein's principle of photoelectric effect we can write down the energy relation:

$$KE = h\nu - E_b - W$$

KE : kinetic energy of excited photoelectron

$h\nu$: incident photon energy

E_b : binding energy

W : work function.

The E_b is defined as the energy difference between the core states and Fermi level and W is the energy difference between the vacuum and Fermi level. This formula is based on the ideal conditions; however, we sometime have to consider other factors such as secondary electrons, imperfect inelastic scattering, band bending effect... etc. Experimentally, we have to using some data processing methods to eliminate those effects, such as background deduction, bulk alignment, least square fitting ...etc. Total resolution of instrument is convolution of x-ray source width, natural line width of peak, analyzer resolution⁷¹.

$$FWHM_{total} = \sqrt{FWHM_{x-ray}^2 + FWHM_{line-width}^2 + FWHM_{analyser}^2}$$

$(0.1 \sim 1.0 \text{ eV}) \quad (< 0.1 \text{ eV}) \quad (0.1 \sim 0.2 \text{ eV})$

(5.3.1)

Where FWHM of analyzer is really only one factor we can control. Resolution defines ability to separate closely spaced photoemission peaks $E = \frac{\Delta E}{E}$, $\Delta E \approx FWHM_{total}$, where E is the kinetic energy of photoelectron. Therefore we ought to select appropriate light source energy as small as possible. Synchrotron radiation has tunable energy range, higher collimation, lower aperture which provides a perfect light source for implementing XPS measurement.

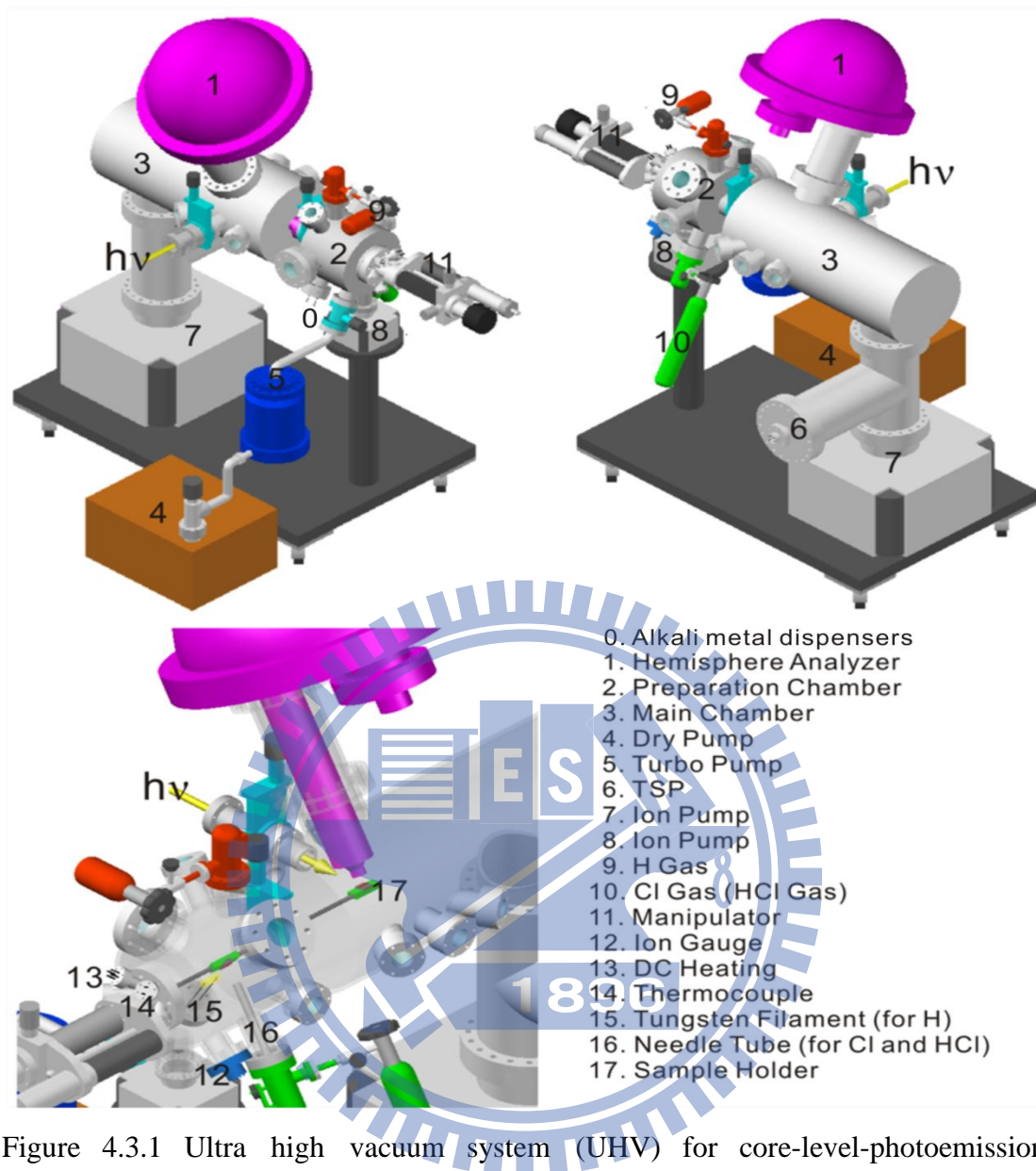


Figure 4.3.1 Ultra high vacuum system (UHV) for core-level-photoemission spectroscopy.

4.4 XPS results

The incident photon energies in our experiment is locked in 140 eV for Si $2p_{3/2}$ ($E_b=99.4$ eV), Na $2p_{3/2}$ ($E_b=30.8$ eV), and 240 eV for Cl $2p_{3/2}$ ($E_b=200$ eV) respectively. The relative energy resolution can be roughly estimated as follow:

$$\frac{\Delta E}{E} = \frac{\sqrt{(0.3)^2 + (0.1)^2 + (0.125)^2}}{E_{\text{photon}} - E_b} \sim 8.0 \times 10^{-3} (\text{Si}2p) \cdot 3.0 \times 10^{-3} (\text{Na}2p) \cdot 8.5 \times 10^{-3} (\text{Cl}2p).$$

The detailed XPS measured results are shown in Fig. 4.4.1 to Fig. 4.4.3. The background of each spectra has deducted by the standard Shirley method⁷², and each peak components were decomposed by least square fitting method with reasonable Gaussian and Lorentz mixed FWHM^{73, 74}. All energy scales are referred to the bulk Si $2p_{3/2}$ to eliminate band bending effect⁷⁵. A clean Si(100) spectra can be decomposed into four components. They are related to bulk (B) atoms, up atoms (S_u), down atoms (S_d), and the second layer (S') atoms respectively. After the chlorine reaction, two surface peaks (S_u · S_d) would disappear but S^+ became larger. This peak has narrower FWHM which corresponds to high ordered Si-Cl bonding state. With the increasing of sodium coverage, the FWHM of S^+ peak becomes more broadening. On the other hand, the intensity of dangling bond state (S_u · S_d) slowly increased until the sodium coverage over one monolayer. The result implies that the Si-Cl bonding has gradually weaken and becoming disorderly. At the time, deposited sodium plays the role of electron donor instead of surface silicon. In general, the surface dangling bond state has very high activity that can easily react with surrounding atoms. The dangling bond (DB) state usually cannot survive over ten minute even in the UHV chamber (5×10^{-10} torr). However, in the experiment, we found that the buried DB state in the interface that unexpectedly survived over more than one hour. We think the unusual

phenomenon is credited from cover layer, the dense NaCl thin film.

Next we discuss the spectra of Na $2p$ and Cl $2p$. Before the sodium deposition, FWHM of Cl $2p$ spectra looks very narrow that reflects the chlorine atom be in ordered Cl-Si bonded state. With the increasing of sodium dosage, the Cl $2p$ peak is shifting to higher binding energy, and its FWHM becomes broad. The sodium peaks also reveal same tendency. Their binding energy energies synchronously increased about 1.1 eV . Both the Na $2p$ and Cl $2p$ peak becomes more and more broad, which reveals that may not only unique one bond state existing at the surface or interface. It also indicates NaCl thin film may not be a perfect 2D plane. The behavior of synchronously core level shifts in Na and Cl should not be explained as a result of relative chemical shifts (charge transfer) between them. That should be regard as a result of total band offset, which reflects their valence bonding energy becoming stronger. The shift usually accompanies some constructional or ligancy changes. Now we don't have enough information for understanding how it happening, this issue will be fully discussed further in the last chapter. In additional, after the sodium dosage over one monolayer, a new peak was arising at the position of lower binding energy (-67.8 eV). It is corresponded the Na atoms who own higher electron density or fewer unscreened core hole. The peak should be explained as some metallic sodium clusters. The peak provides us a good indicator to double check the amount of sodium coverage. But, it is not necessary for the purpose of this thesis to inter into a detailed discussion of the extra metallic sodium.

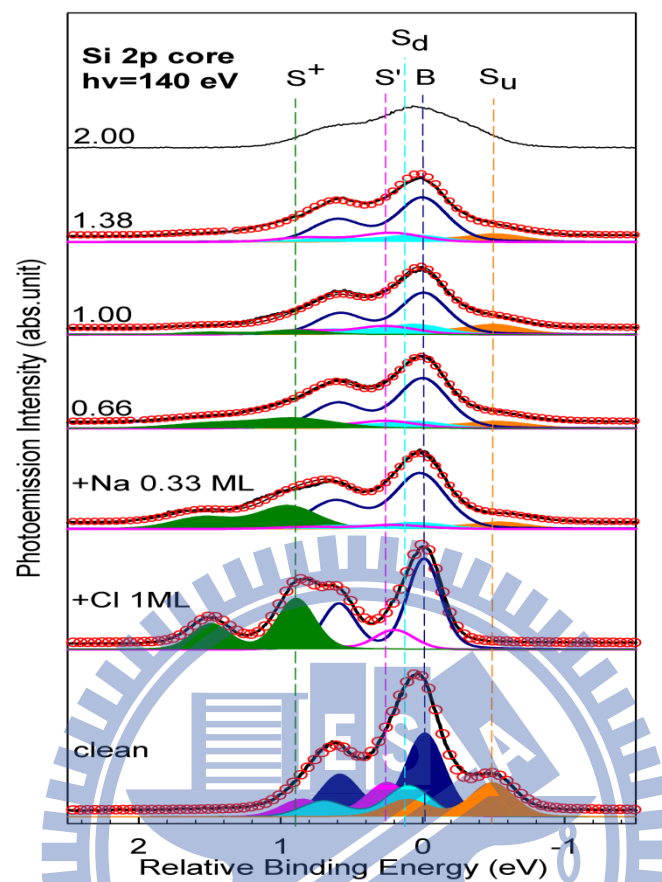


Figure 4.4.1 Si $2p$ core level photoemission spectra (red circles) for the ALD growth process. The black solid curves are the fitting results which can be decompose into five components - S_u (up atom) , S_d (down atom) , B(bulk) , S_i' (second layer) and S_i^+ (Si-Cl bonding state).

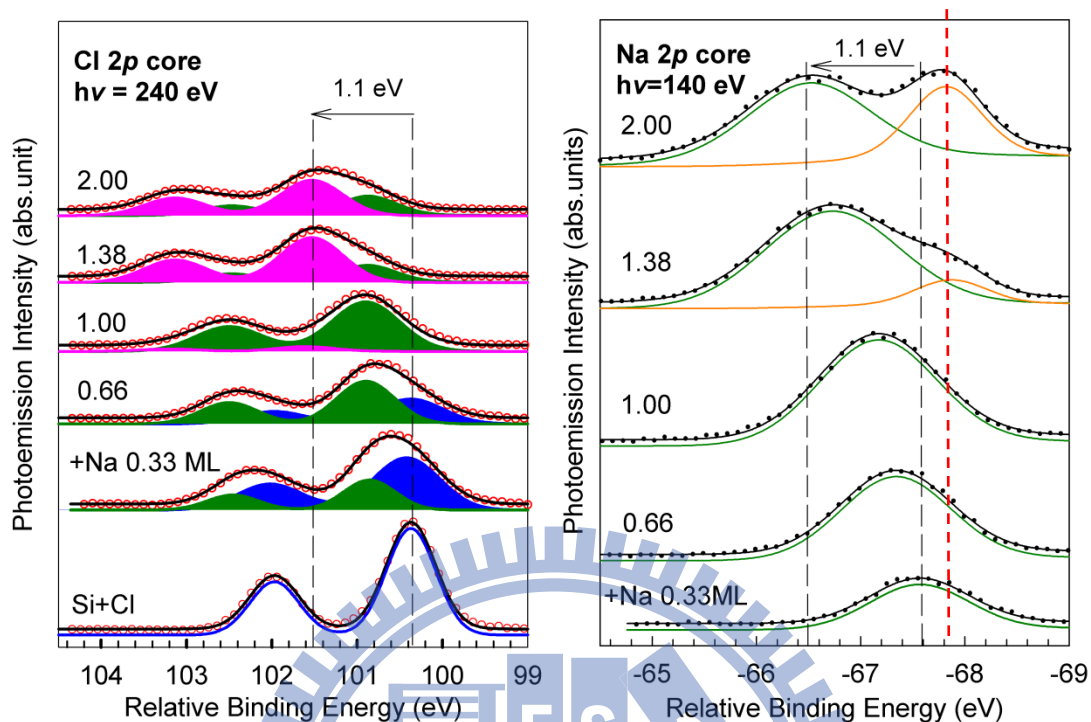


Figure 4.4.2 Cl $2p$ (left) and Na $2p$ (right) core level photoemission spectra (red and black dots) in different sodium coverage. Relative binding energy in both spectra were simultaneously shifted about 1.1 eV. When Na coverage is over 1 ML, a metallic Na $2p$ state appears at -67.8 eV.

Chapter 5 Computational results (I)

Morphologies and dynamics

In this chapter, we consider the cases in static calculations to find their ground state configurations (0K). In order to deepen the understanding the diffusion behavior of sodium atoms, we then employed the Nudged Elastic Band (NEB) method to compute diffusion barriers in various path ways. Sometimes, static relaxation is incapable for finding real global energy minimum, especially if the system is too complicated. Therefore, we attempted to use the alternative Abinito molecular dynamic simulation (AIMD) for seeking whether one structure has lower energy minimum. It not only guarantees structure's correctness but also provides more dynamic information. Detailed calculation conditions is listed in Appendix A.

5.1 Static structure relaxations

It is known that the top layer atoms of the Si(100) surface reconstruct to form parallel rows of dimers, which establish two well-differentiated directions, in parallel and perpendicular to these rows. After chlorine reaction, the chlorine atom tends to saturate at the top of dangling bond sites. We can calculate the adsorption energies for a chlorine molecule by the formula:

$$E_{ads} = (E_{Cl-Si-Cl} - E_{Si} - NE_{Cl_2}) / N \quad (5.1.1)$$

We get $E_{ads} = -3.44$ eV for single chlorine adsorption which value is roughly in a good agreement with that reported in previous papers. The reaction is a typical exothermic process with zero reaction barriers. If we increase the exposure of the chlorine gas, the density of the fully Cl-terminated dimers increases. Finally, all the dimers with

dangling bonds on the surface will be terminated with chlorine atoms. The adsorption of Cl molecules does not disrupt the dimer bonds, but break the weaker π bonds. Therefore, each dimer has terminated with two Cl atoms, as one Cl per Si, in the Cl-saturated Si(100)-p(2 \times 1) surface. Now, we consider one simplest adsorption situation to place one single sodium atom upon the surface. As shown in Fig 5.1.1(a), there are six high symmetric points should be concern. The consideration is based on translation symmetry and mirror symmetry, So sodium atom is individually placed one angstroms above the points for a static structure. By using the similar formula as Eq. 5.1.1,

$$\bar{E}_{ads} = (E_{Si-Cl-Na} - E_{Si-Cl} - NE_{iso-Na}) / N_{Na} \quad 5.1.2$$

We obtained mean adsorption energy with varying sodium number as shown in Fig. 5.1.1(b). As anticipated, for single sodium atom, the top site of chlorine is the most unstable position for adsorption. Contrast, hollow site is the most stable adsorption site. The Si-Cl bond length in each case was slightly to be elongated that is roughly inversely proportional to their adsorption energy. In contrast, Na-Cl bond has larger difference, larger Na-Cl bond would cause more stable structures, and shorter Na-Cl bond (T) would cause higher energy. If so, a square-like pattern with dark or bright spot is to be observed in experiment. However, it is not. We did not find any structure looks like a sodium atom on hollow site. Thus we go on to consider more complex structure the surface composed by plural sodium atom. As Fig. 5.1.1(b) shows, two sodium adsorb on adjacent hollow site would lead energy rising. With four sodium adsorption, the mean adsorption energy is equal to the mean value of separate case but unequal to the value of two sodium adsorption.

$$(-2.12(H_1H_2H_1H_2)) \approx (-2.15(H_1) + (-2.19)(H_2))/2 \neq -1.96(H_1H_2).$$

At first sight the result seems to be confusing. But if we more in-depth examine their structure we will find they are not similar. The Figures. 4.1.1(d) and (e) tell us if one chlorine be pulling out of the silicon is beneficial for reducing energy. the Si-Cl bond is broken and the Na-Cl ionic bond is formed. However, the energy is not lowered; the result still cannot explain why the dark spot in STM image always occupied only one side of dimer. For more in deep understanding what we observed in experiment, we have to further consider the diffusion behavior of the system. We will further discuss diffusion behavior of the sodium in next section.

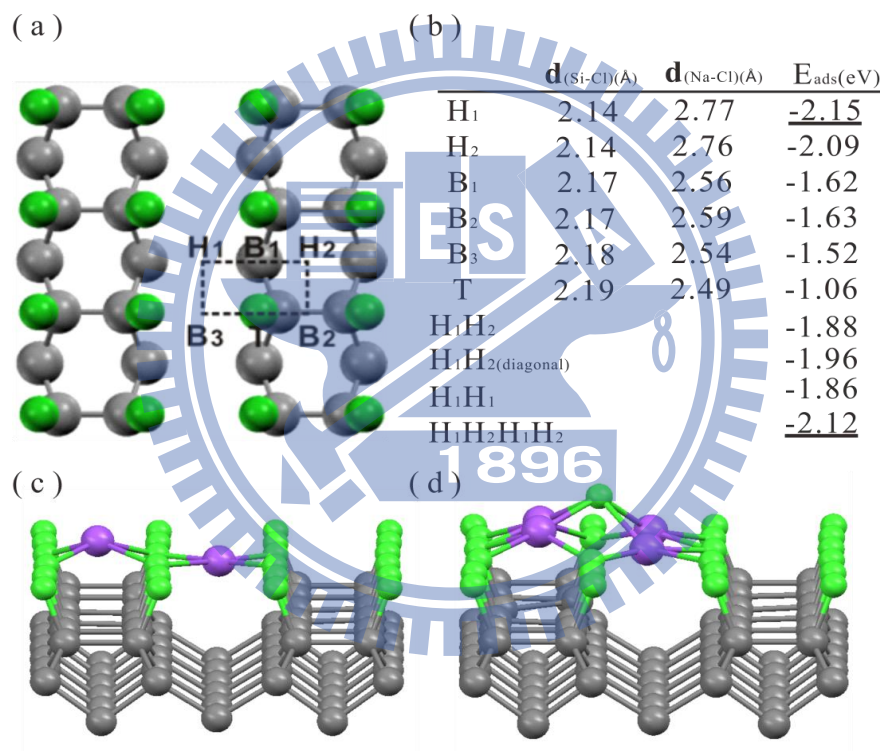


Figure 5.1.1(a) Bird's eye view of chlorine terminated Si(100) surface with six high symmetry adsorption sites,(b) mean adsorption energy table, (c) configuration of H₁H₂ case ,and (d) configuration of H₁H₂H₂H₂ case.

5.2 Diffusion process

The nudged elastic band (NEB)⁷⁶⁻⁸⁰ is a method for finding saddle points and minimum energy paths between known reactants and products. The method works by optimizing a number of intermediate images along the reaction path. Each image finds the lowest energy possible while maintaining equal spacing to neighboring images. This constrained optimization is done by adding spring forces along the band between images and by projecting out the component of the force due to the potential perpendicular to the band. The Fig. 5.2.1 conceptually illustrated how NEB works.

We now consider diffusion behavior for a single sodium atom. The Fig. 5.2.2 shows diffusion barrier along the path A→B→C→D. The diffusion barrier are 0.44 eV, 0.53 eV, and 0.57 eV for the path A→B, B→C, C→D respectively. In general, the atom can diffuse easily if the barrier is below 1 eV; namely, experimentally, that the pattern with single sodium on hollow site might exist only in lower sodium coverage. In higher sodium coverage, if they arrange to be a cluster which can effectively reduce energy, we cannot find single sodium atom but a cluster. That is the reason why we never observed in experiment the case a single atom on hollow site. We further consider the diffusion frequency by the Arrhenius formula:

$$D = D_0 \exp(-E_b / KT) \quad 5.2.1$$

Where E_b is the diffusion barrier, D_0 is the pre-factor. Although we have not been calculated this factor, but we assume the factor is the same in each case, and then, the diffusion ratio could be roughly estimated from:

$$R_{B \rightarrow C / A \rightarrow B} = \frac{D_0 \exp(-E_{B \rightarrow C} / KT)}{D_0 \exp(-E_{A \rightarrow B} / KT)} \approx \exp((E_{A \rightarrow B} - E_{B \rightarrow C}) / KT) \quad 5.2.2$$

After calculation, we got diffusion ratio 1, 0.30, and 0.18 for A→B, B→C, and C→D respectively. The result indicates that a sodium atom diffusing on dimer is relatively easy than others. The result is qualitatively explained why zigzag pattern along the

dimer is so frequently be observed in experiment. So far, we have discussed the possible adsorption behavior of the case in low sodium coverage. But for higher coverage, static calculation will no longer to be an efficient method for searching global energy minimum. Next section, we use alternative approach to determine ground state structure for the cases with higher sodium coverage.

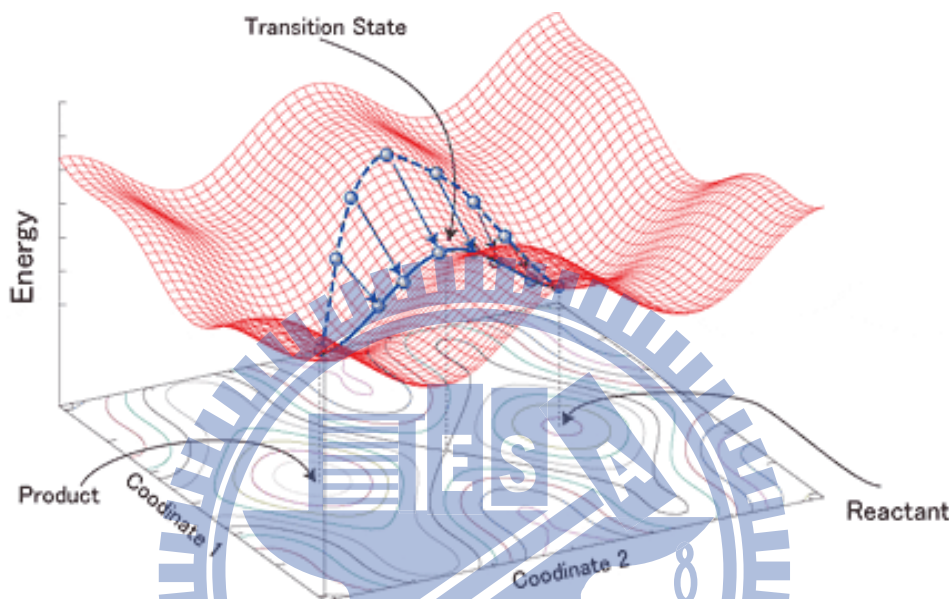


Figure 5.2.1 Sketch of the Nudged Elastic Band (NEB) method, to determine the energetic minimum path between the reactant and product state of a chemical reaction, an initial band (dashed) is constructed connecting the positional configuration of the two states. The location of the band is then minimized through a series of iterations yielding a minimum embedding of the band on the potential energy surface (solid line). (cited from <http://www.cybernet.co.jp/quantumwise/example/neb/neb-01.html>)

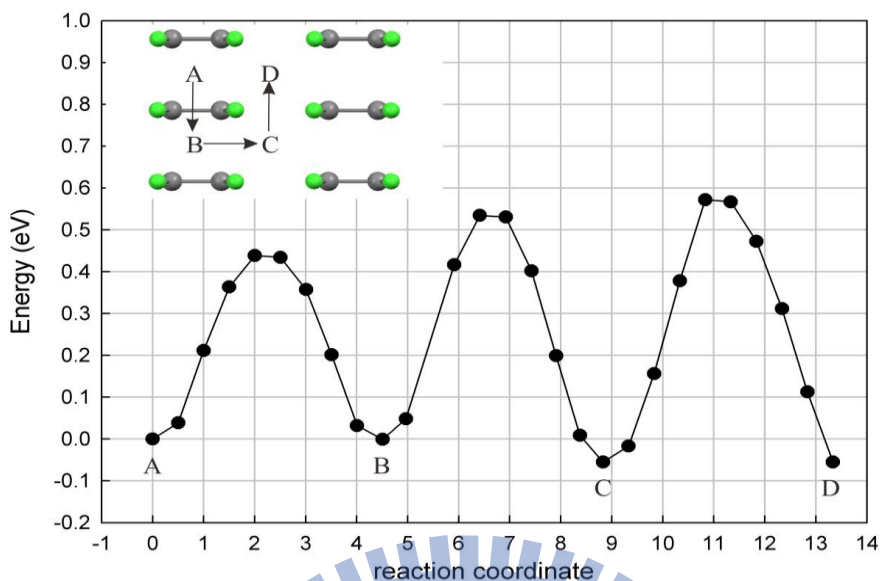


Figure 5.2.2 Energy variation along the diffusion path A→B→C→D, each the path contains eight intermediate states (black circle).

5.3 Finite temperature simulations

Molecular dynamics simulations generate information at the microscopic level, including atomic positions and velocities. Based on statistical mechanics, here we employed the canonical ensemble with several constraints for simulating “annealing process”. Here, we briefly introduce the principle of AIMD⁸¹⁻⁸⁴. In canonical ensemble, The particle number (N) and volumes (V) are keep constant, and a finite temperature were given by the heat bath approach – the Nose-Hoover thermostat⁸⁵⁻⁸⁷; which introduced a new degree of freedom’s’ as a reservoir, and then associate kinetic and potential energy can be redefined as following:

$$\begin{aligned}
U_s &= -gk_b T \ln s, \quad K_s = \frac{1}{2} Q \dot{s}^2 \\
L_{Nose} &= \sum_1^N \frac{m_i (s \dot{\mathbf{r}}_i)^2}{2} - U(\mathbf{r}^N) + K_s - U_s \quad \Rightarrow \quad \mathbf{p}_i = \frac{\partial L}{\partial \dot{\mathbf{r}}_i} = m_i s^2 \dot{\mathbf{r}}_i, \quad p_s = \frac{\partial L}{\partial \dot{s}} = Q \dot{s} \\
H_{Nose} &= \sum_1^N \frac{\mathbf{p}_i^2}{2m_i s^2} + U(\mathbf{r}^N) + K_s + U_s
\end{aligned} \tag{4.3.1}$$

where g is a new degree of freedom Q is effective mass. The can be interpreted as a time scaling factor ,which makes the system's total energy without to be conserved, but extended Hamiltonian is conserved. Therefore, we rewrite associated equations of motion as following:

$$\begin{aligned}
\dot{\mathbf{r}}_i &= \frac{\partial H}{\partial \mathbf{p}_i} = \frac{\mathbf{p}_i}{m_i s^2} \\
\dot{\mathbf{p}}_i &= -\frac{\partial H}{\partial \mathbf{r}_i} = \mathbf{F}_i \\
\dot{s} &= \frac{\partial H}{\partial p_s} = \frac{p_s}{Q} \\
\dot{p}_s &= -\frac{\partial H}{\partial s} = \frac{1}{s} \left[\sum_1^N \frac{\mathbf{p}_i^2}{m_i s^2} - gk_b T \right] \quad \frac{\partial (sp_s / Q)}{\partial t} = \frac{1}{Q} \left[\sum_1^N \frac{\mathbf{p}_i^2}{m_i s^2} - gk_b T \right]
\end{aligned} \tag{4.3.2}$$

With substituting $\zeta \equiv \frac{\dot{s}}{s}$, $\dot{\zeta} \equiv \frac{1}{Q} \left[\sum_{i=1}^N \frac{p_i^2}{m_i} - gk_b T \right]$, finally the Lagrangian equation of motion can be rewrite as:

$$\dot{\mathbf{r}} = \frac{\mathbf{p}_i}{m_i}, \quad \dot{\mathbf{p}}_i = \mathbf{F}_i - \zeta \mathbf{p}_i \tag{4.3.3}$$

The Nose' effective mass Q determines the response of the heat bath to fluctuations of the system. It should be sufficiently small to allow the system to approach to equilibrium fleetly. In the other hand, it should be large enough to yield correct values for the energy fluctuations of the system. The frequencies of temperature fluctuation are approximately the same as typical phonon-frequencies. The characteristic frequency of the thermostat is $\omega_T^2 = \frac{2gk_b T}{Q}$. Setting that to the same order of magnitude as the characteristic frequencies of system is always reliably

suggestion^{88, 89}. In addition, the time step should be small enough to follow the real trajectory, but too small setting would waste too much computing time. According to VASP guide line, how to select δt which is depends on what the component the system contains. For example, we use always $\delta t \sim 1\text{fs}$ for the first, $\delta t \sim 2\text{fs}$ for the second, $\delta t \sim 3\text{fs}$ or 4fs for the fourth rows of elements respectively. For our system (Si · Cl · Na), we always choose $\delta t \sim 2\text{fs}$ for all case. In general, the time chemical equilibrium required is only about picoseconds order. Here we set total simulation time $t=2000\text{fs}$ for all cases. The initial structure for MD calculation was given by the the results of static relaxation, and initial velocities of each atom were given by the Maxwell–Boltzmann distribution $\mathbf{v}_{x,y,z} = \pm \sqrt{\frac{KT}{M}} \approx 5 \times 10^{-2} \text{ \AA /fs}$ (300K).

Now, we first consider a simplest situation an initial adsorption process; six sodium atoms were arranged above the surface with random position. The initial velocity of each the sodium were given along $-z$ direction $(0, 0, \sim -5 \times 10^{-2}) \text{ \AA /fs}$. A series of images of dynamic process were shown in Fig. 5.3.1.(a)-(f). After 400 fs, we can clearly see that the left three sodium atoms has individually settled at the hollow site, and the right three sodium slowly close to each other. After 800 fs, one of right chlorine atom has been lifted by surrounding sodium atom. Until the end, the surface almost keeps the same configuration itself. The Fig. 5.3.1(g) reveals when the system after 500 fs, the temperature fluctuation has less than 50 K, which means, at the time, the system has achieved thermal equilibrium. Finally, the right sodium formed as a triangular structure and left sodium adsorbed on the hollow site individually. The result indicates that triangular cluster might be smallest unit of “NaCl” cluster.

Furthermore, we putted five sodium atoms in the adjacent hollow site as a initial

condition. As shown in Fig. 5.3.2(a)-(g), after 500 fs the system has achieved thermal equilibrium ($\delta T < 50$ K). At the same time, catercornered chlorine atoms have been lifted by surrounding sodium atoms. Sodium atom occupied a lower position instead of former chlorine atoms, and formed two triangular structures. Until the end, the surface atoms almost held their position with very small oscillation. The result strongly supports an explanation that the previous dark dot of zigzag p(2x2) pattern in STM experiment should be triangular structure instead of standing sodium atoms. Each the cluster contains three sodium atom and one chlorine atom that might block the tunneling current; therefore, the region seems darker than others. Later I shall try to give a more precise account of this issue. The results of higher sodium coverage case (9/36) were shown in Figure 5.3.3(a)-(g). At 400 fs, one of topmost sodium atom was assembled with three chlorine atoms, and each chlorine atom was assembled with lower three sodium atoms. Until the end, the structure has not changed much. Finally, the surface formed as several interlocking triangular fragments. In this case, we found a strange and beautiful pyramidal Na/Cl/Na/Si multi-layer structure. Let's further consider more complex case the surface with 13/36 sodium coverage. Fig. 5.3.4(a)-(f) shows the sodium and chlorine atoms still tend to form as triangular fragments. At 1600 fs, the upper right chlorine seems to be pulled out of its former position and move to the left side. Finally, the surface became very complex, from the top to down; the triangular NaCl cluster, Na cluster, and a few bare silicon dangling bonds.

Now, we summarized the MD results and list them in Fig. 5.3.5. There are five configurations calculated from static relaxation after MD calculation. We give a symbol to each structure (I-V). The mean adsorption energy of them can be calculated

$$\bar{E}_{ads} = (E_{Si+Cl+(N)Na} - E_{Si+Cl} - E_{isoNa}) / N \quad (5.3.4)$$

As shown in Fig. 5.3.5(a), with the increasing of sodium coverage, the mean adsorption energy becomes more and more high, which means, in the AIMD may no longer to be an effectively method for searching global energy minimum for the case(IV) and (V). Fig. 5.3.5(a) indicates type III has larger (lower) normalized adsorption energy that is most possible to be observed in experiment. Besides, there are two structure (type II, type IV) who have second highest normalized adsorption energy, they might also could be existing under the room temperature ($E_k = 0.025eV$). That also means in low sodium coverage case, the NaCl tend to form discrete triangular structure “on plane” instead of three-dimensional stack. By a comparing, the type II、III、IV exactly correspond to the type ii、iii、iv in STM images respectively (see Fig. 4.2.1(b) and (c)); which strongly supported our calculation results.

Let's further to examine the triangular structure. The bottom-right picture of Fig. 5.3.5 shows a typical NaCl crystal with both the (100) and (111) surface. By comparing, we can see that the triangle-like structure and NaCl(111) surface have the same phase. In the other words, the p(2x2) ordered structure is actually formed by discrete NaCl(111) cluster. However, the Na and Cl in NaCl(111) phase is formed as layer by layer. That surface would produce very strong surface dipole, as the results we presented in section 1.1.3; the surface would not to be stable. In addition, in the structure V, we can see an interesting structure at right medium side. It seems to be NaCl(111) structure; But if we look it on lateral, it could be also oblique NaCl(100). As we calculated before, The structure V is relatively unstable; we can image that the structure would transfer to NaCl(100) by two ways. First, the rhombus structure can pull out itself to form NaCl(100) surface; if so, the interface would remain much unoccupied silicon dangling bond. It should correspond to reappearing

S_u and S_d peak (see Fig. 4.4.1) that we observed in XPS experiment. Second, with more sodium coverage, sodium would freely diffuse from the edge or drop from the source to replace former sodium atom, and then, the NaCl(100) surface could also be formed. If so, a part of sodium atoms would be buried under the NaCl(100) layer. In order to gain lower energy, buried sodium should assemble itself as hexagonal (or discrete triangular) sodium layer. It should correspond to the metallic-like $Na2p$ peak. In summary, silicon dangling bond state and metallic-like $Na2p$ signal in XPS experiment both demonstrated that, in room temperature, two kinds of scenario could happen. Since the NaCl(111) phase should be the most stable structure. In order to more in detail understand how the (111) phase transfer to (100) phase when the sodium coverage is reached (over) 1 ML. We back to using the static relaxation; we reproduce the triangular structure along both on dimer and perpendicular to the dimer with varying numbers; after relaxation, we combine the energy calculation results to Fig. 5.3.5 and Fig. 5.3.6. The diagram indicates that if triangular NaCl cluster is growing along on dimer (VI-VIII); The mean adsorption energy have just only a little variation. But if that is growing along the direction perpendicular to the dimer, the structure would be unstable; which indicates here a repulsive interaction between the dimer rows. It means the triangular structure that along the direction perpendicular to the dimer cannot conserve with too large scale. That might be another reason why we always saw the $p(2 \times 2)$ pattern along dimer instead of perpendicular to the dimer.

In experiment, we observed apparent phase transition from $p(2 \times 2)$ to $p(1 \times 1)$ when sodium coverage over 1 ML. But in theory, simulating such structure changes is very difficult in implementation. Because, as shown in Fig. 4.2.1, although such structure in the x - y direction is roughly ordered, but in z direction is not. To completely describe such complicated structure required very large unit cell and

computational resource. We think that the DFT based on periodic boundary condition can not to handle such complicated process. Solving these kinds of problem usually requires from quantum Monte Carlo method. Here we just do a simple case, we artificially create a perfect planar $p(1 \times 1)$ NaCl thin film and put it on the Si(100) surface, and take it to do a standard MD simulation. After annealing, take the structure to do a static relaxation. As shown in Fig. 5.3.5, the type XII structure roughly hold its $p(1 \times 1)$ periodicity in the x-y direction, but it is not smooth in z-direction. The nearest distance between two chlorine atoms in this case is about 4.3 Å; the value almost equal to experiment result (see 4.2.1(e)). But the energy of this case is still higher than type XI about 0.03 eV/per sodium. However, as we can see in Fig. 5.3.6, the adsorption energy is reducing with lateral cluster density.

If the a NaCl(111) chain growing along with the direction perpendicular to dimer row side by side that would result in 0.05 eV energy ascending. In general, the average kinetic energy of an atom at room temperature is about $\frac{3}{2} kT \sim 0.025$ eV. By comparing of these numbers, judging from the above, we have good grounds for thinking, with the increasing of sodium coverage, the cluster would be forced in growing along perpendicular to dimer row; that would cause energy ascending and result in structure transition. With different sodium coverage, the process should be random and contiguous. It roughly corresponds to $p(1 \times 1)$ distorted structure that observed in STM experiment. This argument seems roughly to fit the facts. In the other hand, the continuous structure phase transition would reflect in continuous changes of valence bond state. As we shall see later in the next chapter, it would also lead core state shifts.

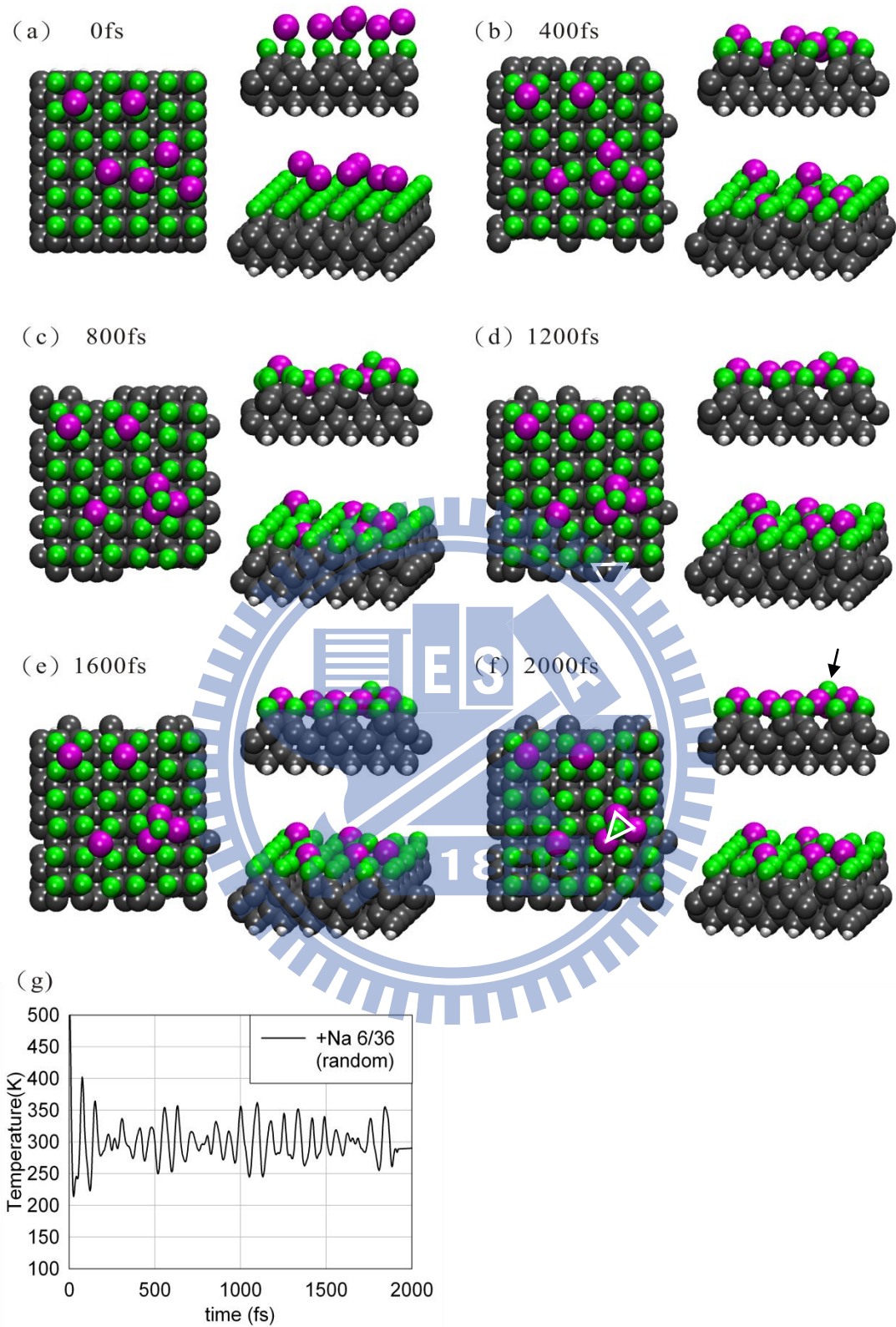


Figure 5.3.1(a)-(f) Molecular dynamic process: $\theta_{Na} = 6/36$ (random), and (g) temperature history. Each snapshot includes three kinds direction of view, the bird's eye view(left),side view(upper right),and oblique view(lower right)

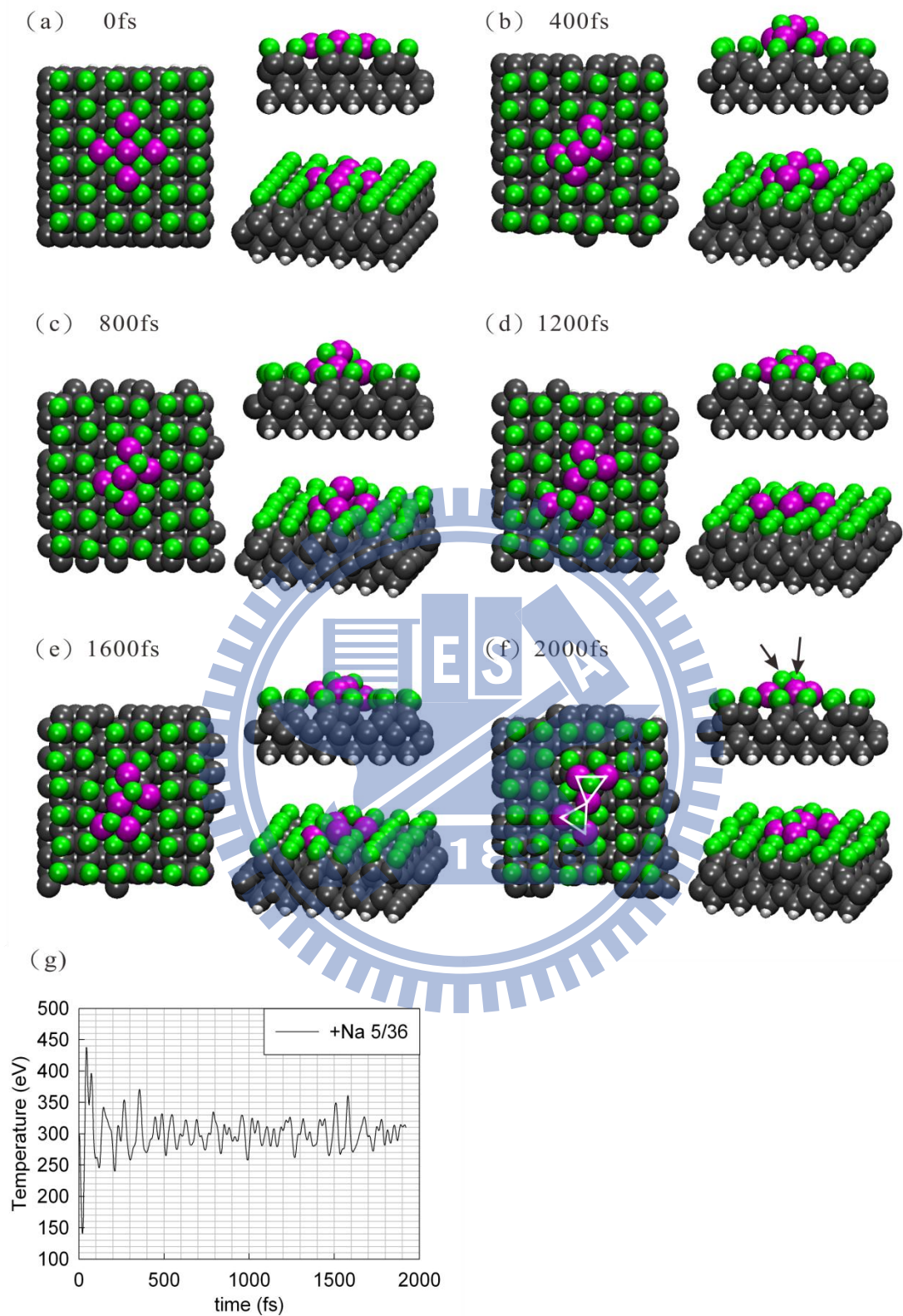


Figure 5.3.2(a)-(f) Molecular dynamic process: $\theta_{Na}=5/36$ and (g) temperature history.

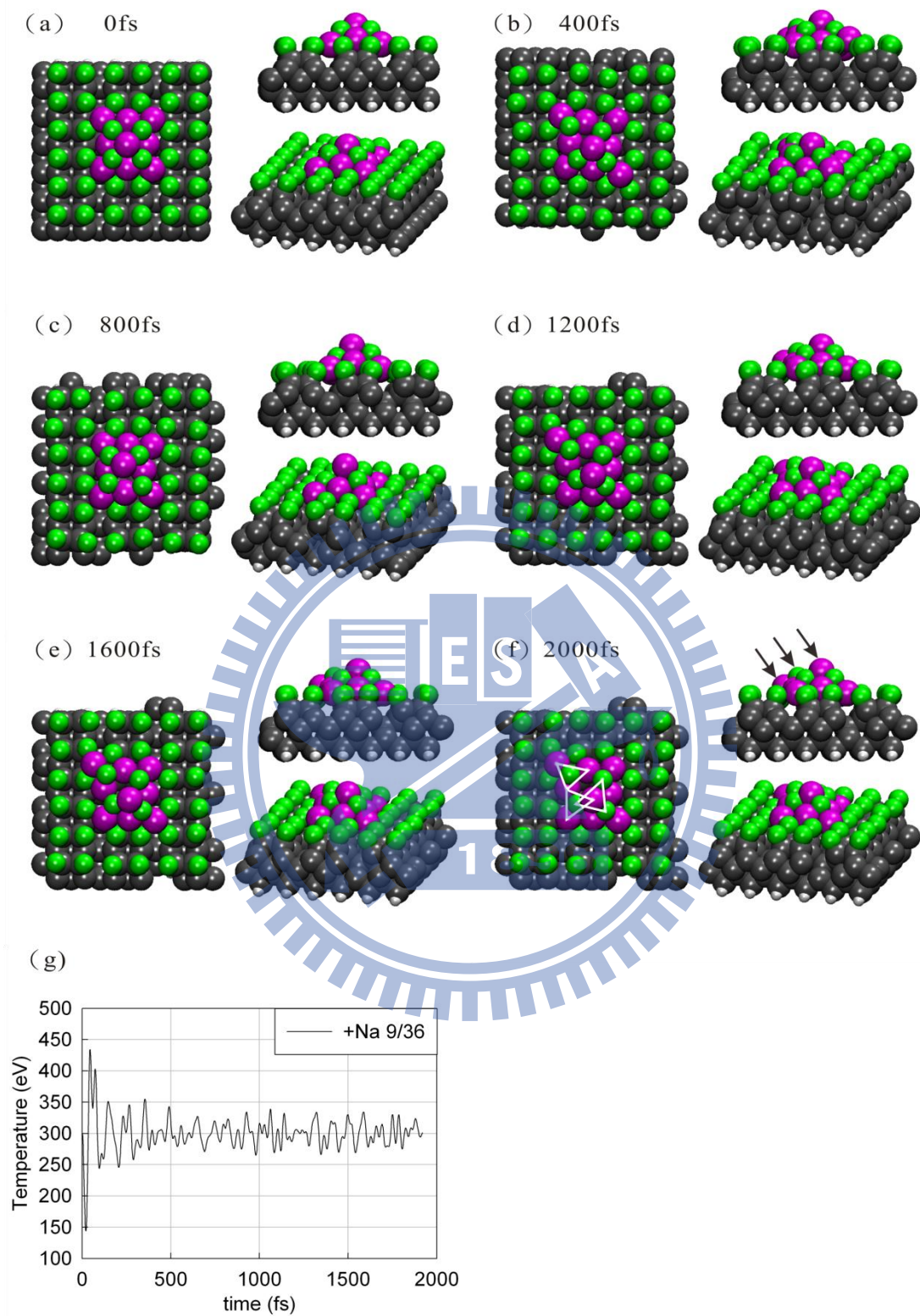


Figure 5.3.3(a)-(f) Molecular dynamic process: $\theta_{Na} = 9/36$ and (g) temperature history.

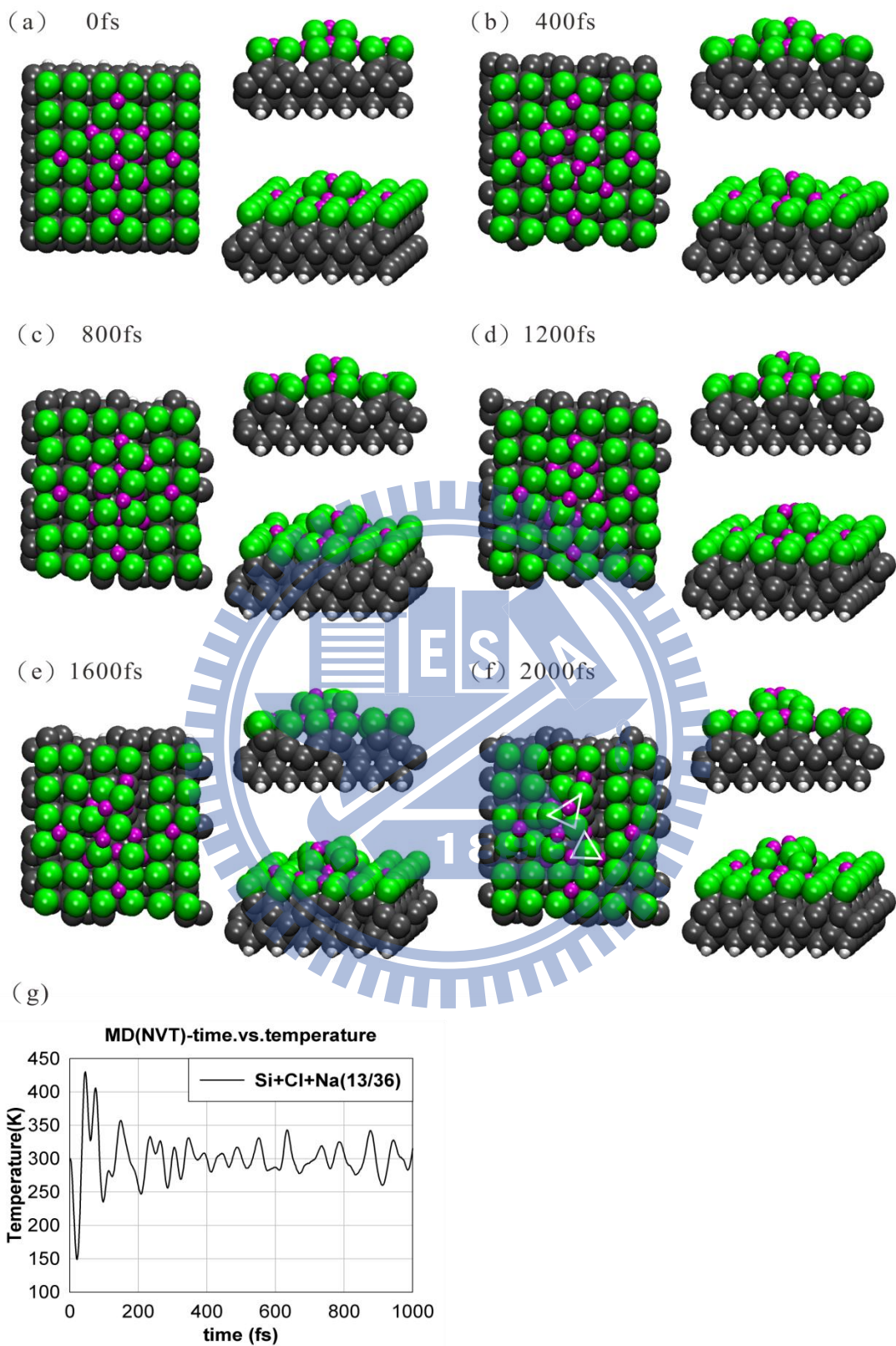


Figure 5.3.4(a)-(f) Molecular dynamic process: $\theta_{Na} = 13/36$ and (g) temperature history.

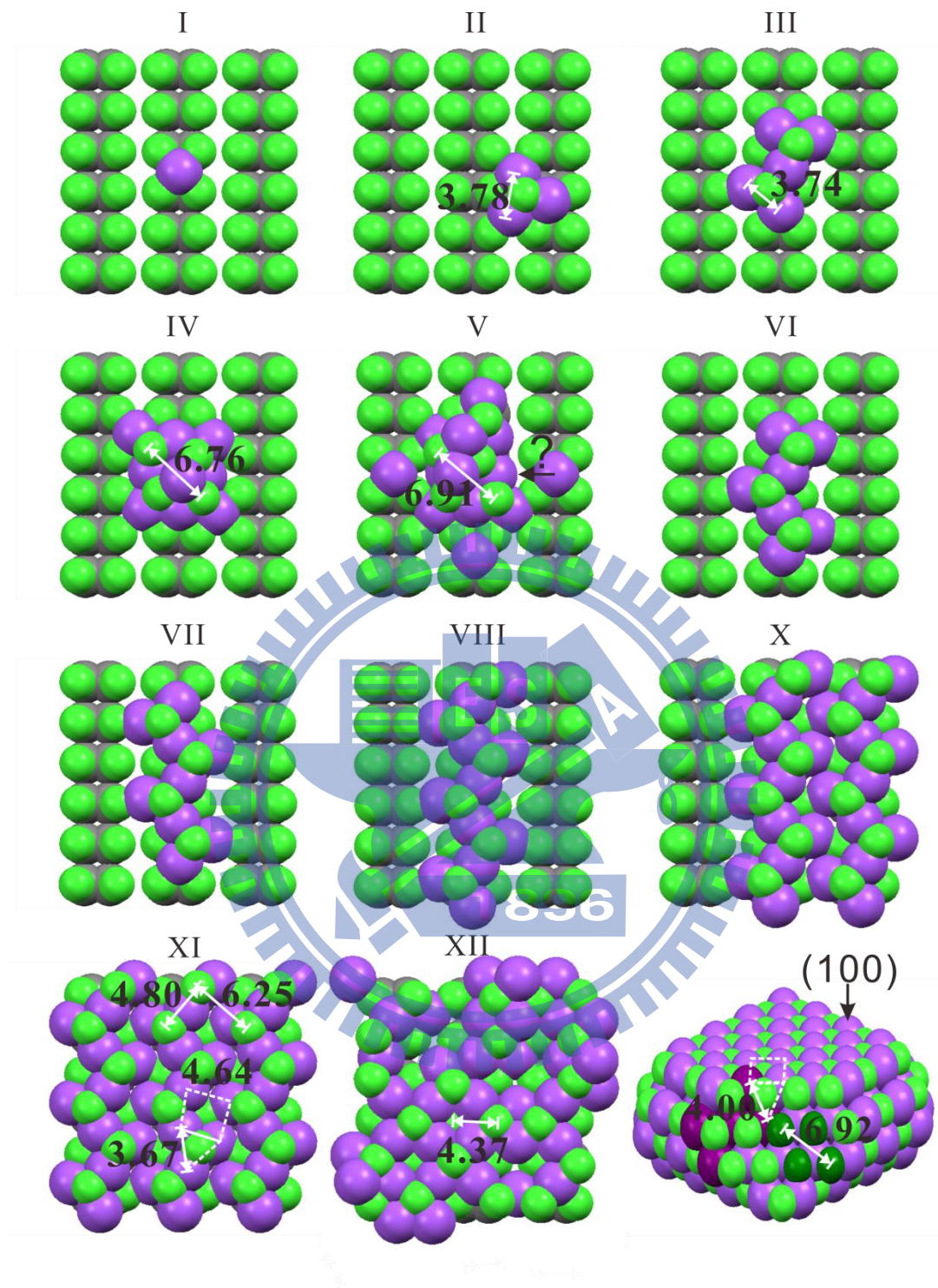


Figure 5.3.5 (I)-(V) structures were calculated by static relaxation after “annealing”, (VI)-(XII) structures were calculated by static relaxation, and (XII) was calculated by static relaxation from predetermined coplanar NaCl(100) layer after “annealing”.

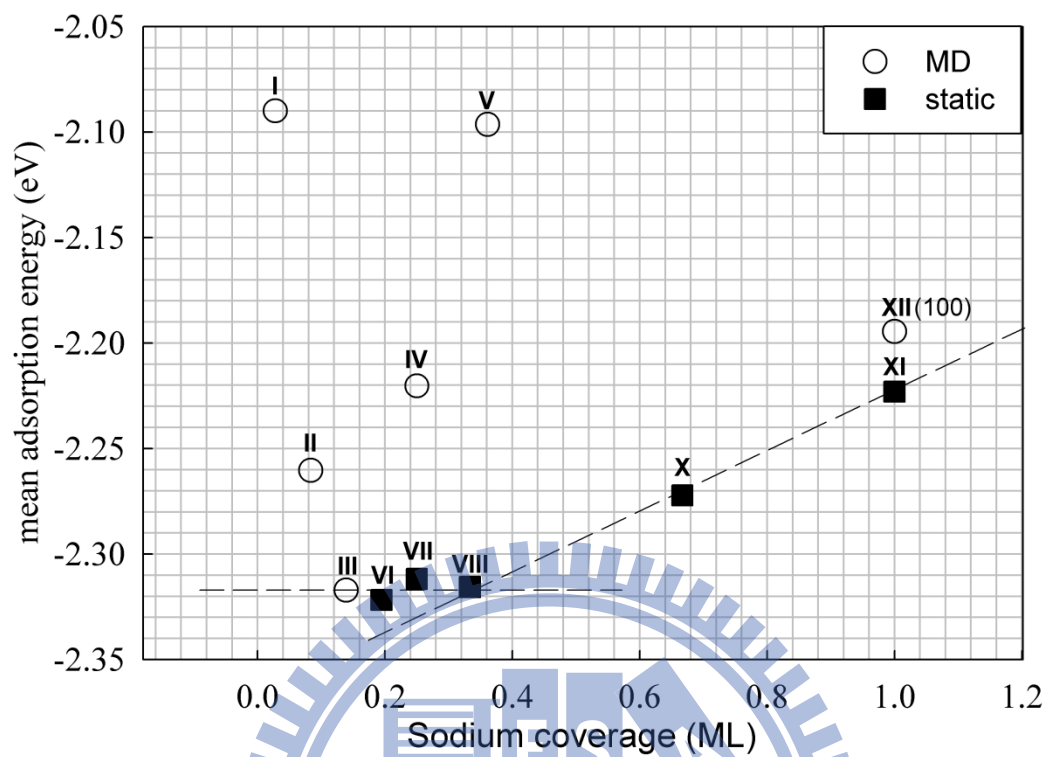


Figure 5.3.6 Mean adsorption energy diagram of various structures.

Chapter 6 Computational results (II): Electronic properties

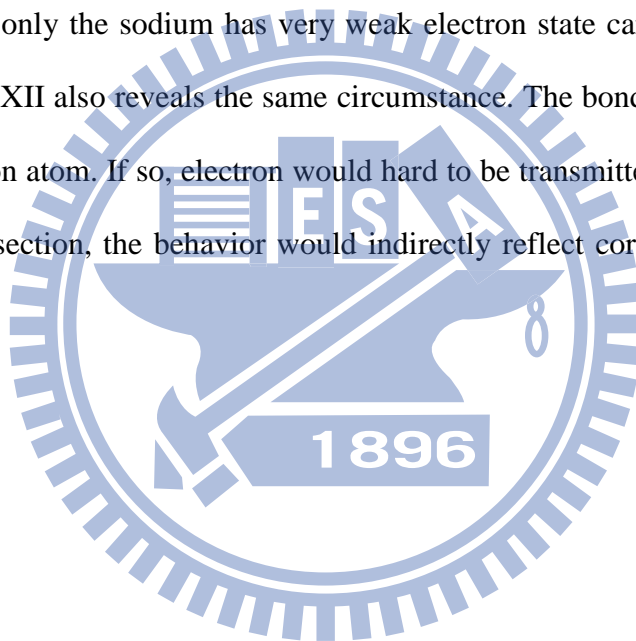
6.1 Density of State

In this section, we show a series of DOS and PDOS results. All spectra were calculated by $4 \times 4 \times 1$ automatic Monkhorst-Pack K point mesh with tetrahedron smearing method with Blöchl corrections. The projected radius were 1.312 \AA , 1.111 \AA , 1.757 \AA for Si , Cl , Na respectively. In order to subtract the error induced from the Fermi level position definition, the energy level of each case was calibrated by the Si $1s$ core level eigenvalue.

We first consider the DOS of 1 ML chlorine saturated surface. Fig. 6.1.1 exhibits a band gap of about 1.15 eV; which value is very close to the experimental results (1.12 eV) for bulk silicon. Surface Si , Cl were bonded with covalent σ bonds with a DOS between 0 to -5 eV. Upon single sodium adsorption, Fig. 6.1.1 tells us that the sodium was bonded with surrounding Chlorine by covalent-like bonding around -3 to -5 eV. Around the Na adsorption site, Si-Cl bonds becomes rather weak than before. More sodium coverage, Fig. 6.1.2 indicates the sodium and chlorine atom in the NaCl(111) cluster are held together by very local electrostatic interaction which corresponds to very sharp PDOS around -2 to -2.5 eV. Notably, relevant silicon atom exhibits unusual a “dangling bond state” which means the atom has metallic-like electrons. At 5/36 ML sodium coverage, the DOS becomes broader. When the NaCl forms a NaCl(111) cluster; As indicated by the type IV and V in Fig. 6.1.3, the DOS of both chlorine and sodium would become very broad and complex. We may note, in passing, the PDOS of silicon has a metal induced gap state (MIGS)^{90, 91} in around 0 to 0.5 eV; the behavior would decrease the band gap of system. In a manner of speaking,

it can be regarded as a result of heavy metal doping. Furthermore, if the NaCl(111) cluster is arranged as a long chain along the dimer. The type VIII in Fig. 6.1.4 tells us that the Na and Cl bond level would become very local. There are two major discrete bond states around -1.8 to -2.2 eV and -3.0 to -4 eV in the case. Only the bond state with higher energy located at the lower chlorine atom could contribute to tunneling current under our experimental scan bias (-2 V).

For higher sodium coverage, the PDOS result in the type XI case indicates that sodium and chlorine are bonded at a lower energy level than before. In this condition, under our scan bias (-2 V), only the sodium has a very weak electron state that can be detected. The last cases of type XII also reveal the same circumstance. The bonding between NaCl and surface Silicon atoms. If so, electrons would be hard to be transmitted. As we shall see in the following section, the behavior would indirectly reflect a core level shift in the XPS spectra.



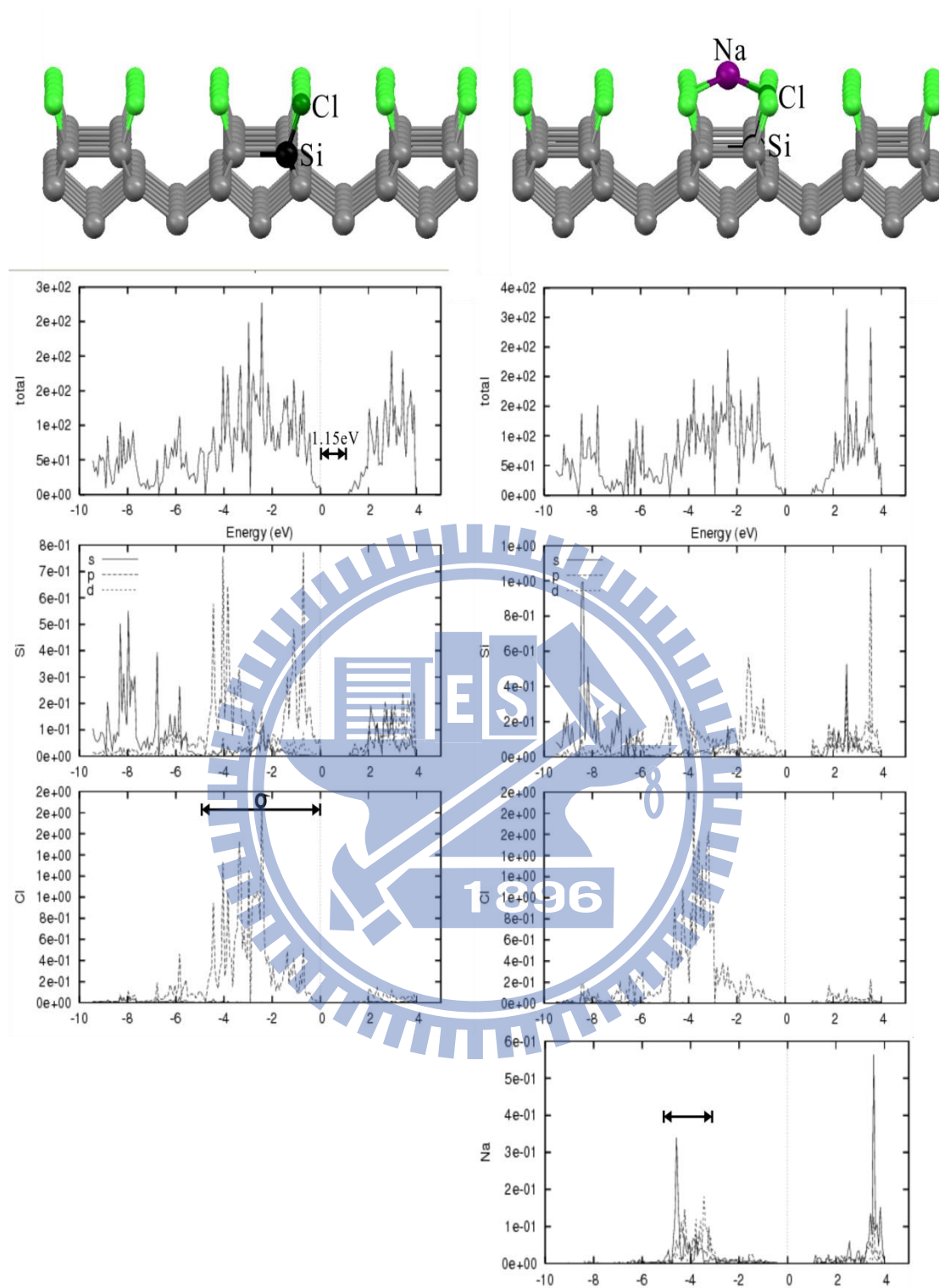


Figure 6.1.1 DOS of chlorine pre-covered case (left) and single sodium adsorption case (type I). The atom used for computing project density of state (PDOS) was marked with darker color.

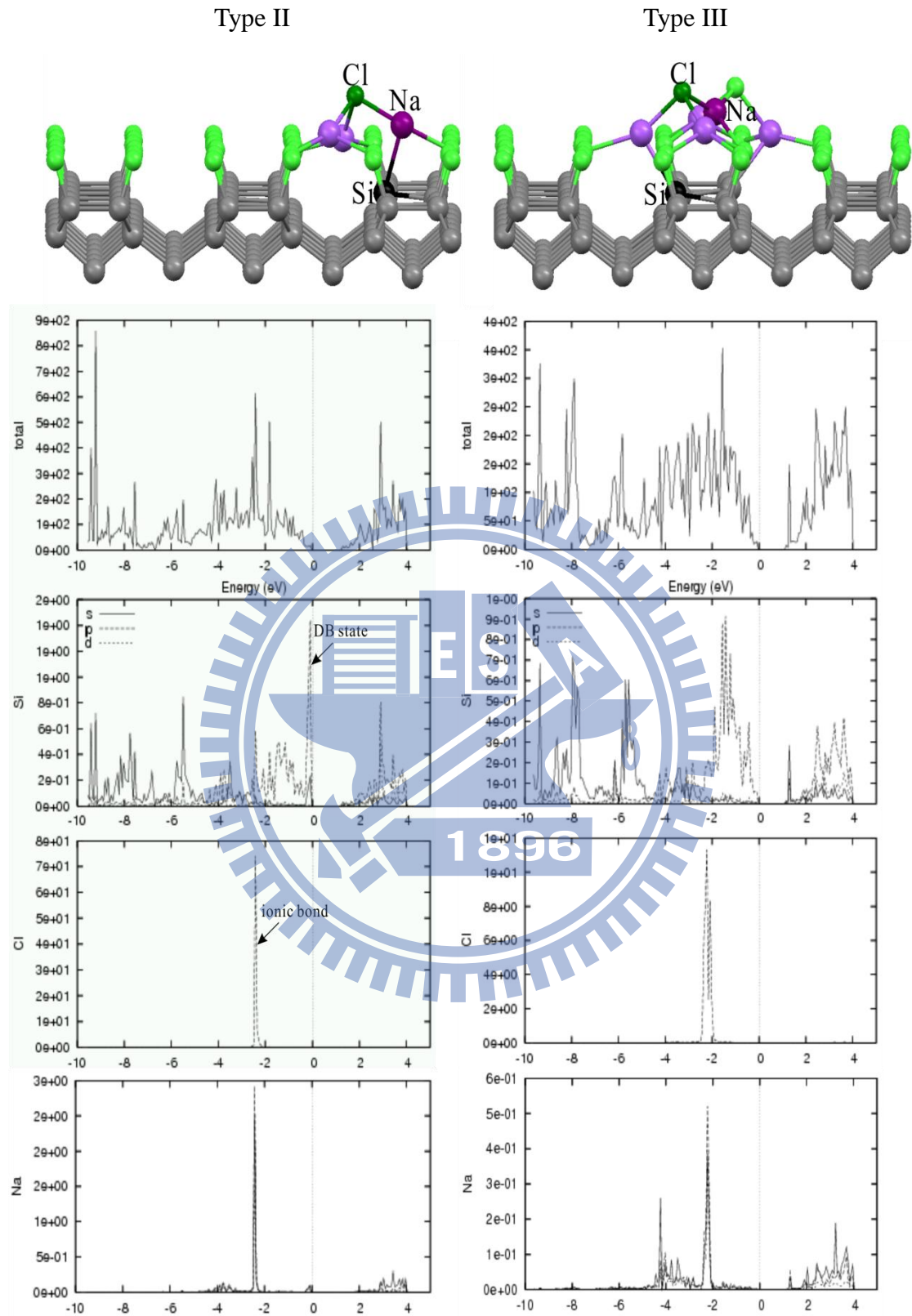


Figure 6.1.2 DOS of the type II (3/36 ML) and (b) type III case (5/36 ML).

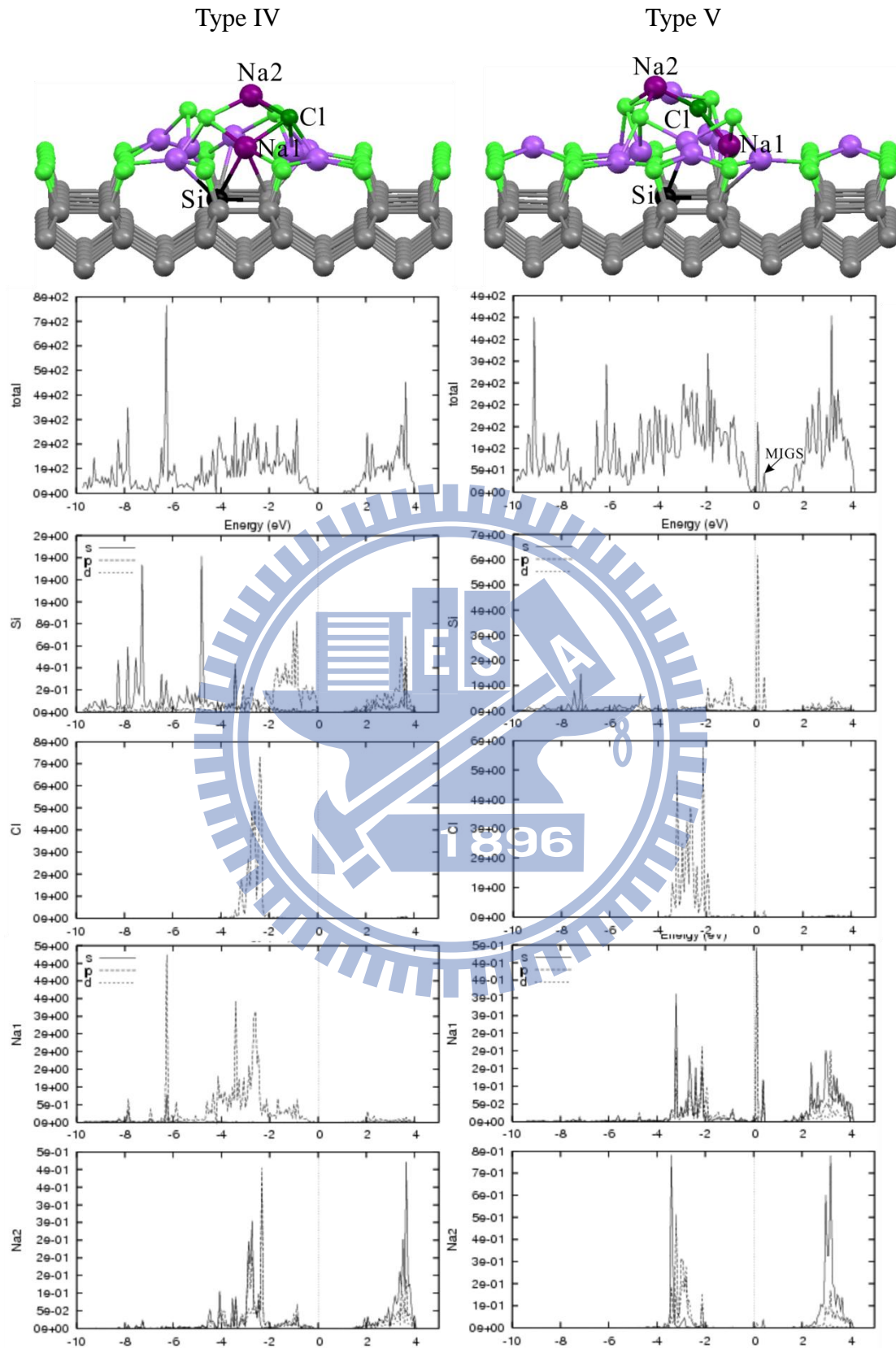


Figure 6.1.3 DOS of the type IV (9/36 ML) and type V case (13/36 ML).

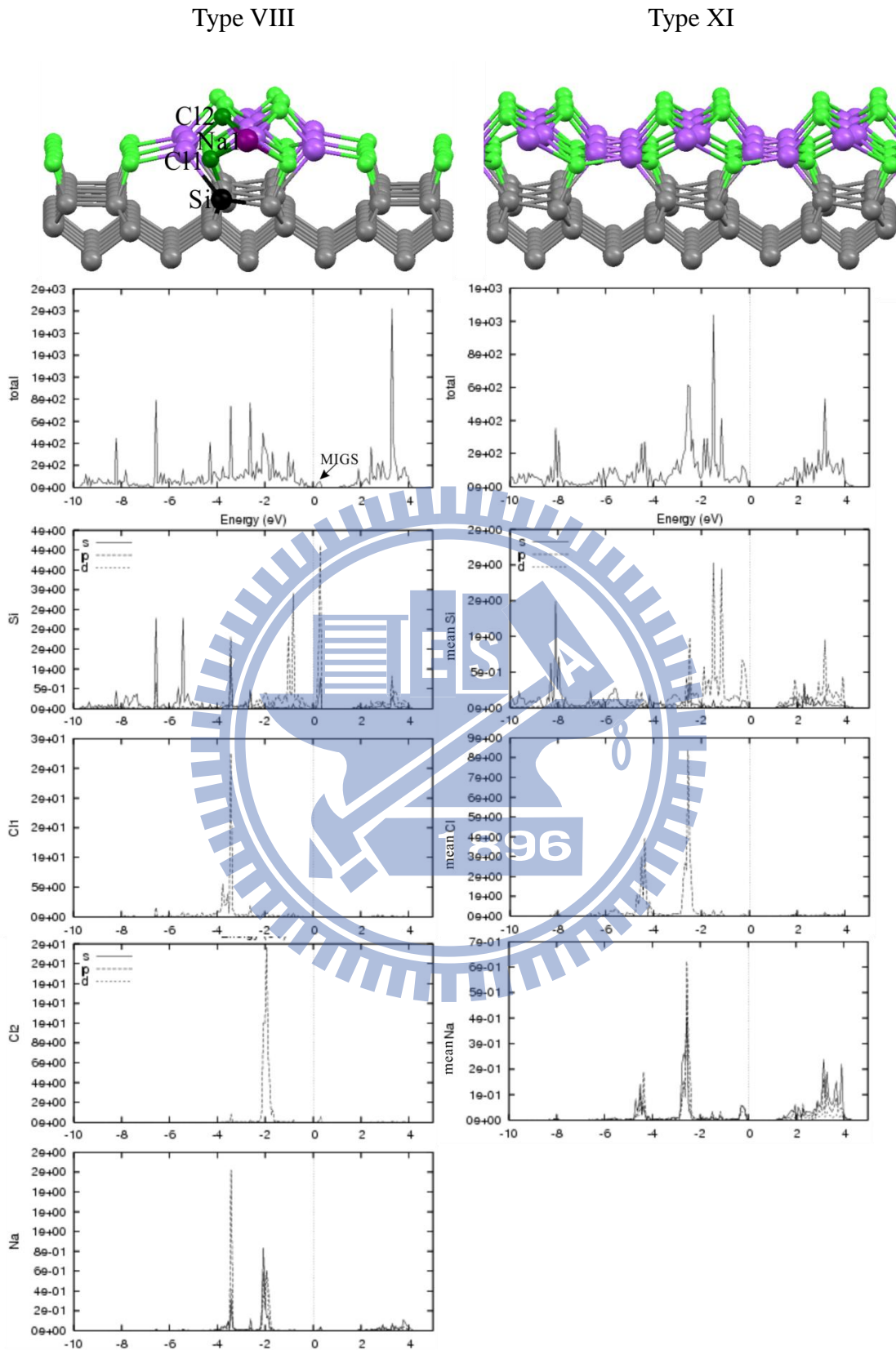


Figure 6.1.4 DOS of the type VIII (12/36 ML) and type XI case (36/36 ML).

Type XII

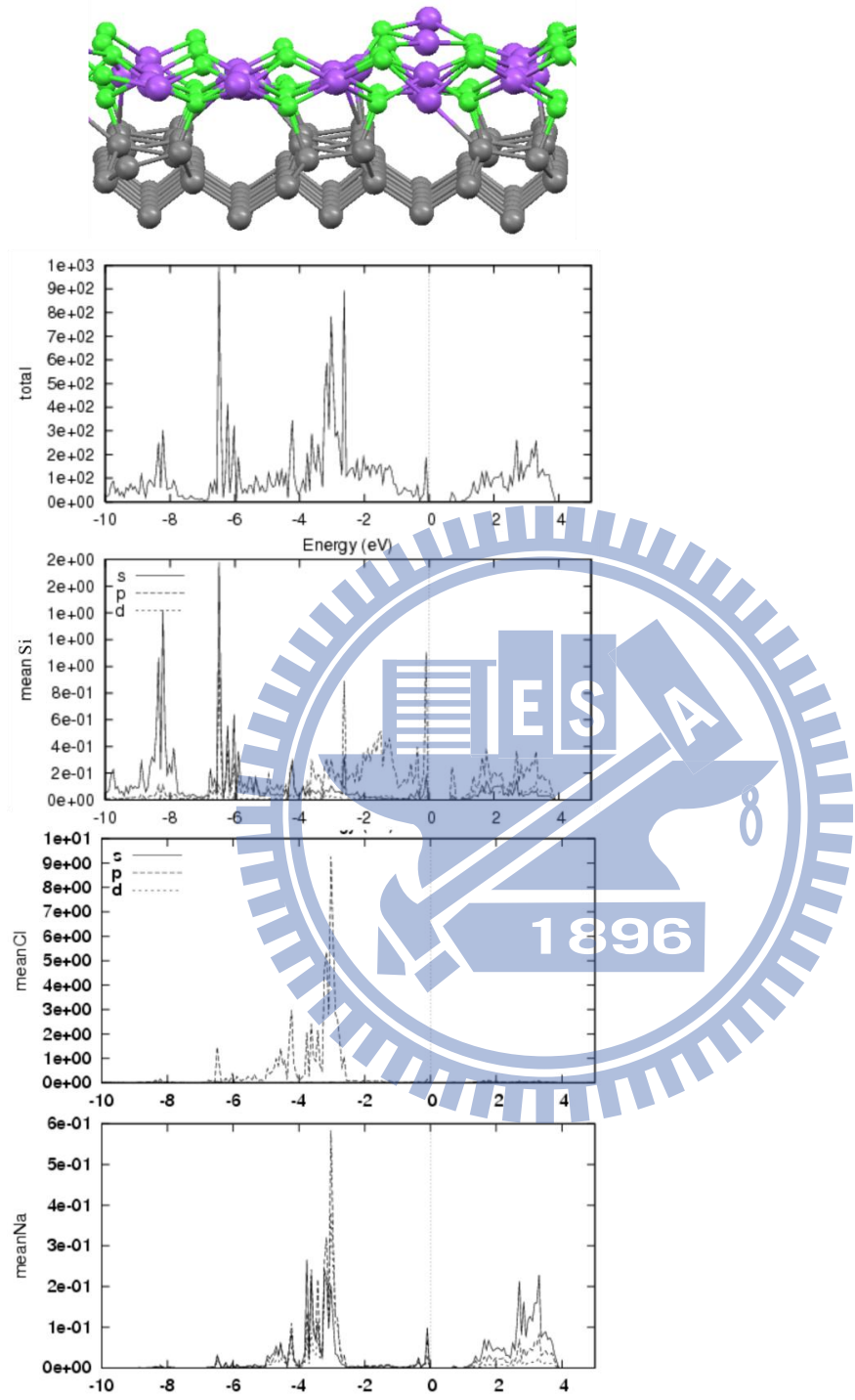


Figure 6.1.5 DOS of the type XII case (36/36 ML)

6.2 STM simulations

Bardeen's treatment of a tunnel junction based on perturbation theory laid the groundwork for the first theoretical STM model^{92, 93}. The tunneling current in Bardeen's formalism is expressed:

$$I = \frac{4\pi e}{\hbar} \int_0^{eV_{bias}} \rho_s(E_f - eV_{bias} + E) \rho_T(E_f + E) |M_{\mu\nu}|^2 \quad (6.3.1)$$

where ρ_s , ρ_T denote the density of states (DOS) of the sample and the tip, $M_{\mu\nu}$ is the matrix element for the transition of an electron between a sample wave function and tip wave function. If the experiments are performed at room temperature and small voltage, we take the limits of small voltage and temperature:

$$I = \frac{2\pi}{\hbar} e^2 V \sum_{\mu,\nu} |M_{\mu,\nu}|^2 \delta(E_\mu - E_F) \delta(E_\nu - E_F) \quad (6.3.2)$$

If the tip wave functions are arbitrarily localized, then the matrix element is simply proportional the amplitude of ψ_ν at the position \mathbf{r}_0 of the probe. Hence, Eq. 6.3.2 reduced to: $I = \sum_\nu |\psi_\nu(\mathbf{r}_0)|^2 \delta(E_\nu - E_F)$ (6.3.3)

The quantity on the right is simply the surface local density of state (PDOS) at E_F , the charge density from states at E_F . Thus the tunneling current is proportional to the surface PDOS at the position of the point probe, and the microscope image represents a contour map of constant surface PDOS which is known as Tersoff- Hamann approximation⁹⁴⁻⁹⁷. In this section, we follow the T-H approximation, to project the PDOS on a plane along +z direction; that plane is fixed at 2.0 Å above topmost chlorine atom for each cases. In order to compare with our experiment data, the integrated energy region is from 0 to ±2 eV relative to Fermi level. A series of simulated STM results and their configurations are presented in Fig. 6.2.1.

For 1 ML chlorine per-covered surface, under different bias condition (energy

region of PDOS), they both reveal p-(2x1) ordered pattern but have a small displacement along x- direction. That is due to different PDOS shape of them, highest density of occupied state of chlorine is along x-y direction, but that in unoccupied state is along x-z direction. So, after a project operation, a small displacement appears. For the single sodium adsorbed surface (type I), the area around the sodium atom displays different brightness under different bias conditions. If so, the area should show a symmetrical square. However, the pattern had never been observed in our STM result. As we mentioned before, because the sodium atoms can easily diffuse on surface; therefore single Na adsorption sites only exist under a low sodium coverage or low temperature condition.

For more sodium coverage, simulated results of type II and III tell us that the area blocked by NaCl cluster should be corresponding to darker spot. The reason is that because both sodium and chlorine form in cluster they almost didn't have any DOS in the energy region we used in STM experiment (-2 V). Therefore, under constant current mode condition, through the feedback system, the tip must be more close to the surface to detect constant current. Therefore, although the area has higher topography but it would look to be darker than others. The simulated image for type IV gives very complex result .Because in the case the pyramidal cluster has very large altitude difference. I think the simulation method by projecting DOS on a plane is incapable to handle such complex steric cluster. Therefore, I cannot give more discussion for the images this case. The simulated STM image for periodic triangular cluster in along (VIII) and perpendicular (XI) with dimer are shown in Fig. 6.2.2; which tells us that the chlorine atom in lower position is also brighter than upper chlorine atom. The reason is similar as we mentioned before. Finally, the simulated STM image of the case VIII displays very complex pattern; in basically, the structure

has ununiform altitude; technically, the image is strongly depends on the height of projected plane what we used. In the case, Chlorine and sodium atom they have almost the same brightness. The result seems roughly to fit the STM image. Both chlorine and sodium can be detected in this case. The result, in a manner of speaking, is corresponding to the STM image of 1 ML sodium covered case. In summary, the simulation result totally fit in experiment STM images.



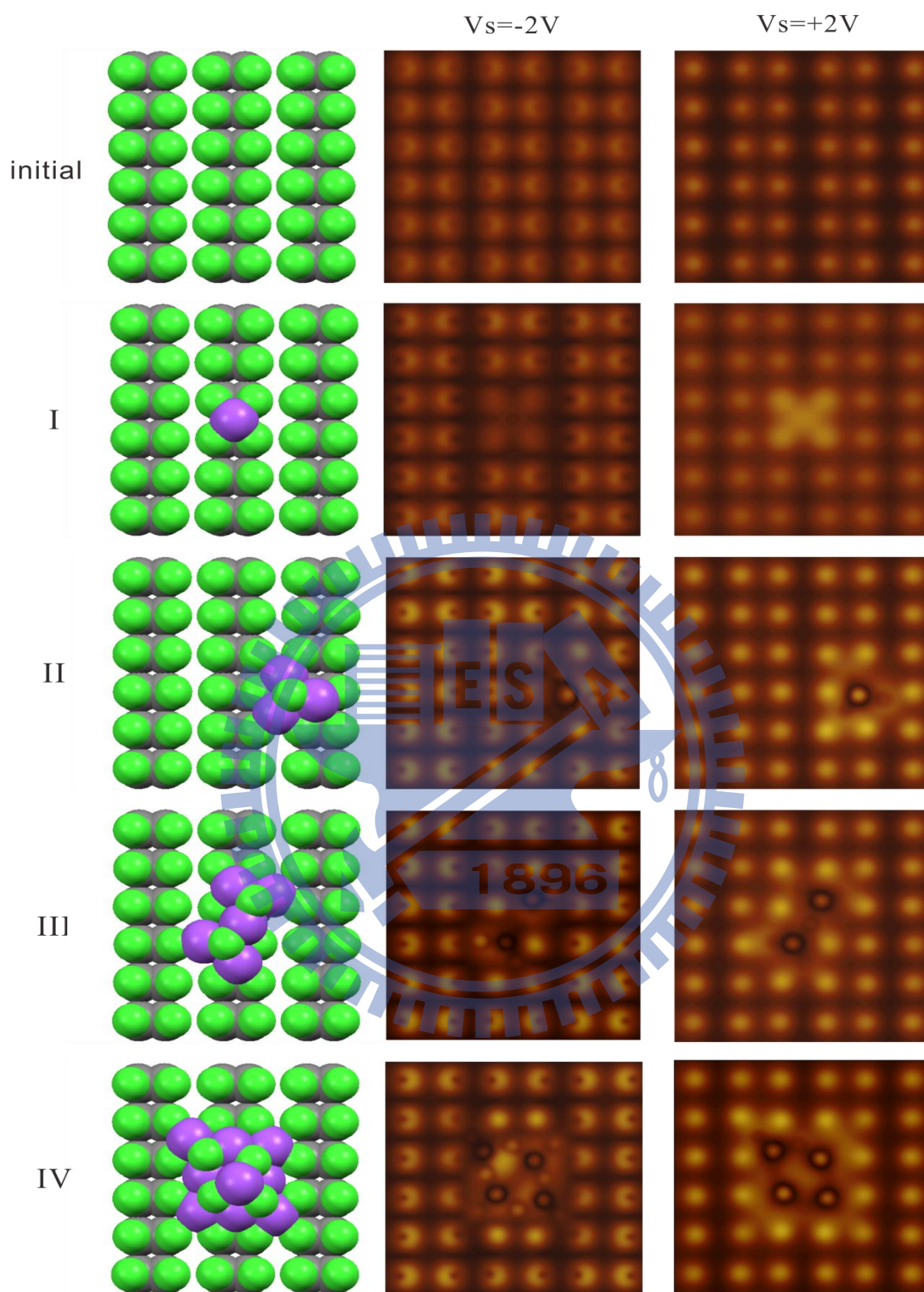


Figure 6.2.1 A series results of STM simulation for fill state ($V_s = -2\text{ V}$) and empty state ($V_s = +2\text{ V}$). The projection plane is placed on about 2 \AA above topmost chlorine.

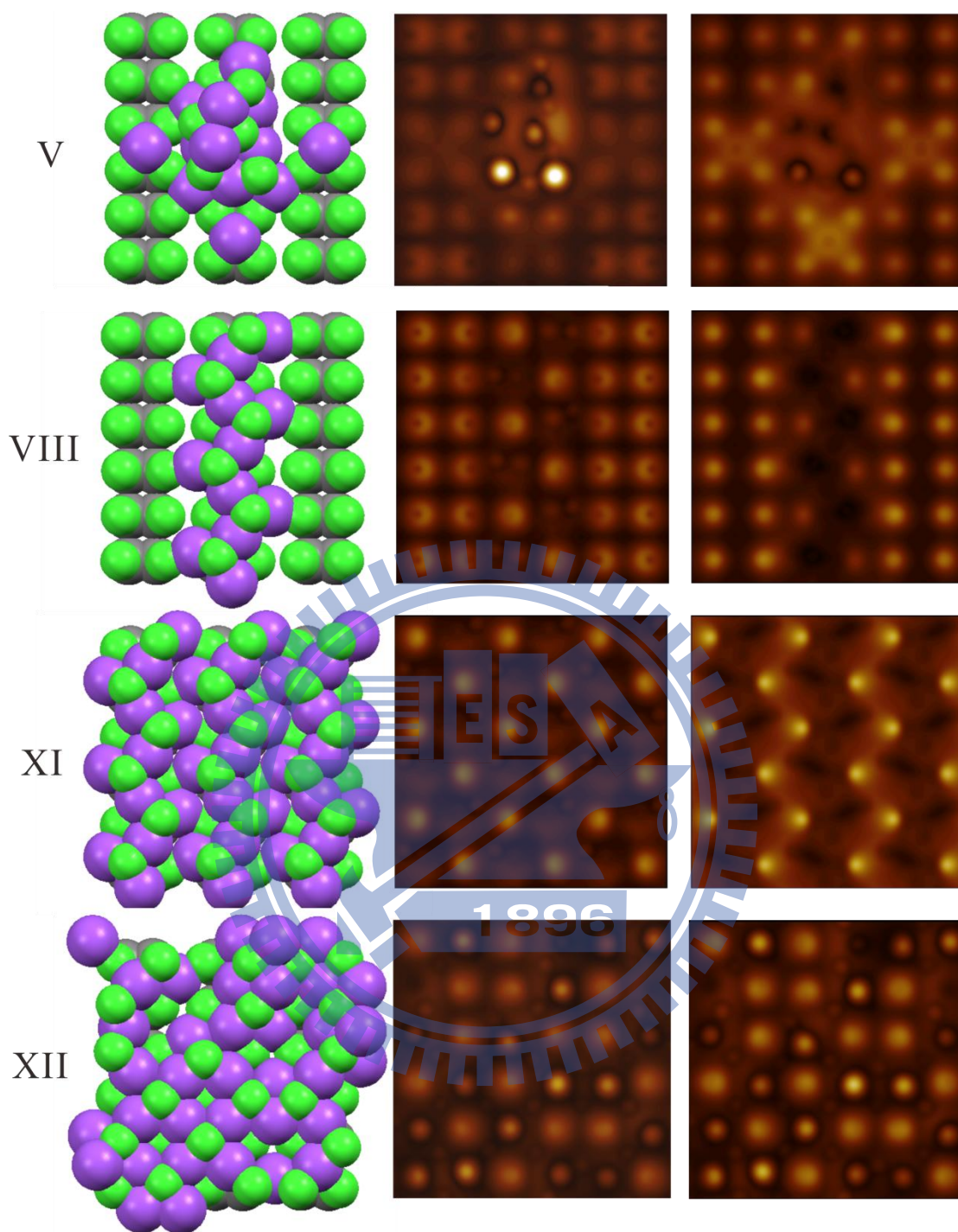


Figure 6.2.2 A series results of fill state ($V_s = -2$ V) and empty state ($V_s = +2$ V) simulated STM images. The projection plane is placed on about 2 Å above topmost chlorine.

6.3 Bader charge and core level shifts

As shown in Fig. 6.3.1, an atom can be defined as a region bounded by a surface through which no gradient vectors of ρ , meaning that the surface is not crossed by any trajectories of $\nabla\rho(\mathbf{r}_s)$. In other words, an interatomic surface (IAS) satisfies the “zero-flux” boundary condition: $\nabla\rho(\mathbf{r}_s)\cdot\mathbf{n}(\mathbf{r}_s) = 0$ for every point \mathbf{r}_s on the surface $S(\mathbf{r}_s)$ where $\mathbf{n}(\mathbf{r}_s)$ is the unit vector normal to the surface at \mathbf{r}_s . By integrating the electron density within each region we further quantitatively examine how valence charge distributes^{98,99}.

The theoretical models for the calculations of the core-level binding energy shifts within density functional theory (DFT) can be classified in two major groups, based on the complete screening picture, the initial state approximation and the final state model, respectively. In Fig. 6.3.1, an atom is shown in its (a) initial state A, and (b) final state A* after the ejection of a core-electron from state i . The resulting core-hole is assumed to be completely screened, as indicated by the extra charge in the local valence band DOS at the atom, effectively corresponding to one extra electron in the valence band. This is modeled in the calculations by promotion of an electron to the lowest unoccupied valence state, preserving the charge-neutrality of the system.

The core electron binding energy in the initial state approximation (IS)¹⁰⁰ can be calculated from the Kohn-Sham eigenvalues of the core state of interest ε_c and the Fermi level ε_f : $E_{CL}^{init} = \varepsilon_c - \varepsilon_f$ (6.3.1)

In the final state approximation (FS)¹⁰¹⁻¹⁰³, the electrons are allowed to relax after the core electron has been removed, so that the localized hole is screened. In general, the final state approximation that simulate including somewhat excited state behavior; the

core electron binding energy shifts between the bulk and the surface are expected to agree well with experiment. However, final state approximation has to be calculated by very complex procedure. First, a core electron is replaced by a valence one, then total energy difference between bulk and surface atom is calculated; The method can estimate the core hole effect only for only substrate (silicon). Each the case needs thirty six separate calculations which would cost very large computing resource and time. Therefore, we picked only a few specific atoms for the final state calculation.

The surface core-level binding energies shifts were defined as¹⁰⁴:

$$E_{SCLS}^{is(fs)} = [E_{surf}(n_c - 1) - E_{surf}(n_c)] - [E_{bulk}(n_c - 1) - E_{bulk}(n_c)] \quad (6.3.2)$$

In order to eliminate the error caused by relative Fermi level shift; we choose the bulk state Si 2*p* eigenvalue as a reference level to calibrate energy for following calculations.

In the case of chlorine-terminated surface about 0.64 electron transferred from silicon to its associated chlorine atom, which corresponds to +0.60 eV RCLS (IS) in Si 2*p* state. If we consider the core hole effect (FS), the number would be increasing by about 0.23 eV. The result indicates, the excited core hole in chlorine bonded silicon is more difficult to be screened than bulk silicon. The result calculated by FS approximation is smaller than experiment number of about 0.07 eV. In the case I, the central adsorbed sodium atom (No. 1) contributes about 0.85 electrons to surrounding chlorine atom (No. 2). The RCLS (IS) of surrounding Cl atom also increased of 0.65 eV relative to unreacted Cl atom (No. 3). In the case II, the RCLS (IS) of buried silicon (No. 3) decreased to -0.5 eV; and its Bader charge also reduces to 0.1 electrons; which suggesting that the associated silicon atom recovers its dangling bond (DB) state. In the case III, IV and V, the Bader charge of buried silicon in those cases increases

with the sodium amounts, which results in the reduction of RCLS (IS). The final state results also indicate the buried silicon atom has metallic-like electron state, as we mentioned before, that also reflects to their metal induced gap state (MIGS) of valence electron. But in fact, we didn't find a peak have such large shift (-1.21 eV) in experiment. In combination of previous results of energetic calculation; that tells us that case may account for only a small proportion of the whole surface structure. Furthermore, in case VIII, the upper and lower chlorine atom has different RCLS; there were 94.28 eV and 96.14 eV for upper and lower chlorine atom respectively, which roughly corresponds to their two kinds of valence bonding in around -2 eV and -4 eV (see Fig. 6.1.4 (a)). The extended case XII also reveals similar result, which indicates the experimental continuous Cl 2p RCLS should be interpreted as a result of superposition of the chlorine in NaCl(111) and NaCl(100) states. RCLS of sodium also reveals similar trend but shift with smaller number. We may note, in passing, the RCLS of buried silicon gradually retrieves electron and try back to its dangling bond state. For the last case, as we can see the No. 1 chlorine atom that has about 95.48 eV RSCLS; which almost equal to the average number of previous two different chlorine atom. Here, we can notice that RCLS of surrounding sodium also enhanced approximately +1 eV. From the point of view of band theory, When the NaCl gradually formed into large-scale structure. The group band shifts should be considered instead of individual atomic chemical shifts. Therefore, for higher sodium coverage, the same quantity of RCLS in Na 2p and Cl 2p state actually reflects the group valence band shift of NaCl(100) thin film. The result servers as good explanation for previous XPS data. Actually, continuous peak shift of Na 2p and Cl 2p is precisely reflected structure phase transition with varying of sodium coverage.

In summary, the Bader charge result show that charge redistribution depends on

their relative electronegativity difference. Adsorbed sodium atoms are electron donors; the valence charges of the sodium and chlorine atoms are preserved during the growth process. The substrate silicon atoms are electron acceptors and their valence electron counting change significantly. For surface silicon atoms, RCLS has indeed responded accordingly the charge transfer behavior between the interfaces. Without the signals from the bulk, RCLS of chloride and sodium atoms changes their corresponding binding energies.

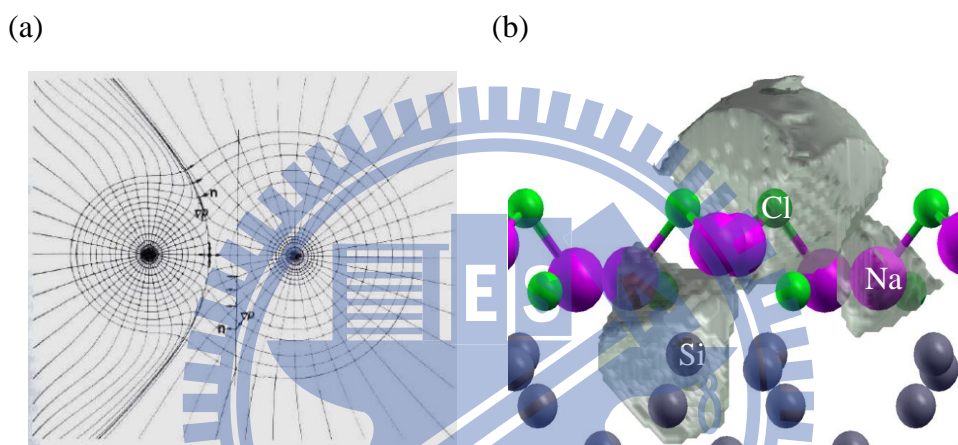


Figure 6.3.1 (a) Contour map of NaCl overlaid with trajectories of $\nabla\rho$, and (b) Bader partition volume of our system. ((a) cited from

<http://www.chemistry.mcmaster.ca/bader/bio/highschool.htm>)

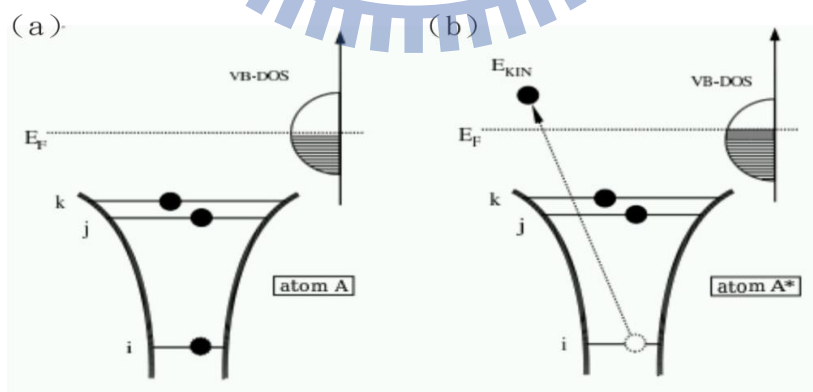


Figure 6.3.2 (a) Initial and (b) final states of the photoemission process. The effect of screening is shown by the increased occupation of the local valence band DOS in (b) compared to (a). (cited from Phys. Stat. Sol. (b) 243, 2447 (2006))

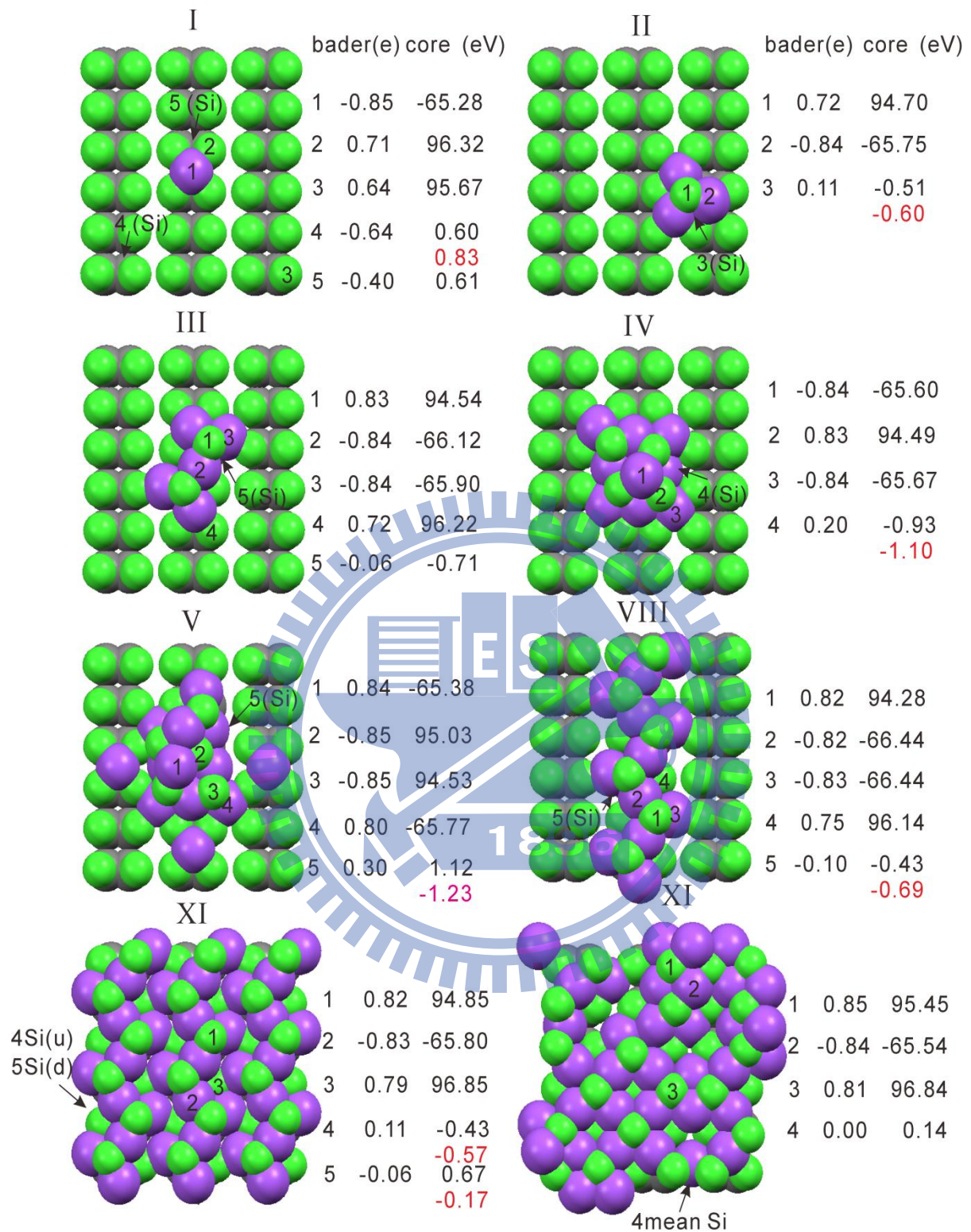


Figure 6.3.3 Net Bader charges ($q_{\text{bader}} - q_{\text{neutral}}$) and RCLS (relative to Si $2p$ bulk) for specified atoms. The final state results of Si $2p$ states are labeled in red.

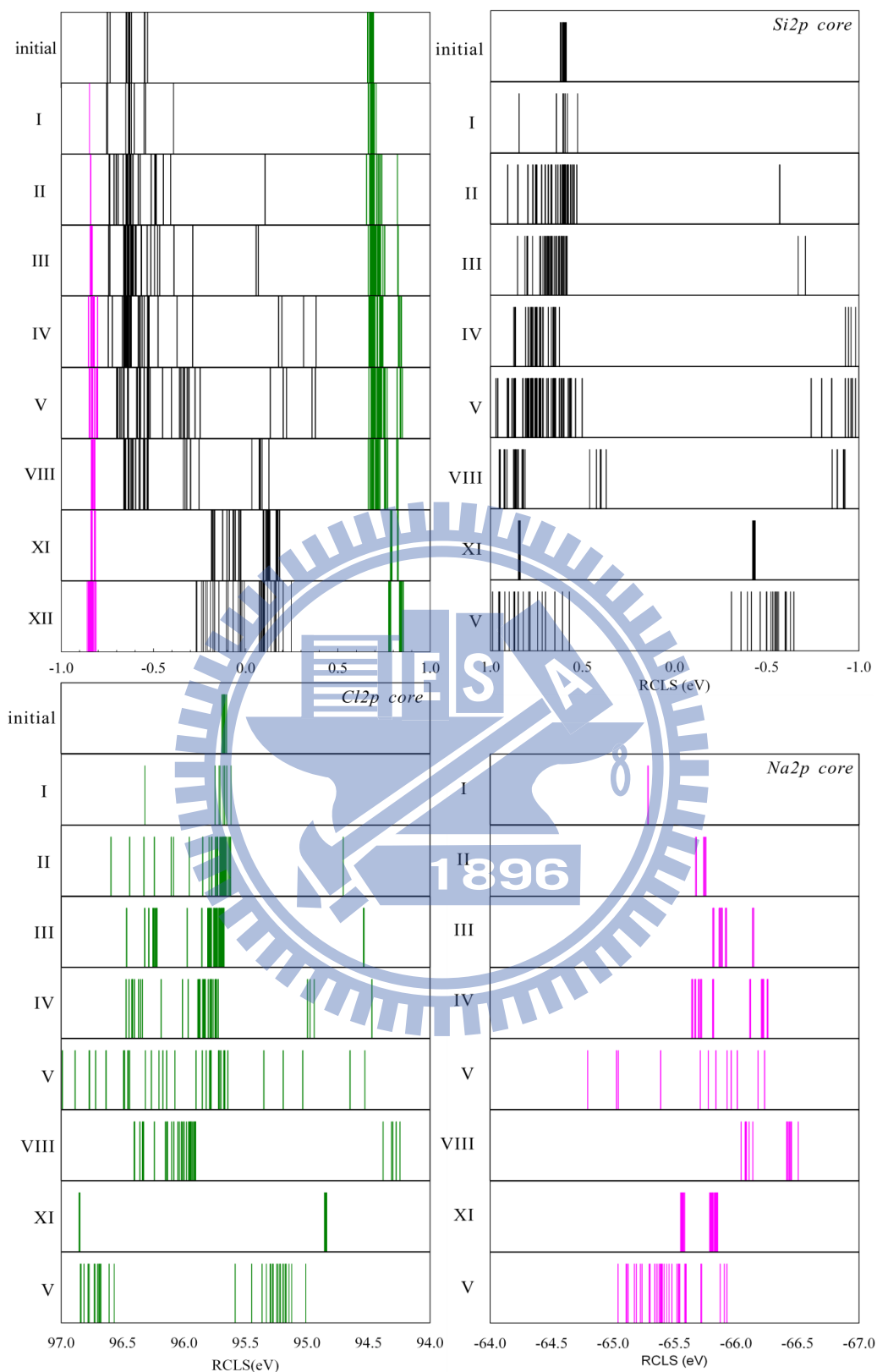


Figure 6.3.4 (a) Detailed net Bader charge and (b)-(d) RCLS (relative to Si 2p bulk) in all of the surface atoms. Each case includes thirty-six data points.

Chapter 7 Conclusion

In this research, we have studied the morphology, electronic states and interface properties of the simplest and yet significant heteroepitaxial system. The atomic layer deposition (ALD) technique enabled us to produce various functional thin films in atomic level. The self-limited reaction serves as great stage for understanding the interaction between dissimilar atoms. By a combination of the two concepts, we designed a two-step reaction to grow a atomic layer of ionic NaCl.

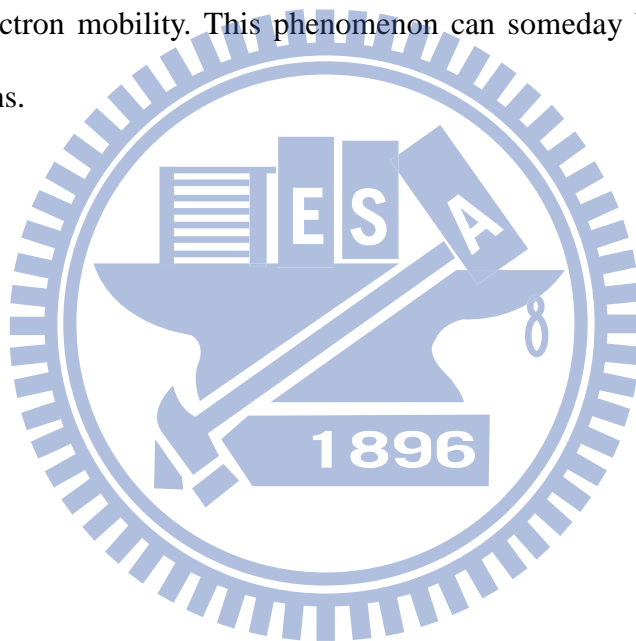
The first principle calculation results indicate that molecular chlorine can spontaneously dissociative chemisorbs on the clean Si(100) surface forming p(2x1) chlorine-terminated surface without extra energy input. The nearest neighbor distance between surface chlorine atoms (3.86 Å) is very close to that in typical NaCl crystal (3.99 Å). Each chlorine atom received about 0.67 electrons from the bonded silicon atom, resulting in a polar surface. A sodium atom prefers to adsorb on the hollow site between surface chlorine atoms, and donates about 0.85 electrons to the nearby chlorine atoms. So the partial ionic bonding would be form to replace Si-Cl covalent bonding. However, the singly-adsorbed structure had never been observed in our STM images. By the NEB method, we figured out the diffusion barrier along and perpendicular to the dimer row is only about 0.5 eV. In other words, the single adsorption case can be observed only under very dilute sodium dosage or at low temperature. It tells us that the dim spot, we observed in STM images, is consisted of cluster formation.

We have employed several simulation methods to find possible NaCl 2D structure. Static calculation results indicated two sodium atoms adsorbing on adjacent hollow site would result in energy increasing. The result implies that the cluster must

be form in other arrangement in the initial stages of heteroepitaxy. Furthermore, the AIMD result suggests the sodium and chlorine atoms tend to form (111) phasic NaCl clusters. Each cluster unit contains three sodium and one chlorine atom. The clusters also prefer to assemble along 2D plane instead of 3D stack. From an electrostatic point of view, the growth of NaCl clusters along its '(111)' direction would result in very strong surface dipoles. However, previous studies have reported that non-equilibrium growth shapes are also observed for a range of finite temperatures^{3, 105}. Our simulated results indicate three possible formations of assembled clusters, the single cluster, 2D assembled clusters, and double-layer 3D stack they have only about 0.05 eV energy difference. They may correspond to the single dim spot, the p(2x2) and a collected area of dim spots in our STM images. Even though the topography of cluster is higher than other uncovered area, the clusters could correspond to dim spots in our STM images due to it is lacking of electron density of state under our scanning bias (-2 eV). With increasing sodium coverage ($\theta_{Na} = 0.5$), the cluster tends to grow along the dimer row. When the clusters gathered over a certain density, it would transform into NaCl(111)-(100) concomitant structure. They spell out which two bonded in two different energy level, one in about -2 eV, another in about -4 eV, which two bonding types are correspond to three fold (111) and four fold NaCl, respectively. From this point of view, the continuous spectra shift of Na 2*p* and Cl 2*p* peak in XPS spectra is induced by structure phase transition. The amount of shifts corresponds well to the formation ratio of NaCl(111) to NaCl(100). To put it the other way around, the XPS data strongly support our theoretical model. When sodium coverage reached one monolayer, the STM images indicates NaCl(111)-(100) would entirely transform into large scale and uniform NaCl(100) monolayer with random corrugations. The XPS spectra also show that the surface silicon regains its dangling

bond state; which means only Van Der Waals force is present between the interface of NaCl thin film and silicon substrate.

Finally, we demonstrated that the growth mechanism of Na on the Cl/Si surface follows Franck-van der Merve growth mode. As far as we know, the NaCl(100) monolayer is fabricated successfully for the first time. We also found unusual (100)-(111) concomitant phase in the system. In additional, we discovered that the thin NaCl films protected the dangling bond state of the surface silicon can be preserved for long time here. Such surface state usually has very high chemical reactivity and electron mobility. This phenomenon can someday become useful for device applications.



Appendix: Computation Conditions

common setting	
Program: Vienna Ab-initio Simulation Package (VASP) Pseudopotential: PAW-GGA-PBE Cut off energy for plane wave: 300 eV (22.06Ry) Without Spin	
Structural relaxation (from an unreasonable starting guess)	
k-point grid : 4x4x1 (Monkhorst-Pack)	
INCAR LREAL=A # fully automatic optimization of projection operator ALGO = Fast #RMM-DIIS for electron ISM EAR = -5 #DOS smearing method :-5=Tetrahedron IBRION = 2 # CG algorithm NSW = 10 #10 ionic steps for ionic step NELMIN = 5 # do a minimum of four electronic steps EDIFF = 1E-2 # low accuracy ($dE_e < 1.0E-2$) EDIFFG = -0.3 # accuracy of ions not too high($dE_i < 0.3$ eV/A)	
Structural relaxation (from pre-converged starting guess)	
k-point grid : 4x4x1 (Monkhorst-Pack)	
INCAR LREAL=A # fully automatic optimization of projection oper ALGO = Fast #RMM-DIIS for electron ISM EAR = -5 #DOS smearing :-5=Tetrahedron method NELMIN = 8 # do a minimum of ten electronic steps EDIFF = 1E-5 # high accuracy for electronic groundstate EDIFFG = -0.025 # small tolerance for ions NSW = 20 # 20 ionic steps should do MAXMIX = 80 # keep dielectric function between ionic movements IBRION = 1 # use RMM-DIIS algorithm for ions NFREE = 10 # estimated degrees of freedom of the system	

**Static calculation (after Structural relaxation)
generating more precise charge density and wavefunction for
1. DOS 2.Bader 3.Work function 4. Electron localization function
5.XPS simulation 6.STM simulation**

k-point grid : 4x4x1 (Monkhorst-Pack)

INCAR

```

LREAL    = A      #FFT project region
ALGO     = Fast   #RMM-DIIS for electron
ISMEAR   = -5     #Tetrahedron method
#####static calculation#####
IBRION=-1      #fix ion position
NSW=0        #fix ion position
#####convergent criteria#####
EDIFF=1.0E-6  #electronic
#####1.DOS#####
ISPIN= 1      # 2= spin , 1=without spin
EMAX=10      #energy(eV) boundary for DOS
EMIN=-10
RWIGS=0.370 1.312 1.111 1.757 # specify project radius(A)
#####2.All electron(for Bader) #####
LAECHG=.T.   #output all electron
#(increase FFT mesh: NGFX(Y)(Z)=2*NGX(Y)(Z) for better charge resolution)
#####3.workfunction (dipole)#####
LVTOT=.T.    #output LOCPOT
#####4.electron localization function#####
LELF=.TRUE.  #output ELFCAR
#####5.core level #####
ICORELEVEL =1 # 0,1,2(approx final/ initial /acc. final state)
CLNT = 1, 2, 3....# processing N-th species of atom
CLN = 1, 2, 3... # N quantum number
CLL = 0, 1, 2, 3 # orbital quantum number ( 0=s,1=p,2=d)
CLZ = 1        # (How many electron removed from core,0.5 for transition state)
#####6.STM #####

```

```

LPARD =.T.      # output PARCHG
NBMOD = -3     # calculate the range window .vs. Fermi level
EINT =-1       # project window ( eV)

```

Nudged Elastic Band

k-point grid : 1x1x1 (Monkhorst-Pack)

INCAR

```

LREAL= A      # fully automatic optimization of projection operator
ALGO = Fast   # RMM-DIIS for electron
ISM EAR = 0   # Gaussian smear for low K-point
SIGMA = 0.2   # Band width
#####NEB#####
NSW = 100     # max 100 ionic step
POTIM = 0.2   # counting time for ion(0.2fs)
IMAGES=8      # middle points
SPRING=-5     # Spring force between images (eV/A2)
LCLIMB=.T.    # turn on the climbing image algorithm
LWAVE = .F.   #don't write WAVECAR
LCHARG =.F.   #don't write CHGCAR and CHG

```

Vibrational frequency

k-point grid : 4x4x1 (Monkhorst-Pack)

```

LREAL= A      # fully automatic optimization of projection operator
ALGO = Fast   # RMM-DIIS for electron
ISM EAR = -5  # Tetrahedron method
#####Vib#####
IBRION = 5    # Hessian matrix calculation
NSW = 100    # 100 ionic steps
ENCUT = 300  # energy cut off for pseudopotential
POTIM =0.05  # counting time for ion (fs)
NFREE =2     # degree of freedom

```

Molecular Dynamics

k-point grid : 1x1x1 (Monkhorst-Pack)

INCAR

LREAL= A # fully automatic optimization of projection operator

ALGO = Fast # RMM-DIIS for electron

ISMEAR = 0 # Gaussian smear for low K-point

SIGMA = 0.2 # Band width

#####MD#####

IBRION = 0 # For MD calculation

SMASS = -3 # -3 : micro canonical ensemble (NEV)

-2: constant velocity(for calculating Morse potential)

-1: Annealing

>=0: canonical ensemble (NTV) with Nosé-mass

POTIM = 2 # step size (fs)

TEBEG = 300 # initial temperature

TEEND = 300 # final temperature

NSW = 1000 # 1000 ionic steps

LCHARG = .F. # don't write CHGCAR

LWAVE = .F. # don't write WAVECAR

Reference

- 1 F. E. Olsson and M. Persson, *Surface Science* **540**, 172 (2003).
- 2 E. Le Moal, M. Müller, O. Bauer, and M. Sokolowski, *Surface Science* **603**, 2434
(2009).
- 3 W. Hebenstreit, M. Schmid, J. Redinger, R. Podloucky, and P. Varga, *Physical
Review Letters* **85**, 5376 (2000).
- 4 M. McEllistrem, M. Allgeier, and J. J. Boland, *Science* **279**, 545 (1998).
- 5 U. L. Bernard, E. I. Izgorodina, and D. R. MacFarlane, *The Journal of Physical
Chemistry C* **114**, 20472 (2010).
- 6 Z. Jing and J. L. Whitten, *Surface Science* **274**, 106 (1992).
- 7 S. B. Healy, C. Filippi, P. Kratzer, E. Penev, and M. Scheffler, *Physical Review
Letters* **87**, 016105 (2001).
- 8 M. C. Hersam, N. P. Guisinger, J. Lee, K. Cheng, and J. W. Lyding, *Applied
Physics Letters* **80**, 201 (2002).
- 9 C. Manzano, W. H. Soe, H. Kawai, M. Saeys, and C. Joachim, *Physical Review B*
83, 201302 (2011).
- 10 L. S. O. Johansson, R. I. G. Uhrberg, aring, P. rtensson, and G. V. Hansson,
Physical Review B **42**, 1305 (1990).
- 11 J. Gryko and R. E. Allen, *Physica B: Condensed Matter* **194-196**, 381 (1994).
- 12 M. Dubois, et al., *Physical Review B* **71**, 165322 (2005).
- 13 D. Wolf, *Physical Review Letters* **68**, 3315 (1992).
- 14 B. R. A. Nijboer and F. W. De Wette, *Physica* **23**, 309 (1957).
- 15 Gl, ouml, K. ckler, M. Sokolowski, A. Soukopp, and E. Umbach, *Physical Review
B* **54**, 7705 (1996).
- 16 Y. Wang, J. r. Kröger, R. Berndt, and H. Tang, *Journal of the American
Chemical Society* **132**, 12546 (2010).
- 17 C. Bombis, et al., *Physical Review Letters* **104**, 185502 (2010).
- 18 R. Bennewitz, V. Barwich, M. Bammerlin, C. Loppacher, M. Guggisberg, A.
Baratoff, E. Meyer, and H. J. Güntherodt, *Surface Science* **438**, 289 (1999).
- 19 J. Repp, G. Meyer, S. M. Stojkovicacute, A. Gourdon, eacute, and C. Joachim,
Physical Review Letters **94**, 026803 (2005).
- 20 L. Esaki and R. Tsu, *IBM J. Res. Dev* **14**, 61 (1970).
- 21 R. Dingle, A. C. Gossard, and W. Wiegmann, *Physical Review Letters* **34**, 1327
(1975).
- 22 S.-F. Tsay and D. S. Lin, *Surface Science* **603**, 2102 (2009).

- 23 A. Maximilian and et al., Nanotechnology **20**, 445301 (2009).
- 24 J.-Y. Chung, H.-D. Li, W.-H. Chang, T. C. Leung, and D.-S. Lin, Physical Review B
83, 085305 (2011).
- 25 A. D. Liehr, Annals of Physics **1**, 221 (1957).
- 26 A. Gordon and J. E. Avron, Physical Review Letters **85**, 34 (2000).
- 27 L. M. Loew and E. Sacher, Journal of Macromolecular Science, Part B: Physics
15, 619 (1978).
- 28 Canadian Journal of Physics **47**, 699 (1969).
- 29 E. R. Tuttle, Physical Review A **1**, 1758 (1970).
- 30 W. Kohn and L. J. Sham, Physical Review **140**, A1133 (1965).
- 31 P. Hohenberg and W. Kohn, Physical Review **136**, B864 (1964).
- 32 G. Teo, H. Wang, Y. Wu, Z. Guo, J. Zhang, Z. Ni, and Z. Shen, Journal of Applied
Physics **103**, 124302 (2008).
- 33 O. V. Yazyev, E. N. Brothers, K. N. Kudin, and G. E. Scuseria, The Journal of
Chemical Physics **121**, 2466 (2004).
- 34 M. E. Casida, C. Jamorski, K. C. Casida, and D. R. Salahub, The Journal of
Chemical Physics **108**, 4439 (1998).
- 35 J. P. Perdew and W. Yue, Physical Review B **33**, 8800 (1986).
- 36 K. Kunc and K. Syassen, Physical Review B **81**, 134102 (2010).
- 37 J. P. Perdew and A. Zunger, Physical Review B **23**, 5048 (1981).
- 38 D. M. Ceperley and B. J. Alder, Physical Review Letters **45**, 566 (1980).
- 39 J. P. Perdew, K. Burke, and M. Ernzerhof, Physical Review Letters **77**, 3865
(1996).
- 40 J. P. Perdew and Y. Wang, Physical Review B **46**, 12947 (1992).
- 41 M. Ernzerhof and G. E. Scuseria, The Journal of Chemical Physics **110**, 5029
(1999).
- 42 T. J. Giese and D. M. York, The Journal of Chemical Physics **133**, 244107
(2010).
- 43 B. Hammer, K. W. Jacobsen, oslash, and J. K. rskov, Physical Review Letters **70**,
3971 (1993).
- 44 Y. Zhang and W. Yang, Physical Review Letters **80**, 890 (1998).
- 45 F. Tran, P. Blaha, K. Schwarz, Nov, aacute, and P. k, Physical Review B **74**,
155108 (2006).
- 46 P. Rivero, C. Loschen, I. D. P. R. Moreira, and F. Illas, Journal of Computational
Chemistry **30**, 2316 (2009).
- 47 Canadian Journal of Chemistry **88**, 1057 (2010).
- 48 W. Knorr and R. W. Godby, Physical Review Letters **68**, 639 (1992).

- 49 H. Xiao, J. Tahir-Kheli, and W. A. Goddard, *The Journal of Physical Chemistry Letters* **2**, 212 (2011).
- 50 D. J. Chadi and M. L. Cohen, *Physical Review B* **8**, 5747 (1973).
- 51 H. J. Monkhorst and J. D. Pack, *Physical Review B* **13**, 5188 (1976).
- 52 G. Kresse and J. Furthmüller, *Computational Materials Science* **6**, 15 (1996).
- 53 Bl, ouml, P. E. chl, O. Jepsen, and O. K. Andersen, *Physical Review B* **49**, 16223 (1994).
- 54 M. Hasegawa and M. Watabe, *Journal of Physics C: Solid State Physics* **16**, L29 (1983).
- 55 J. S. Lin, A. Qteish, M. C. Payne, and V. Heine, *Physical Review B* **47**, 4174 (1993).
- 56 M. C. Payne, M. P. Teter, D. C. Allan, T. A. Arias, and J. D. Joannopoulos, *Reviews of Modern Physics* **64**, 1045 (1992).
- 57 D. R. Hamann, Schl, uuml, M. ter, and C. Chiang, *Physical Review Letters* **43**, 1494 (1979).
- 58 Bl, ouml, and P. E. chl, *Physical Review B* **50**, 17953 (1994).
- 59 G. Kresse, Furthm, uuml, and J. Iler, *Physical Review B* **54**, 11169 (1996).
- 60 B. Zhou and Y. A. Wang, *The Journal of Chemical Physics* **128**, 084101 (2008).
- 61 R. Car and M. Parrinello, *Physical Review Letters* **55**, 2471 (1985).
- 62 uuml, T. D. hne, M. Krack, F. R. Mohamed, and M. Parrinello, *Physical Review Letters* **98**, 066401 (2007).
- 63 P. Steneteg, I. A. Abrikosov, V. Weber, and A. M. N. Niklasson, *Physical Review B* **82**, 075110 (2010).
- 64 R. P. Feynman, *Physical Review* **56**, 340 (1939).
- 65 B. R. Trenhaile, A. Agrawal, and J. H. Weaver, *Applied Physics Letters* **89**, 151917 (2006).
- 66 R. M. Tromp, R. J. Hamers, and J. E. Demuth, *Physical Review B* **34**, 1388 (1986).
- 67 H. Tokumoto, K. Miki, and K. Kajimura, *Journal of Crystal Growth* **99**, 1329 (1990).
- 68 L. Vitali, M. G. Ramsey, and F. P. Netzer, *Physical Review Letters* **83**, 316 (1999).
- 69 B.-F. Ju, Y.-L. Chen, M. Fu, Y. Chen, and Y. Yang, *Sensors and Actuators A: Physical* **155**, 136 (2009).
- 70 Z. Q. Yu, C. M. Wang, Y. Du, S. Thevuthasan, and I. Lyubinetsky, *Ultramicroscopy* **108**, 873 (2008).
- 71 P. J. Cumpson, *Journal of Electron Spectroscopy and Related Phenomena* **73**,

- 25 (1995).
- 72 R. G. Cavell, S. P. Kowalczyk, L. Ley, R. A. Pollak, B. Mills, D. A. Shirley, and W.
Perry, *Physical Review B* **7**, 5313 (1973).
- 73 M. P. Seah, I. S. Gilmore, and S. J. Spencer, *Journal of Electron Spectroscopy
and Related Phenomena* **120**, 93 (2001).
- 74 M. P. Seah and M. T. Brown, *Applied Surface Science* **144-145**, 183 (1999).
- 75 J. Shirafuji and T. Sugino, *Diamond and Related Materials* **5**, 706 (1996).
- 76 G. Mills, H. Jónsson, and G. K. Schenter, *Surface Science* **324**, 305 (1995).
- 77 G. Henkelman, B. P. Uberuaga, and H. Jonsson, *The Journal of Chemical
Physics* **113**, 9901 (2000).
- 78 G. Henkelman and H. Jonsson, *The Journal of Chemical Physics* **113**, 9978
(2000).
- 79 S. Y. Liem, G. Kresse, and J. H. R. Clarke, *Surface Science* **415**, 194 (1998).
- 80 M. Villarba and H. Jónsson, *Surface Science* **317**, 15 (1994).
- 81 P. Ballone and et al., *EPL (Europhysics Letters)* **8**, 73 (1989).
- 82 M. E. Tuckerman, P. J. Ungar, T. von Roseninge, and M. L. Klein, *The Journal of
Physical Chemistry* **100**, 12878 (1996).
- 83 M. J. Field, P. A. Bash, and M. Karplus, *Journal of Computational Chemistry* **11**,
700 (1990).
- 84 F. Tassone, F. Mauri, and R. Car, *Physical Review B* **50**, 10561 (1994).
- 85 D. J. Evans and B. L. Holian, *The Journal of Chemical Physics* **83**, 4069 (1985).
- 86 S. Nose, *Journal of Physics: Condensed Matter* **2**, SA115 (1990).
- 87 W. G. Hoover, *Physical Review A* **37**, 252 (1988).
- 88 H. A. Posch, W. G. Hoover, and F. J. Vesely, *Physical Review A* **33**, 4253 (1986).
- 89 S. Toxvaerd and O. H. Olsen, *Physica Scripta* **1990**, 98 (1990).
- 90 H. Hasegawa and H. Ohno, *Journal of Vacuum Science & Technology B:
Microelectronics and Nanometer Structures* **4**, 1130 (1986).
- 91 J. Tersoff, *Physical Review B* **30**, 4874 (1984).
- 92 J. Bardeen, *Physical Review Letters* **45**, 1978 (1980).
- 93 N. Isshiki, H. Kageshima, K. Kobayashi, and M. Tsukada, *Ultramicroscopy* **42-44**,
109 (1992).
- 94 J. Tersoff and D. R. Hamann, *Physical Review Letters* **50**, 1998 (1983).
- 95 J. Tersoff and D. R. Hamann, *Physical Review B* **31**, 805 (1985).
- 96 K. Stokbro, B. Y.-K. Hu, C. Thirstrup, and X. C. Xie, *Physical Review B* **58**, 8038
(1998).
- 97 J. Tersoff, *Physical Review B* **40**, 11990 (1989).
- 98 R. F. W. Bader and H. Essen, *The Journal of Chemical Physics* **80**, 1943 (1984).

- 99 R. F. W. Bader, The Journal of Chemical Physics **73**, 2871 (1980).
100 Ald, eacute, M. n, H. L. Skriver, B. Johansson, ouml, and rje, Physical Review
Letters **71**, 2449 (1993).
101 W. Olovsson, I. A. Abrikosov, and B. Johansson, Journal of Electron
Spectroscopy and Related Phenomena **127**, 65 (2002).
102 T. P. Chen, Y. Liu, C. Q. Sun, M. S. Tse, J. H. Hsieh, Y. Q. Fu, Y. C. Liu, and S. Fung,
The Journal of Physical Chemistry B **108**, 16609 (2004).
103 E. Pehlke and M. Scheffler, Physical Review Letters **71**, 2338 (1993).
104 E. Lundgren, et al., Physical Review Letters **88**, 246103 (2002).
105 J. W. Evans, P. A. Thiel, and M. C. Bartelt, Surface Science Reports **61**, 1 (2006).



Curriculum vitae

LI, Hong-Dao

李宏道

inmyheart1314@hotmail.com



■ PERSONAL DETAILS

- Date of birth: Dec 14, 1976
- Civil state: married

■ SKILLS

- Thin film process
- Ultra-High-Vacuum (UHV) operation
- X-ray Photoelectron Spectroscopy (XPS) measurements
- Scanning Tunneling Microscope (STM) measurements
- First principle calculations
- Linux operation
- C, Matlab, and Fortran program design

■ EDUCATION

- Fu Jen Catholic University (FJU)
Undergraduate degree in department of physics, 2000-2004
- National Central University (NCU)
Master degree in institute of space physics, 2004-2006
- National Chiao Tung University (NCTU)
Ph. D. degree in institute of physics 2006- 2011

■ EXPERIENCE

- Operating Ultra-High-Vacuum system and XPS at National Synchrotron Radiation Research Center (NSRRC)
- Training semiconductor processing technology (VLSI) at National Nano Device laboratories (NDL)
- CMRFG member (Workshop on First-Principles Computational Material Physics)

■ PUBLICATIONS

1. C.-T. Lou, H.-D. Li, J.-Y. Chung, D.-S. Lin, T.C. Chiang
Oscillations of Bond Character and Polarization at the NaCl/Ge(100) Interface during Cyclic Growth.
Phys Rev. B 80, 195311 (2009)
2. Ming-Feng Hsieh, Hong-Dao Li, Deng-Sung Lin and Karina Morgenstern
Formation, binding, and stability of O-Ag-CO₂-Ag-O compounds on Ag(100) Investigated by Low Temperature Scanning Tunneling Microscopy and Manipulation.
J. Phys. Chem. C, 2010, 114 (33), pp 14173–14179 (2010)
3. Hong-Dao Li, Chan-Yuen Chang, Ling-Ying Chien, Shih-Hsin Chang, T.-C. Chiang and Deng-Sung Lin.
Adsorption and abstraction reactions of HCl on a single Si(100) dangling bond
Phys. Rev. B 83, 075403 (2011)
4. Jen-Yang Chung, Hong-Dao Li, Wan-Heng Chang, T. C. Leung, and Deng-Sung Lin.
Sodium chloride on Si (100) grown by molecular beam epitaxy.
Phys. Rev. B 83, 085305 (2011)
5. Ying-Hsiu Lin, Hong-Dao Li, Horng-Tay Jeng, and Deng-Sung Lin

Energetics and Interactions of Mixed Halogen Adsorbates on the Si(100) Surface.
J. Phys. Chem. C, DOI: 10.1021/jp201251j (2011)

6. Hong-Dao Li, Ying-Hsiu Lin, Horng-Tay Jeng, and Deng-Sung Lin
Two-dimensional Sodium chloride thin film on Si(100) grown by Atomic Layer
Deposition.
J. Phys. Chem. C (has been accepted for publication) (2011)

7. Hong-Dao Li, Ying-Hsiu Lin, Horng-Tay Jeng, and Deng-Sung Lin
Core Level Shifts of Halogen adsorbed Si(100) and Ge(100) surface.
J. Phys. Chem. C (reviewing) (2011)

